Stochastic Modeling of Magnetic Properties by Using Random Fields

Stochastische Modellierung von magnetischen Materialeigenschaften mit Zufallsfeldern
Zur Erlangung des akademischen Grades Doktor-Ingenieur (Dr.-Ing.)
genehmigte Dissertation von Radoslav Jankoski aus Gostivar
Tag der Einreichung: 26.06.2018, Tag der Prüfung: 28.11.2018
Darmstadt — D 17

1. Gutachten: Prof. Dr. Sebastian Schöps
2. Gutachten: Prof. Dr. Ulrich Römer

TECHNISCHE
UNIVERSITÄT
DARMSTADT

Fachbereich 18 - Electrical Engineering and Information Technology
GSCE/TEMF

Stochastic Modeling of Magnetic Properties by Using Random Fields
Stochastische Modellierung von magnetischen Materialeigenschaften mit Zufallsfeldern

Genehmigte Dissertation von Radoslav Jankoski aus Gostivar

1. Gutachten: Prof. Dr. Sebastian Schöps
2. Gutachten: Prof. Dr. Ulrich Römer

Tag der Einreichung: 26.06.2018
Tag der Prüfung: 28.11.2018

Darmstadt — D 17

Erklärung zur Dissertation

Hiermit versichere ich, die vorliegende Dissertation ohne Hilfe Dritter nur mit den angegebenen Quellen und Hilfsmitteln angefertigt zu haben. Alle Stellen, die aus Quellen entnommen wurden, sind als solche kenntlich gemacht. Diese Arbeit hat in gleicher oder ähnlicher Form noch keiner Prüfungsbehörde vorgelegen.

Darmstadt, den February 1, 2019

(R. Jankoski)

Contents

Abstract

This thesis is related to modeling uncertainties in magnetic properties of ferromagnetic materials which occur due to, e.g., manufacturing imperfections. The modeling procedure is based on the random field approach. The Karhunen-Loève expansion is used to approximate random fields with a minimal number of random variables in mean square sense. Two main cases are covered. First, magnetic hysteresis is taken into account and uncertainties are modeled by introducing the concept of multivariate random field. Second, spatial uncertainties of the magnetic behavior law are also treated. Benchmark examples such as a single phase transformer and a combined function magnet are used to illustrate how to propagate uncertainties from the input material data to the relevant output data.

Kurzfassung

Diese Dissertation behandelt Unsicherheiten in der Modellierung von magnetischen Eigenschaften ferromagnetischer Materialien, die beispielsweise durch den Fertigungsprozess auftreten. Die Modellierung basiert auf dem Konzept der Zufallsfelder. Die Karhunen-Loève Entwicklung ermöglicht die Approximation der Zufallsfelder mit einer minimalen Anzahl von zufälligen Variablen. Zwei Fälle werden behandelt. Zunächst wird magnetische Hysterese betrachtet, und Unsicherheiten werden durch multivariate Zufallsfelder modelliert. Anschliessend werden räumliche Unsicherheiten des magnetischen Materialgesetzes behandelt. Anhand von Anwendungen, beispielsweise einem Einphasen-Transformator und einem Multifunktions-Magneten, wird gezeigt, wie Unsicherheiten von den Material-Eingangsdaten in die relevanten Ausgangsdaten propagiert werden können.

1 Introduction

1.1 Motivation

The design of electrical devices can be significantly improved if a numerical simulation is carried out in the early design phase. Often the time to manufacture the device can also be reduced. Developing computational models enables us to predict the behavior of those devices under different circumstances and investigate multiple scenarios [1]. The modern computational paradigm consists of choosing an appropriate mathematical model, usually expressed through partial differential equations (PDEs), that captures the physical phenomena and solve a numerical approximation on a computer.

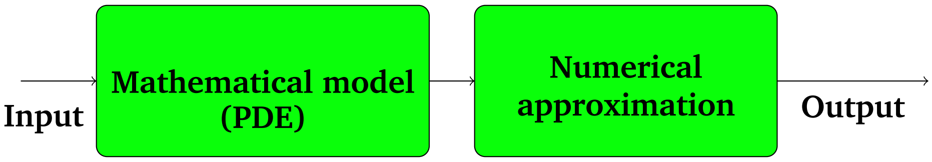

Figure 1: Abstraction of a deterministic simulation

In order to analyze certain aspects of a given system one has to identify the input parameters, e.g., geometry and material properties, and the output parameters, e.g., power losses and consumption, as it is depicted in Fig. 1. The main assumption of the approach shown in Fig. 1 is that the input parameters are well known. However, in engineering practice this is rarely true. Usually the input data is subject to uncertainty. In a modeling context these uncertainties appear in the boundary and initial conditions, source terms in the right hand side of the PDE and material properties. One deterministic simulation, as the one illustrated in Fig. 1, is not enough to make a statement about the real-world behavior of the system. The uncertainties have to be considered as well. In particular it is important to quantify their impact on the output parameters, commonly referred to as quantities of interest (QoIs), which are relevant in the design phase.

One usually distinguishes between aleatoric and epistemic type of uncertainty. The first type of uncertainty arises due to the intrinsic randomness of the input parameter. When there is a mass production of a certain material, e.g., ferromagnetic materials, their properties vary in each sample due to the manufacturing imperfection. The second type arises due to lack of data and knowledge about the system. Unlike aleatoric the epistemic uncertainty can be reduced by obtaining additional information about the system. Aleatoric uncertainty is characterized by assigning a probability density function (PDF) to the uncertain input. The epistemic uncertainty is modeled by intervals which represent degree of belief of the analyst with or without assigning a corresponding PDF [2].

The simplest and oldest known method to propagate the uncertainties from input parameters is the Monte Carlo (MC) method. This method consists of generating random realizations of the input data and collecting it in order to compute the statistics of the output parameters. The MC method suffers from a low convergence rate, i.e., a relatively large number of deterministic simulations are required such that the computed statistics of the QoI converges. In contrast to the MC method spectral methods, for instance generalized polynomial chaos expansion, stochastic collocation, stochastic Galerkin method are a suitable replacements to circumvent the low convergence rate problem, see [3, 4]. On the other hand, these methods become quickly computationally expensive as the number of random variables grows. This problem is known as "curse of dimensionality". To remedy this issue many techniques have been suggested in the literature such as sparse grids [5, 6], tensor decomposition [7, 8, 9, 10]. However, the problem could be remedied if the input parameters are modeled with a small number of random variables.

In this thesis the focus will be placed on uncertainties in material properties which are usually described via space- and state-dependent material functions in which uncertainties may be introduced by random fields. The key benefit of this approach is that they can be approximated, i.e., represented by the smallest number of random variables in mean square sense, by using the orthogonal decomposition known as the Karhunen-Loève (KLE) expansion [11].

In discreet settings, a reduction of the number of random variables can be achieved by using a principal component analysis [12]

This thesis deals with modeling uncertainties of magnetic properties in ferromagnetic materials. These materials are building blocks of many electrical devices, for instance electric motors, power transformers and accelerator magnets. Understanding their internal properties plays a key role in the design. During the manufacturing process magnetic materials go through mechanical and laser cutting, punching and rolling. These procedures influence the magnetic law. Experimental results that describe the impact of the manufacturing processes, quantitatively and qualitatively, have been reported in the literature, see [13, 14, 15, 16, 17, 18].

Three papers represent the starting point for the work presented in this thesis. First in [19] twenty eight samples of magnetic behavior law expressed via $B-H$ curves coming from a production chain were reported. These experimental results were only related to the initial magnetization curves. Later, full hysteresis cycles from the same production chain were also reported in [20]. In both papers stochastic models are proposed based on four in [19] and six in [20] random variables, respectively. These random variables represent physical quantities related to the magnetization process.

The third paper [21] is the pioneering work that relates the concept of random fields and the KLE with the magnetic properties. Namely, it was recognized that the perturbed $B-H$ curves presented in [19] can be modeled as a univariate random field. A strong correlation was observed in the perturbed $B-H$ curves that has enabled a truncation of the KLE after a few terms.

There are two research goals in this thesis:

- First, we want to take into account uncertainty in magnetic hysteresis by using the random field approach in order to exploit the key benefit of reducing the number of random variables.
- Second, we want to handle spatial uncertainties of the magnetic behavior law by using the same approach.

The work presented has two main contributions:

- First, a new stochastic model is developed that takes into account the hysteretic properties of ferromagnetic materials and is still based on the KLE. This possibility is recognized in a phenomenological type of hysteresis model known as the Duhem model [22] combined with a multivariate random field approach [23].
- Second, a generalization is achieved by allowing spatial variation of the magnetic law, i.e., the case when it depends on spatial coordinates is considered. The contribution here

is related to circumventing a drawback that arises when the KLE is applied to a spatial random field. Namely, a generalized eigenvalue problem arises with relatively large dense matrices which require huge computer memory and slow down iterative algorithms for solving eigenvalue problems. In order to deal with the dense matrix format we use the hierarchical matrix technique [24]. The hierarchical matrix format reduces the memory requirements and decreases the complexity of basic arithmetical operations such as matrix addition, matrix-vector and matrix-matrix multiplications.

The practical relevance of our contribution will be illustrated via two types of benchmark examples. We will consider transformers and accelerators magnets. In particular, the magnetic hysteresis model is important for modeling remanence effects in accelerator magnets.

1.2 Thesis overview

The work of this thesis is organized as follows: In Chapter 2 Maxwell's equations are given and the derivation of the so called magnetoquastistatic approximation. The numerical approximation of the magnetoquasistatic model is derived in Chapter 3 by means of the finite element method (FEM) and the implicit Euler method. The concept of random field is introduced in Chapter 4 and its extension to the multivariate case. Also the stochastic collocation method for uncertainty propagation is explained.

The main contribution of this thesis is in Chapter 5 and Chapter 6. In Chapter 5 the material functions of the Duhem model for ferromagnetic hysteresis are modeled as cross-correlated trivariate random field. The hierarchical matrix technique and the Lanczos algorithm for solving an eigenvalue problem are explained in Chapter 6.

Chapter 7 is related to the simulation of remanence effects in a combined function magnet. Summary and outlook are given in Chapter 8.

2 Governing Equations

The electrical devices studied in this thesis are subject to the electromagnetic phenomenon. Therefore, we will consider Maxwell's equations. The content presented in this section can be found in many textbooks, e.g., see [25]. We will derive the so called magnetoquasistatic approximation of Maxwell's equations. As we will focus on magnetic materials, a precise definition of the magnetic reluctivity will be given.

2.1 Maxwell's equations

On the macroscopic level the laws of electromagnetism are fully described by the four Maxwell's equations. The usual differential form is given as

$$\nabla \cdot \boldsymbol{D} = \rho, \tag{1}$$
$$\nabla \cdot \boldsymbol{B} = 0, \tag{2}$$
$$\nabla \times \boldsymbol{E} = -\frac{\partial \boldsymbol{B}}{\partial t}, \tag{3}$$
$$\nabla \times \boldsymbol{H} = \boldsymbol{J} + \frac{\partial \boldsymbol{D}}{\partial t}, \tag{4}$$

where $\boldsymbol{E}$ is the electric field, $\boldsymbol{D}$ is the electric displacement, $\boldsymbol{H}$ is the magnetic field strength, $\boldsymbol{B}$ is the magnetic flux density, $\boldsymbol{J}$ is the electric current density and ρ is the electric charge density. The introduced quantities are functions on space and time. Maxwell's equations are supplemented by boundary conditions or decay conditions for bounded or unbounded domains, respectively. In addition to the Maxwell's equations, the electromagnetic properties of the media are expressed through the constitutive relations

$$\boldsymbol{D} = \varepsilon \boldsymbol{E}, \tag{5}$$

$$\boldsymbol{J} = \sigma \boldsymbol{E}, \tag{6}$$

where ε is the electric permittivity, σ is the electric conductivity. Special attention will be placed on the relationship between $\boldsymbol{H}$ and $\boldsymbol{B}$ expressed as

$$\boldsymbol{B} = \overline{\mu} \boldsymbol{H}, \tag{7}$$

where $\overline{\mu}$ is the magnetic permeability tensor. The constitutive relations (5) and (6) could be expressed also via tensors. However, in this thesis we shall consider the simple case when they are scalar quantities. The constitutive relation (7) can be written as

$$\boldsymbol{H} = \overline{\nu} \boldsymbol{B}, \tag{8}$$

where $\overline{\nu} = \overline{\mu}^{-1}$ is the magnetic reluctivity tensor given as follows

$$\overline{\nu} := \begin{bmatrix} \nu_{\mathrm{xx}} & \nu_{\mathrm{xy}} & \nu_{\mathrm{xz}} \\ \nu_{\mathrm{yx}} & \nu_{\mathrm{yy}} & \nu_{\mathrm{yz}} \\ \nu_{\mathrm{zx}} & \nu_{\mathrm{zy}} & \nu_{\mathrm{zz}} \end{bmatrix}. \tag{9}$$

Moreover, we are going to consider the simplest anisotropic model that neglects all elements which are not on the main diagonal and also decouples the laws in each direction, i.e., the H_x, H_y and H_z depend only on B_x, B_y and B_z, respectively. In this case the magnetic reluctivity tensor is given as

$$\overline{\nu} := \begin{bmatrix} \nu_\mathrm{xx}(B_\mathrm{x}) & 0 & 0 \\ 0 & \nu_\mathrm{yy}(B_\mathrm{y}) & 0 \\ 0 & 0 & \nu_\mathrm{zz}(B_\mathrm{z}) \end{bmatrix}. \tag{10}$$

This modeling approach has been discussed for instance in [26].

2.1.1 Magnetoquasistatic approximation

By adding the displacement current $\frac{\partial \boldsymbol{D}}{\partial t}$ into the previously established Ampère's law (4), Maxwell predicted the existence of electromagnetic waves. The wavelength of the electromagnetic waves depends on the angular frequency $\omega = 2\pi f$, where f is the frequency, of the radiation source and the electromagnetic properties of the medium in which they are propagating. These relation reads as follows,

$$\lambda = \frac{2\pi}{\omega\sqrt{\varepsilon\mu}}, \tag{11}$$

where μ is linear isotropic magnetic permeability. The Maxwell's equations in frequency domain are given as

$$\nabla \cdot \boldsymbol{D} = \rho, \tag{12}$$

$$\nabla \cdot \boldsymbol{B} = 0, \tag{13}$$

$$\nabla \times \boldsymbol{E} = -j\omega\mu\boldsymbol{H}, \tag{14}$$

$$\nabla \times \boldsymbol{H} = \boldsymbol{J} + j\omega\boldsymbol{D}, \tag{15}$$

where $j = \sqrt{-1}$. In some real world applications, such as transformers, electric motors and accelerator magnets, the use of the full set of Maxwell's equations is unnecessary. A great deal of simplification can be made by neglecting the displacement current. This approximation is known as magnetoquaststistatics. A justification of the magnetoquasistatic model has been given by both, engineers and mathematicians [27, 28]. The intuitively accepted conditions are if the wavelength exceeds significantly the diameter of the computational domain D, i.e.,

$$\mathrm{diam}(D) \ll \lambda, \tag{16}$$

and if

$$\omega\varepsilon \ll \sigma, \tag{17}$$

then the displacement current can be neglected. Let us for the sake of clarity denote the electric field coming from the full set of Maxwell's equation as $\boldsymbol{E}^\mathrm{m}$ and only $\boldsymbol{E}$ the one from the magnetoquasistatic approximation. The rigorous mathematical analysis in [28] shows that the error due to the approximation is estimated as

$$\frac{||\boldsymbol{E}^{\mathrm{m}} - \boldsymbol{E}||_{L^2(D)}}{||\boldsymbol{E}^{\mathrm{m}}||_{L^2(D)}} \leq C_1 \varepsilon \mu \omega^2 \mathrm{diam}(D)^2 + C_2 \frac{\omega \varepsilon}{\sigma}, \tag{18}$$

where C_1 and C_2 are constants which are influenced by the geometry of the system. The error in (18) indeed becomes small if

$$C_1 \varepsilon \mu \omega^2 \mathrm{diam}(D)^2 \ll 1, \tag{19}$$

$$C_2 \frac{\omega \varepsilon}{\sigma} \ll 1, \tag{20}$$

which are recognized as the condition given by (16) and (17) if the constants C_1 and C_2 have moderate sizes. One should keep in mind that these conditions can lose their meaning if C_1 and C_2 have large values. In this context, certain scenarios related to the topology can contribute as explained in [28]. The discussion in this section is restricted to isotropic and linear magnetic properties. In our work we consider more a complicated nonlinear anisotropic magnetic behavior law. Nevertheless, within the scope of thesis we are going to neglect the displacement current.

2.1.2 Magnetic vector potential

From (2) it follows that the magnetic flux density is a divergence free quantity. This allows that we express it as

$$\boldsymbol{B} = \nabla \times \boldsymbol{A}, \tag{21}$$

where $\boldsymbol{A}$ is the magnetic vector potential.

2.1.3 Current density and governing partial differential equation

As we already stated, the displacement current will be neglected so we are left with two types of currents which are summarized on the right hand side of (4). The current density vector is given as

$$\boldsymbol{J} = \boldsymbol{J}_{\mathrm{o}} + \boldsymbol{J}_{\mathrm{c}}, \tag{22}$$

where $\boldsymbol{J}_{\mathrm{o}}$ is the current density imposed by a source and $\boldsymbol{J}_{\mathrm{c}}$ is the induced electric current. From (3) it follows

$$\boldsymbol{E} = -\frac{\partial \boldsymbol{A}}{\partial t} - \nabla \phi, \tag{23}$$

where ϕ is an electric scalar potential. The induced current density vector

$$\boldsymbol{J}_{\mathrm{c}} = -\sigma(\frac{\partial \boldsymbol{A}}{\partial t} + \nabla \phi). \tag{24}$$

By substituting (24) into (22) and (21) in (4) and neglecting the displacement current, the following partial differential equation is obtained

$$\sigma \frac{\partial \boldsymbol{A}}{\partial t} + \nabla \times (\overline{\nu} \nabla \times \boldsymbol{A}) = \boldsymbol{J}_{\mathrm{o}} - \sigma \nabla \phi. \tag{25}$$

We are going to use $\boldsymbol{A}^*$ formulation, i.e., $\phi = 0$, see [29]. The governing PDE (25) can be written as

$$\sigma \frac{\partial \boldsymbol{A}}{\partial t} + \nabla \times (\overline{\nu} \nabla \times \boldsymbol{A}) = \boldsymbol{J}_{\mathrm{o}}, \tag{26}$$

and the boundary conditions are still to be defined. In order to achive uniqueness of $\boldsymbol{A}$, a gauge conditions needs to be defined. However, in the scope of this thesis we are going to work with simplified 2D version of (26) where gauging is not necessary.

2.2 Reduction from 3D to 2D

Often a preliminary study of a low frequency electromagnetic system can be conducted by considering only a 2D cross section. The magnetic field is considered to have components only on the x − y plane and the source current density has only z—component. The dependency on z—coordinate is assumed to vanish. The vector quantities subject to 2D simplification are given as,

$$\begin{aligned} \boldsymbol{H} &= H_{\mathrm{x}} \boldsymbol{e}_{\mathrm{x}} + H_{\mathrm{y}} \boldsymbol{e}_{\mathrm{y}}, \\ \boldsymbol{B} &= B_{\mathrm{x}} \boldsymbol{e}_{\mathrm{x}} + B_{\mathrm{y}} \boldsymbol{e}_{\mathrm{y}}, \\ \boldsymbol{A} &= A_{\mathrm{z}} \boldsymbol{e}_{\mathrm{z}}, \\ \boldsymbol{J}_{\mathrm{o}} &= J_{\mathrm{z}} \boldsymbol{e}_{\mathrm{z}}, \end{aligned} \tag{27}$$

where $\boldsymbol{e}_{\mathrm{x}}, \boldsymbol{e}_{\mathrm{y}}$ and $\boldsymbol{e}_{\mathrm{z}}$ are unit vectors in a Cartesian coordinate system. If (27) is substituted into (26) the reduced 2D governing equation is obtained

$$-\frac{\partial}{\partial x}\left(\nu_{\mathrm{yy}} \frac{\partial A_{\mathrm{z}}}{\partial x}\right) - \frac{\partial}{\partial y}\left(\nu_{\mathrm{xx}} \frac{\partial A_{\mathrm{z}}}{\partial y}\right) + \sigma \frac{\partial A_{\mathrm{z}}}{\partial t} = J_{\mathrm{z}}, \tag{28}$$

or written in a simplified manner

$$\sigma \frac{\partial A_{\mathrm{z}}}{\partial t} - \nabla \cdot (\overline{\nu}_{\mathrm{d}} \nabla A_{\mathrm{z}}) = J_{\mathrm{z}}, \tag{29}$$

where

$$\overline{\nu}_{\mathrm{d}} := \begin{bmatrix} \nu_{\mathrm{yy}} & 0 \\ 0 & \nu_{\mathrm{xx}} \end{bmatrix}. \tag{30}$$

For the derivation of the weak formulation in the next chapter we will use (29).

2.3 Formulation of the problem

We consider a magnetoquasistatic problem on the computational domain D with the boundary ∂D, in the time interval $T = [0, T_{\mathrm{c}}]$ as it is depicted in Fig. 2. The coil domains in which the imposed electric current flows in positive and negative direction w.r.t. the z-axis are denoted as $D_{\mathrm{j}}^{(+)}$ and $D_{\mathrm{j}}^{(-)}$, respectively. Their union is written as $D_{\mathrm{j}} = D_{\mathrm{j}}^{(+)} \cup D_{\mathrm{j}}^{(-)}$. The total computational domain is given as $\overline{D} = \overline{D}_{\mathrm{j}} \cup \overline{D}_{\mathrm{e}} \cup \overline{D}_{\mathrm{c}}$. The conductivity is assumed to satisfy

$$\sigma := \begin{cases} \sigma_{\mathrm{c}} & \text{in } D_{\mathrm{c}}, \\ 0 & \text{in } D_{\mathrm{e}} \cup D_{\mathrm{j}}, \end{cases} \tag{31}$$

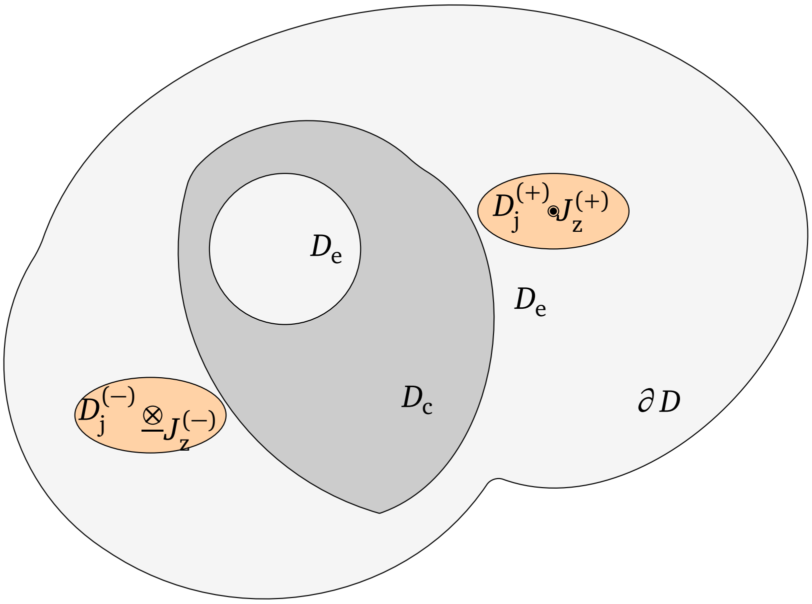

Figure 2: Geometry under consideration

where $\sigma_c > 0$ is a positive constant. The magnetic reluctivity is given as

$$\overline{\nu}_\mathrm{d} := \begin{cases} \overline{\nu}_\mathrm{c} & \text{in } D_\mathrm{c}, \\ \overline{\nu}_0 & \text{in } D_\mathrm{e} \cup D_\mathrm{j}, \end{cases} \tag{32}$$

where

$$\overline{\nu}_0 := \begin{bmatrix} \nu_0 & 0 \\ 0 & \nu_0 \end{bmatrix} \quad \overline{\nu}_\mathrm{c} := \begin{bmatrix} \nu_{yy}^\mathrm{c} & 0 \\ 0 & \nu_{xx}^\mathrm{c} \end{bmatrix}. \tag{33}$$

The reluctivity of the vacuum is denoted as ν_0. We will omit denoting the magnetic reluctivity with superscript c to emphasize that it belongs to the core region.
The current density is defined as

$$J_\mathrm{z} := \begin{cases} -J_\mathrm{z}^{(-)} & \text{in } D_j^{(-)}, \\ J_\mathrm{z}^{(+)} & \text{in } D_j^{(+)}. \end{cases} \tag{34}$$

In computational practice boundary of the domain ∂D is chosen to be far away from $D_\mathrm{j} \cup D_\mathrm{c}$ such that the magnitude of the magnetic flux density decreases significantly. This is a reasonable assumption because the field decreases in strength as we analyse points further away from the source. The magnetic flux density that penetrates through ∂D is neglected which leads to the boundary condition $\boldsymbol{n_0} \cdot \boldsymbol{B} = 0$. One way to impose this condition is to set the tangential component of $\boldsymbol{A}$ to zero, i.e., $\boldsymbol{A} \times \boldsymbol{n_0} = 0$ on ∂D which implies that the normal component of the magnetic flux density is zero. Thus, no magnetic flux penetrates the boundary ∂D. In the 2D case this condition is simply written as $A_\mathrm{z} = 0$. We seek for solution A_z which is subject to:

$$\begin{aligned} \sigma \frac{\partial A_\mathrm{z}}{\partial t} - \nabla \cdot (\overline{\nu}_\mathrm{d} \nabla A_\mathrm{z}) = J_\mathrm{z} \quad & \text{in} \quad D \times T, \\ A_\mathrm{z} = 0 \quad & \text{in} \quad \partial D \times T, \\ A_\mathrm{z}(0) = 0 \quad & \text{for} \quad D \times \{0\}, \end{aligned} \tag{35}$$

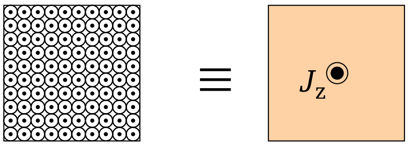

Figure 3: Stranded conductor model

where $A_z(t) := A_z(\boldsymbol{x}, t)$. We will omit spatial or temporal notation when possible.

2.4 Conductor modeling

In many technical applications a large number of conductors are part of the coil region. Resolving each wire within the FEM mesh is computationally expensive. Instead a modeling assumption is introduced. Namely it is assumed that the current density is constant across the coil domain, see Fig. 3, and it is computed as

$$J_z = \begin{cases} \frac{-N_j I_j}{S_j} & \text{in } D_j^{(-)} \\ \frac{N_j I_j}{S_j} & \text{in } D_j^{(+)} \end{cases} \tag{36}$$

where N_j is the number of wires, I_j is the electric current flowing in a single wire and S_j is the cross-sectional area of the coil domain D_j. This conductor model is known as “stranded conductor model” and it has been introduced in [30].

2.5 Magnetic reluctivity tensor

The magnetic reluctivity explained here is related only to the ferromagnetic domain D_c of the considered system. We will omit using upper and lower scripts to denote this consideration. The relationship between $\boldsymbol{H}$ and $\boldsymbol{B}$ is expressed via the magnetic reluctivities ν_{xx} and ν_{yy} as follows

$$H_x = \nu_{xx} B_x, \tag{37a}$$
$$H_y = \nu_{yy} B_y. \tag{37b}$$

We are going to consider three cases:

a) Linear magnetic reluctivity

b) Nonlinear magnetic reluctivity

c) Nonlinear magnetic reluctivity with hysteresis taken into account

The third case will be explained in seventh chapter after we introduce the magnetic hysteresis. The definitions that follow will refer to both ν_{xx} and ν_{yy}. We will refer to the x and y component as p, where $p \in \{x, y\}$, in order to avoid writing the same definitions twice. The magnetic reluctivity is defined as

$$\nu_{pp}(B_p) := \frac{H_p}{B_p}, \tag{38}$$

for $B_p \neq 0$. We proceed by introducing the the first two cases.

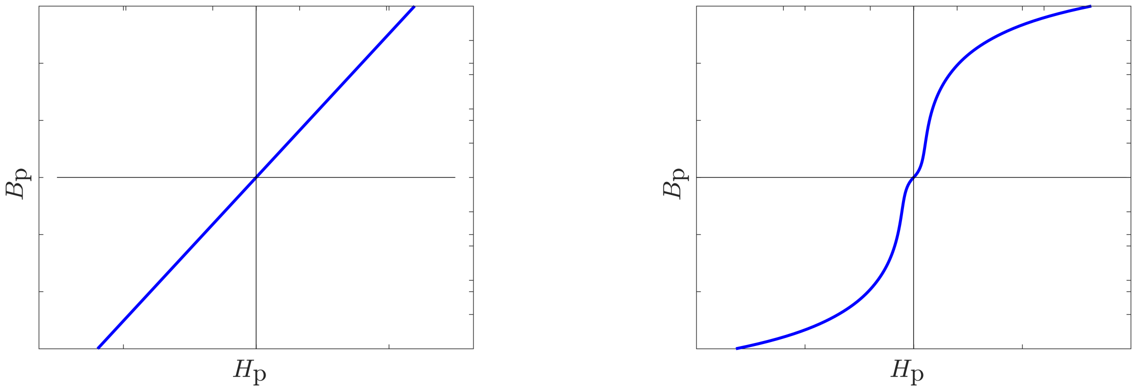

(a) Linear $B-H$ curve **(b)** Nonlinear $B-H$ curve

Figure 4: Linear (a) and nonlinear (b) $B-H$ curve

2.5.1 Linear magnetic reluctivity

The analysis of electrical devices is significantly simplified in the case where the magnetic reluctivity is considered to be linear. In this case $\nu_\mathrm{xx} = C_1$, and also $\nu_\mathrm{yy} = C_2$, where C_1 and C_2 are constants, see Fig. 4a. The error which arises due to linearizing nonlinear models has been studied in details in [31]. However, we are going to use the linear magnetic reluctivity without specifying from which nonlinear curve has been extracted as an approximation, i.e., we will not consider any error analysis.

2.5.2 Nonlinear magnetic reluctivity

For nonlinear magnetic materials the relationship between H_p and B_p is expressed through the so called $B-H$ curve, as it is depicted in Fig. 4b. The properties that the curve satisfies are discussed in [32]. We are going to work with the inverse of the $B-H$ curve because it is more convenient for the magnetic vector potential formulation. In [32] the listed properties refer to the amplitudes, i.e., the absolute values of $\boldsymbol{H}$ and $\boldsymbol{B}$. Here we deal with the individual components of the vectors where negative values are possible. Thus, we will consider the negative real numbers as part of the domain and codomain of the $B-H$ mapping. The curve is denoted as $F^\mathrm{p}_\mathrm{HB} : \mathbb{R} \to \mathbb{R}$ and it satisfies the following properties

$$F^\mathrm{p}_\mathrm{HB}(0) = 0, \tag{39a}$$

$$\frac{\partial F^\mathrm{p}_\mathrm{HB}(B_\mathrm{p})}{\partial B_\mathrm{p}} \le \nu_0, \quad \forall B_\mathrm{p} \in \mathbb{R} \tag{39b}$$

$$\lim_{B_\mathrm{p}\to\pm\infty} \frac{\partial F^\mathrm{p}_\mathrm{HB}(B_\mathrm{p})}{\partial B_\mathrm{p}} = \nu_0. \tag{39c}$$

The magnetic reluctivity (38) can be written as

$$\nu_\mathrm{pp}(B_\mathrm{p}) := \frac{F^\mathrm{p}_\mathrm{HB}(B_\mathrm{p})}{B_\mathrm{p}}, \quad \text{if} \quad B_\mathrm{p} \neq 0. \tag{40}$$

From (40) we can write $F_{\mathrm{HB}}^{\mathrm{p}}(\cdot) = \nu_{\mathrm{pp}}(\cdot)\cdot$. The magnetic reluctivity satisfies the following properties

$$
\begin{aligned}
&0 < \nu_{\min}^{\mathrm{p}} \leq \nu_{\mathrm{pp}}(B_{\mathrm{p}}) \leq \nu_0, && \text{(41a)}\\
&\nu_{\mathrm{pp}}(\cdot)\cdot \ \text{ is Lipschitz continuous with constant } \nu_0, && \text{(41b)}\\
&\nu_{\mathrm{pp}}(\cdot)\cdot \ \text{ is monotonically increasing for } B \in \mathbb{R}. && \text{(41c)}
\end{aligned}
$$

At the point $B_{\mathrm{p}} = 0$ the magnetic reluctivity $\nu_{\mathrm{pp}}(0)$ is defined by taking the limit $B_{\mathrm{p}} \to 0$. More precisely the limit can be defined from both the left and the right side. We assume that the limit approaches to the same value from both sides as

$$
\nu_{\mathrm{pp}}(0) := \lim_{B_{\mathrm{p}} \to 0^{\pm}} \frac{F_{\mathrm{HB}}^{\mathrm{p}}(B_{\mathrm{p}})}{B_{\mathrm{p}}} = \nu_{\min}^{\mathrm{p}}, \tag{42}
$$

2.6 Conclusion

This section was concerned with the governing equations in a deterministic setting. Maxwell's equations were presented and the magnetoquaststatic approximation derived by using the magnetic vector potential. The assumptions of the 3D to 2D reduction were explained under which the governing equations were stated. The magnetic reluctivity was defined in three particular scenarios which will be considered in this thesis.

3 Numerical Approximation of the Governing Equations

The aim of this chapter is to introduce the numerical approximation of the governing equations presented in chapter 2. We introduce the FEM and implicit Euler method as discretization techniques in space and time, respectively. The Newton-Raphson method will be introduced to address the nonlinear problem that arises due to the magnetic reluctivity tensor.

3.1 Weak formulation

Before we proceed with the derivation of the weak formulation we need to introduce some elements of function spaces. We refer to [33, 34, 35, 36, 37] for all details related to functional analysis. We consider the space of all real valued square integrable functions $L_2(D)$, i.e., $u \in L_2(D)$ where it holds

$$\int_D |u(\boldsymbol{x})|^2 \mathrm{d}\boldsymbol{x} < \infty. \tag{43}$$

Next, we introduce the Hilbert space $H_0^1(D)$ defined as

$$H_0^1(D) = \{u \in L_2(D); \quad \frac{\partial u}{\partial x}, \frac{\partial u}{\partial y} \in L_2(D); \ u = 0 \ \text{ on } \ \partial D\}. \tag{44}$$

The governing equation is multiplied with a test function v and integrated over the computational domain D as follows

$$\int_D \sigma \frac{\partial A_\mathrm{z}}{\partial t} v \mathrm{d}\boldsymbol{x} - \int_D v \nabla \cdot (\overline{\nu}_\mathrm{d} \nabla A_\mathrm{z}) \mathrm{d}\boldsymbol{x} = \int_D J_\mathrm{z} v \mathrm{d}\boldsymbol{x}. \tag{45}$$

The following relation is exploited:

$$v \nabla \cdot (\overline{\nu}_\mathrm{d} \nabla A_\mathrm{z}) = \nabla \cdot (v \overline{\nu}_\mathrm{d} \nabla A_\mathrm{z}) - \overline{\nu}_\mathrm{d} \nabla A_\mathrm{z} \cdot \nabla v. \tag{46}$$

By substituting (46) into (45) we obtain

$$\int_D \sigma \frac{\partial A_\mathrm{z}}{\partial t} v \mathrm{d}\boldsymbol{x} + \int_D \overline{\nu}_\mathrm{d} \nabla A_\mathrm{z} \cdot \nabla v \mathrm{d}\boldsymbol{x} - \oint_{\partial D} v (\overline{\nu}_\mathrm{d} \nabla A_\mathrm{z}) \cdot \boldsymbol{n_0} \mathrm{d}S = \int_D J_\mathrm{z} v \mathrm{d}\boldsymbol{x}, \tag{47}$$

where $\boldsymbol{n_0}$ is the outer normal vector to ∂D. In order (47) to be well defined and the boundary term to vanish, we chose $v \in H_0^1$. We seek a solution $A_\mathrm{z} \in H_0^1(D)$ such that

$$\int_D \sigma \frac{\partial A_\mathrm{z}}{\partial t} v \mathrm{d}\boldsymbol{x} + \int_D \overline{\nu}_\mathrm{d} \nabla A_\mathrm{z} \cdot \nabla v \mathrm{d}\boldsymbol{x} = \int_D J_\mathrm{z} v \mathrm{d}\boldsymbol{x} \quad \forall v \in H_0^1(D). \tag{48}$$

In this case we say that A_z is the weak solution of (35) and (48) is known as the weak formulation.

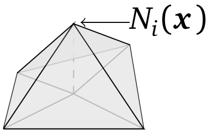

Figure 5: hat function

3.2 Finite element approximation

The first step towards the finite element approximation is to restrict the original space in which we seek a solution to a finite dimensional subspace $V^h \subset H_0^1(D)$. The space V^h is defined as

$$V^h = \text{span}\{N_1, ..., N_n\} \tag{49}$$

where N_i is a piecewise polynomial basis functions with a fixed degree. In this thesis we consider linear basis functions, also known as hat function, see Fig. 5. The approximation of the z component of the magnetic vector potential is given as

$$A_\text{z}^h(\boldsymbol{x}, t) = \sum_{i=1}^{n} a_{\text{z}i}(t) N_i(\boldsymbol{x}). \tag{50}$$

We seek for a solution $A_\text{z}^h \in V^h$ such that

$$\int_D \sigma \frac{\partial A_\text{z}^h}{\partial t} v \mathrm{d}\boldsymbol{x} + \int_D \overline{\nu}_\text{d} \nabla A_\text{z}^h \cdot \nabla v \mathrm{d}\boldsymbol{x} = \int_D J_\text{z} v \mathrm{d}\boldsymbol{x} \quad \forall v \in V^h. \tag{51}$$

For the sake of clarity, in the derivations that follow, we will introduce the local linear system of equations. The global system of equations is obtained via an assembly process. We choose to discretize the computational domain by a finite number of triangular elements. Let us consider only one triangular element as it is depicted in Fig. 6.

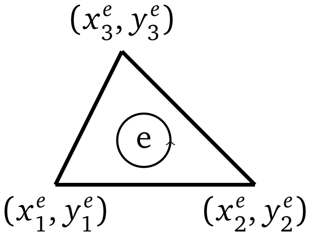

Figure 6: 2D triangular finite element

The unknown A_z is represented as a sum of linear shape functions within the e-th triangular element as follow:

$$A_\text{z}^e(\boldsymbol{x}, t) = \sum_{i=1}^{3} a_{zi}^e(t) N_i^e(\boldsymbol{x}), \tag{52}$$

where N_i^e is a linear shape function having value one on the i—th node and zero on the others as it is shown in Fig. 7.

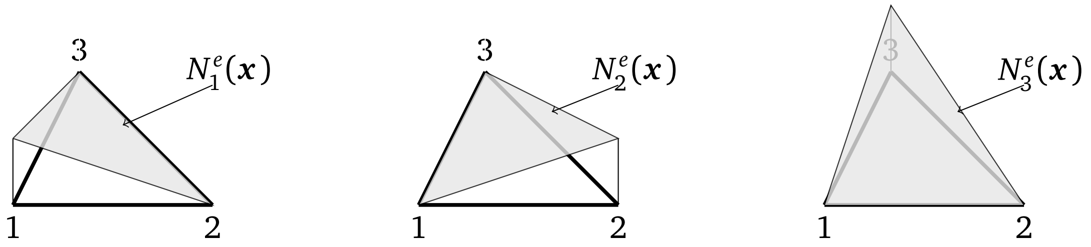

Figure 7: Linear shape functions of the e-th element

The expressions for the three linear shape functions active on the e-th element, see [38, Page 102] are given as

$$
\begin{aligned}
N_1^e(\boldsymbol{x}) &= \frac{1}{2A^e}\left(a_1^e + b_1^e x + c_1^e y\right),\\
N_2^e(\boldsymbol{x}) &= \frac{1}{2A^e}\left(a_2^e + b_2^e x + c_2^e y\right),\\
N_3^e(\boldsymbol{x}) &= \frac{1}{2A^e}\left(a_3^e + b_3^e x + c_3^e y\right),
\end{aligned}
\tag{53}
$$

where A^e denotes the area of the triangle. The coefficients $a_1^e, a_2^e, a_3^e, b_1^e, b_2^e, b_3^e, c_1^e, c_2^e, c_3^e$ are computed as

$$
\begin{array}{lll}
a_1^e = x_2^e y_3^e - x_3^e y_2^e & b_1^e = y_2^e - y_3^e & c_1^e = x_3^e - x_2^e\\
a_2^e = x_3^e y_1^e - x_1^e y_3^e & b_2^e = y_3^e - y_1^e & c_2^e = x_1^e - x_3^e\\
a_3^e = x_1^e y_2^e - x_2^e y_1^e & b_2^e = y_1^e - y_2^e & c_3^e = x_2^e - x_1^e,
\end{array}
\tag{54}
$$

By using the Galerkin approach, i.e., by choosing the test function from $\{N_i^e\}_{i=1}^3$ the following system of equations is obtained

$$
\sum_{i=1}^{3} a_{zi}^e(t) \int_{D^e} \overline{\nu}_{\mathrm{d}}^e \nabla N_i^e \cdot \nabla N_j^e \mathrm{d}\boldsymbol{x} + \sum_{i=1}^{3} \frac{\mathrm{d}a_{zi}^e(t)}{\mathrm{d}t} \int_{D^e} \sigma N_i^e N_j^e \mathrm{d}\boldsymbol{x} = \int_{D^e} J_z N_j^e \mathrm{d}\boldsymbol{x},
\tag{55}
$$

which results in the following local system of equations

$$
\boldsymbol{K}^e \boldsymbol{a}^e(t) + \boldsymbol{M}^e \frac{\mathrm{d}\boldsymbol{a}^e(t)}{\mathrm{d}t} = \boldsymbol{F}^e,
\tag{56}
$$

where $\boldsymbol{K}^e \in \mathbb{R}^{3\times3}$ is the local stiffness matrix whose elements are computed as

$$
K_{ij}^e = \int_{D^e} \overline{\nu}_{\mathrm{d}}^e \nabla N_i^e \cdot \nabla N_j^e \mathrm{d}\boldsymbol{x}.
\tag{57}
$$

The elements of the mass matrix $\boldsymbol{M}^e \in \mathbb{R}^{3\times3}$ are given as

$$
M_{ij}^e = \int_{D^e} \sigma N_i^e N_j^e \mathrm{d}\boldsymbol{x},
\tag{58}
$$

and the loading vector elements as

$$
F_i^e = \int_{D^e} J_z N_i^e \mathrm{d}\boldsymbol{x},
\tag{59}
$$

where $\boldsymbol{F}^e \in \mathbb{R}^3$. In (57) and (58) the magnetic reluctivity and electric conductivity are considered as constant per triangular element. The components of the magnetic flux density are given as follows

$$\begin{aligned} B_{\mathrm{x}}^e &= \frac{\partial {A_{\mathrm{z}}}^e}{\partial y} = \sum_{i=1}^{3} a_{\mathrm{z}i}^e \frac{\partial N_i^e}{\partial y} = \frac{1}{2A^e} \sum_{i=1}^{3} a_{\mathrm{z}i}^e c_i^e \\ B_{\mathrm{y}}^e &= -\frac{\partial {A_{\mathrm{z}}}^e}{\partial x} = -\sum_{i=1}^{3} a_{\mathrm{z}i}^e \frac{\partial N_i^e}{\partial x} = -\frac{1}{2A^e} \sum_{i=1}^{3} a_{\mathrm{z}i}^e b_i^e . \end{aligned} \tag{60}$$

From (60) it is obvious that the magnetic flux density is constant within one triangular element. The same holds for the magnetic field strength vector. The global system of equations can be obtained by assembling the local matrices. By omitting the upper e script it is written as

$$\boldsymbol{K}\boldsymbol{a}(t) + \boldsymbol{M}\frac{\mathrm{d}\boldsymbol{a}(t)}{\mathrm{d}t} = \boldsymbol{F}. \tag{61}$$

For the nonlinear case the stiffness matrix depends on the current solution for the magnetic vector potential, i.e., $\boldsymbol{K} := \boldsymbol{K}(\boldsymbol{a}(t))$.

3.3 Implicit Euler method

The discretization in time domain is carried out by means of the implicit Euler method. After the finite element discretization a system of differential algebraic equations (61) is obtained. Such equations are threated only by implicit methods [39]. We introduce the regular subdivision $\mathscr{T}_T := \{t_n | t_{n+1} > t_n, n = 1, ..., N_T - 1\}$ of $[0, T]$ with a mesh size $\Delta t = t_{n+1} - t_n$. The first order derivative is approximated as

$$\frac{\mathrm{d}\boldsymbol{a}(t_{n+1})}{\mathrm{d}t} \approx \frac{\boldsymbol{a}(t_{n+1}) - \boldsymbol{a}(t_n)}{\Delta t} := \frac{\boldsymbol{a}^{n+1} - \boldsymbol{a}^n}{\Delta t}, \tag{62}$$

where $\boldsymbol{a}^{n+1} := \boldsymbol{a}(t_{n+1})$ and $\boldsymbol{a}^n := \boldsymbol{a}(t_n)$. For simplicity we are going to denote quantities at the time instant t_n with subscript n. The mass matrix will be constant through time and we will avoid denoting time dependency. The global system of equations (61) is now written as

$$\boldsymbol{K}^{n+1}\boldsymbol{a}^{n+1} + \boldsymbol{M}\frac{\boldsymbol{a}^{n+1} - \boldsymbol{a}^n}{\Delta t} = \boldsymbol{F}^{n+1}, \tag{63}$$

where $\boldsymbol{K}^{n+1} := \boldsymbol{K}^{n+1}(\boldsymbol{a}(t_{n+1}))$, $\boldsymbol{F}^{n+1} := \boldsymbol{F}(t_{n+1})$. We can rewrite (63) as

$$(\boldsymbol{K}^{n+1} + \frac{1}{\Delta t}\boldsymbol{M})\boldsymbol{a}^{n+1} = \boldsymbol{F}^{n+1} + \frac{1}{\Delta t}\boldsymbol{M}\boldsymbol{a}^n. \tag{64}$$

When linear electromagnetic properties are considered the solution of (63) is straight forward. In a case of a large system of linear equations, iterative solver such as conjugated gradients can be used. For the nonlinear case we are going to use the Newton-Raphson method.

The dependency of the magnetic reluctivities ν_{xx} and ν_{yy} on the magnetic vector potential, indirectly via the magnetic flux densities, gives rise to a nonlinear problem. The nonlinear problems can be approached for instance by using the fixed point iteration method that is typical slower but provable convergent. On the other hand, the Newton-Raphson method converges faster, see [40]. In this thesis we are going to use the Newton-Raphson method. The notation here is adopted from [41]. First we start with the nonlinear system of equations for the magnetic vector potential in element e at the time step $n+1$ as

$$f_i^{e,n+1}(\boldsymbol{a}^{e,n+1}) := \sum_{p=1}^{3} K_{ip}^{e,n+1} a_{\mathrm{z}p}^{e,n+1} + \frac{1}{\Delta t}\sum_{p=1}^{3} M_{ip}^{e} a_{\mathrm{z}p}^{e,n+1} - F_i^e - \frac{1}{\Delta t}\sum_{p=1}^{3} M_{ip}^{e} a_{\mathrm{z}p}^{e,n}, \tag{65}$$

where $\boldsymbol{a}^{e,n+1} := (a_{\mathrm{z}1}^{e,n+1}, a_{\mathrm{z}2}^{e,n+1}, a_{\mathrm{z}3}^{e,n+1})^T$ for $i = 1,2,3$. We define the following vector

$$\boldsymbol{f}^{e,n+1}(\boldsymbol{a}^{e,n+1}) := \begin{bmatrix} f_1^{e,n+1}(\boldsymbol{a}^{e,n+1}) \\ f_2^{e,n+1}(\boldsymbol{a}^{e,n+1}) \\ f_3^{e,n+1}(\boldsymbol{a}^{e,n+1}) \end{bmatrix}. \tag{66}$$

To proceed we need to compute the local Jacobian matrix in the following form

$$\boldsymbol{J}^{e,n+1,k} = \begin{bmatrix} \frac{\partial f_1^{e,n+1,k}}{\partial a_{\mathrm{z}1}^{e,n+1,k}} & \frac{\partial f_1^{e,n+1,k}}{\partial a_{\mathrm{z}2}^{e,n+1,k}} & \frac{\partial f_1^{e,n+1,k}}{\partial a_{\mathrm{z}3}^{e,n+1,k}} \\ \frac{\partial f_2^{e,n+1,k}}{\partial a_{\mathrm{z}1}^{e,n+1,k}} & \frac{\partial f_2^{e,n+1,k}}{\partial a_{\mathrm{z}2}^{e,n+1,k}} & \frac{\partial f_2^{e,n+1,k}}{\partial a_{\mathrm{z}3}^{e,n+1,k}} \\ \frac{\partial f_3^{e,n+1,k}}{\partial a_{\mathrm{z}1}^{e,n+1,k}} & \frac{\partial f_3^{e,n+1,k}}{\partial a_{\mathrm{z}2}^{e,n+1,k}} & \frac{\partial f_3^{e,n+1,k}}{\partial a_{\mathrm{z}3}^{e,n+1,k}} \end{bmatrix}, \tag{67}$$

where with the superscript k the Newton-Raphson step is denoted. The elements are computed as

$$J_{ij}^{e,n+1,k} := \frac{\partial f_i^{e,n+1,k}}{\partial a_{\mathrm{z}j}^{e,n+1,k}} = K_{ij}^{e,n+1,k} + \frac{1}{\Delta t} M_{ij} + \sum_{p=1}^{3} \frac{\partial K_{ip}^{e,n+1}}{\partial a_{\mathrm{z}j}^{e,n+1,k}} a_{\mathrm{z}p}^{e,n+1,k}. \tag{68}$$

We provide detailed expression for the derivative of the stiffness elements w.r.t. the magnetic vector potential as

$$\frac{\partial K_{ip}^{e,n+1}}{\partial a_{\mathrm{z}j}^{e,n+1,k}} = \frac{\partial \nu_{\mathrm{yy}}^{e,n+1,k}}{\partial B_{\mathrm{y}}^2} \frac{\partial B_{\mathrm{y}}^2}{\partial a_{\mathrm{z}j}^{e,n+1,k}} \frac{b_i^e b_p^e}{4A^e} + \frac{\partial \nu_{\mathrm{xx}}^{e,n+1,k}}{\partial B_{\mathrm{x}}^2} \frac{\partial B_{\mathrm{x}}^2}{\partial a_{\mathrm{z}j}^{e,n+1,k}} \frac{c_i^e c_p^e}{4A^e}. \tag{69}$$

The derivatives of the magnetic flux densities squared are given as

$$\frac{\partial B_{\mathrm{x}}^2}{\partial a_{\mathrm{z}j}^{e,n+1,k}} = \frac{2}{A^e} \sum_{q=1}^{3} \frac{c_q^e c_j^e}{4A^e} a_{\mathrm{z}q}^{e,n+1,k}, \tag{70}$$

and

$$\frac{\partial B_{\mathrm{y}}^2}{\partial a_{\mathrm{z}j}^{e,n+1,k}} = \frac{2}{A^e}\sum_{q=1}^{3}\frac{b_q^e b_j^e}{4A^e} a_{\mathrm{z}q}^{e,n+1,k}. \tag{71}$$

By substituting (70), (71) and (69) into (68) the local Jacobian element is computed as follows

$$J_{ij}^{e,n+1,k} = K_{ij}^{e,n+1,k} + \frac{1}{\Delta t}M_{ij} + \frac{2}{A^e}P_{ij}^{e,n+1,k}, \tag{72}$$

where

$$P_{ij}^{e,n+1,k} = \frac{\partial \nu_{\mathrm{yy}}^{e,n+1,k}}{\partial B_{\mathrm{y}}^2}\sum_{p=1}^{3}\sum_{q=1}^{3}\frac{b_p^e b_i^e}{4A^e}\frac{b_q^e b_j^e}{4A^e}a_{\mathrm{z}p}^{e,n+1,k}a_{\mathrm{z}q}^{e,n+1,k} + \frac{\partial \nu_{\mathrm{xx}}^{e,n+1,k}}{\partial B_{\mathrm{x}}^2}\sum_{p=1}^{3}\sum_{q=1}^{3}\frac{c_p^e c_i^e}{4A^e}\frac{c_q^e c_j^e}{4A^e}a_{\mathrm{z}p}^{e,n+1,k}a_{\mathrm{z}q}^{e,n+1,k} \tag{73}$$

$$\boldsymbol{J}^{e,n+1,k} = \boldsymbol{K}^{e,n+1,k} + \frac{1}{\Delta t}\boldsymbol{M}^e + \frac{2}{A^e}\boldsymbol{P}^{e,n+1,k} \tag{74}$$

where

$$\boldsymbol{P}^{e,n+1,k} = \frac{\partial \nu_{\mathrm{yy}}^{e,n+1,k}}{\partial B_{\mathrm{y}}^2}\boldsymbol{P}_{\mathrm{x}}\boldsymbol{a}^{e,n+1,k}(\boldsymbol{P}_{\mathrm{x}}\boldsymbol{a}^{e,n+1,k})^T + \frac{\partial \nu_{\mathrm{xx}}^{e,n+1,k}}{\partial B_{\mathrm{x}}^2}\boldsymbol{P}_{\mathrm{y}}\boldsymbol{a}^{e,n+1,k}(\boldsymbol{P}_{\mathrm{y}}\boldsymbol{a}^{e,n+1,k})^T. \tag{75}$$

The elements of the matrices $\boldsymbol{P}_{\mathrm{x}}$ and $\boldsymbol{P}_{\mathrm{y}}$ are computed as

$$P_{\mathrm{x}ij} := \frac{b_i^e b_j^e}{4A^e}, \tag{76}$$

$$P_{\mathrm{y}ij} := \frac{c_i^e c_j^e}{4A^e}. \tag{77}$$

After assembly of the local matrices (74) and (66) the following system of equations is obtained

$$\boldsymbol{J}^{n+1,k}\Delta\boldsymbol{a}^{n+1,k+1} = -\boldsymbol{f}(\boldsymbol{a}^{n+1,k}), \tag{78}$$

where $\Delta\boldsymbol{a}^{n+1,k+1} = \boldsymbol{a}^{n+1,k+1} - \boldsymbol{a}^{n+1,k}$. The iteration is terminated when the relative error meets a prescribed tolerance value given as

$$\frac{||\boldsymbol{a}^{n+1,k+1} - \boldsymbol{a}^{n+1,k}||_{l_2}}{||\boldsymbol{a}^{n+1,k+1}||_{l_2}} < \mathrm{tol}, \tag{79}$$

where l_2 is the Euclidean norm.

3.5 Numerical examples

Two benchmark examples will be used throughout the thesis in order to illustrate the technical relevance of the proposed methodology. Namely, we will consider a single phase transformer, see [43] and a combined function magnet. The inductance of the primary coil and the field harmonics will be considered as QoIs in the first and the second example, respectively. The computational domain D is discretized by the open source mesh generator called triangle [44] within the FEMM 4.2 software [45]. For the computation of the stiffness and the mass matrix we use our own inhouse code.

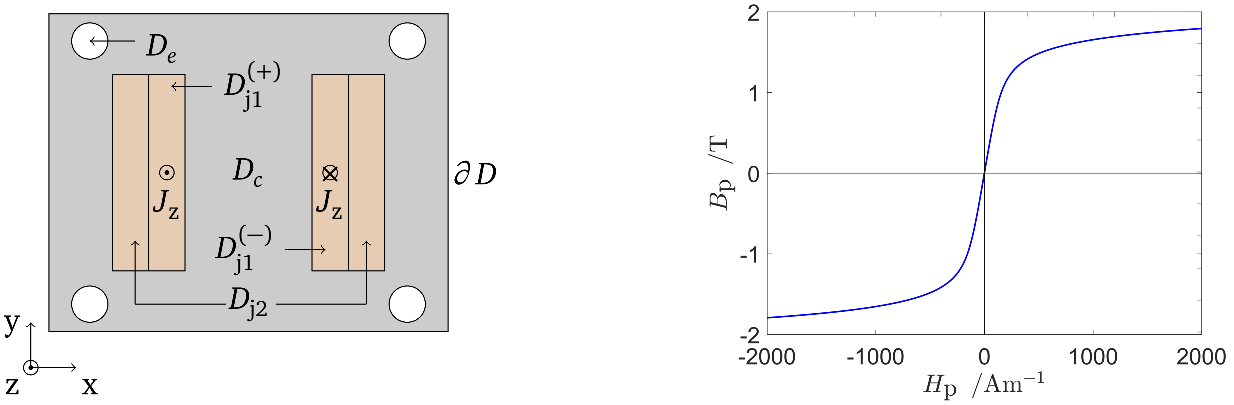

(a) Single phase transformer

(b) Nonlinear $B-H$ curve obtained by the Brauer model [42]

Figure 8: Single phase transformer from [43] (a). Nonlinear $B-H$ curve obtained by the Brauer model for $k_{1\mathrm{p}} = 6\mathrm{H/m}$, $k_{2\mathrm{p}} = 2T^{-2}$ and $k_{3\mathrm{p}} = 120\mathrm{H/m}$ (b)

3.5.1 Single phase transformer

The single phase transformer is depicted in Fig. 8a. It consist of a ferromagnetic core, primary and secondary coil which are denoted as D_c, D_j1 and D_j2, respectively. The details on the geometry of the transformer can be found in [43].

3.5.2 Inductance computation in the linear case

One of the properties that is relevant for such a device is for instance the self inductance. We will refer to it as just an inductance, of the primary or the secondary coil. For the linear case the inductance does not depend on the electric current. For the computation of the inductance we use the following relation

$$L = \boldsymbol{P}_\mathrm{str}^T \boldsymbol{K}^{-1} \boldsymbol{P}_\mathrm{str} \tag{80}$$

where $\boldsymbol{P}_\mathrm{str}$ is the stranded conductor coupling vector, see [46]. We set the number the number of turns $N_\mathrm{j} = 260$ and the electric current to $I_\mathrm{j} = 1A$. The magnetic reluctivity is homogeneous and its value is $\nu = 500\mathrm{Hm}^{-1}$. The computational domain is discretized with $N_\mathrm{t} = 25713$ triangles. The length in z-direction is set to unity. The computed value for the inductance is per unit length. The obtained value in this case is $26.174\mathrm{H/m}$

3.5.3 Inductance computation in the nonlinear case

For the nonlinear case we solve the transient for a given electric current signal. We excite the primary coil with a sinusoidal current $I_\mathrm{j}(t) = I_0 \sin(\omega t)$, where $I_0 = 0.12A$ and $\omega = \pi\,\mathrm{rad/s}$. The conductivity in the core domain is $2.9\mathrm{MS}$. The error tolerance for the Newton-Raphson procedure is set to 10^{-6}. For simplicity we are going to assume that the same material law governs in both x and y direction and we will use the Brauer model [42], given with the following equation:

$$H_\mathrm{p}(B_\mathrm{p}) = \left(k_{1\mathrm{p}} e^{k_{2\mathrm{p}} B_\mathrm{p}^2} + k_{3\mathrm{p}}\right) B_\mathrm{p}, \tag{81}$$

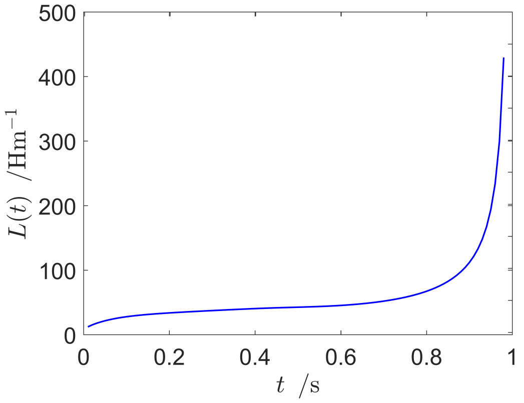

Figure 9: Transient inductance

where $k_{1\mathrm{p}} = 6\mathrm{H/m}$, $k_{2\mathrm{p}} = 2T^{-2}$ and $k_{3\mathrm{p}} = 120\mathrm{H/m}$, to compute the magnetic reluctivity. The corresponding $B-H$ curve is shown in Fig. 8b. The time step is $\Delta t = 0.02\mathrm{s}$. The corresponding magnetic reluctivity is given as

$$\nu_{\mathrm{pp}}(B_{\mathrm{p}}) = \left(k_{1\mathrm{p}} e^{k_{2\mathrm{p}} B_{\mathrm{p}}^2} + k_{3\mathrm{p}}\right). \tag{82}$$

The inductance, for $I_{\mathrm{j}}(t) \neq 0$, is a function of time and it is computed as

$$L(t) = \boldsymbol{P}_{\mathrm{str}}^T \boldsymbol{K}(\boldsymbol{a}(t))^{-1} \boldsymbol{P}_{\mathrm{str}}, \tag{83}$$

and its graph is shown in Fig. 9 in the interval $T = [0,1]$s. The Brauer model for the magnetic reluctivity should be used with caution because it does not model the saturation properties of the magnetic materials. According to (82) we observe that

$$\lim_{\boldsymbol{B}_{\mathrm{p}} \to \infty} \left(k_{1\mathrm{p}} e^{k_{2\mathrm{p}} B_{\mathrm{p}}^2} + k_{3\mathrm{p}}\right) = \infty, \tag{84}$$

but in reality this limit should be a finite constant value.

3.5.4 Combined function magnet

A combined function magnet is a device that is used in accelerators to deflect a beam of charged particles. Such kind of magnets are considered in the center for heavy ion research GSI [47] within the FAIR [48] project. The advantage of using a combined function magnet as technical solution is that it achieves both, vertical and horizontal deflection as a single device. Thus, the spatial requirements are reduced and the costs of building two separate magnets to achieve the same functionality. The 2D cross section of a combined function magnet is depicted in Fig. 10.

The device consists of steerer and switching coils. Both coils are placed around a ferromagnetic yoke. The surrounding medium is air. The beam of charged particles enters in the center part of the magnetic yoke. Before being deflected it is moving perpendicular to the 2D cross section. When the coils are switched on, the beam is in the presence of a magnetic field and it experiences a Lorentz force computed as

$$\boldsymbol{F}_L = q \cdot v \times \boldsymbol{B}, \tag{85}$$

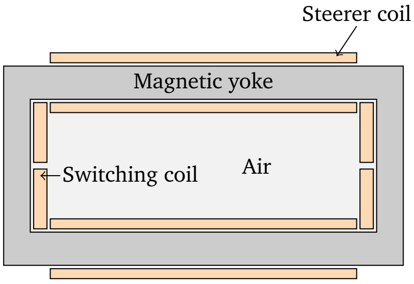

Figure 10: 2D cross section of a combined function magnet

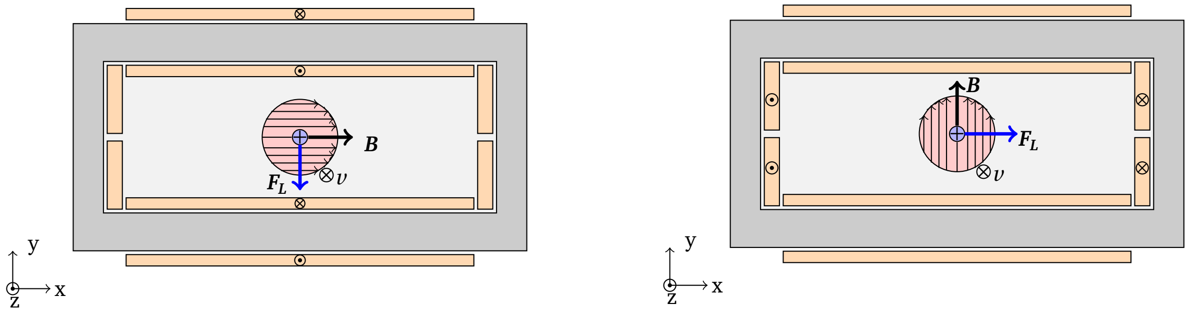

(a) Steering mode

(b) Switching mode

Figure 11: A combined function magnet in steer (a) and switching mode (b)

where q is the electrical charge, v is the velocity of the beam, $\boldsymbol{B}$ is the magnetic flux density and $\boldsymbol{F}_L$ is the Lorentz force. The horizontal and vertical deflection are achieved when the switching and steerer coils are switched on solely, respectively. This working principle is described in Fig. 11 for both, the switching Fig. 11b and steering Fig. 11a mode, respectively.

In order to keep the beam on its intended trajectory there is a high demand for field homogeneity inside the aperture. The combined function magnet falls into the category iron dominated magnets. This classification is mainly related to the fact that the field homogeneity is highly influenced by the magnetic behavior law of the yoke. There are so called coil dominated magnet where the field is mainly shaped by the coils. Comprehensive theoretical study of both types of magnets can be found in [49]. The field homogeneity is also known as a field quality for which detailed explanation is given in the section that follows.

3.5.5 Field quality

The field quality is quantitatively expressed via the Fourier coefficients of the radial component of the magnetic flux density, also known as field harmonics, on a given reference radius r_0 as shown in Fig. 12. For sake of clarity we derive the expression for numerical computation of the field harmonics as it is done in [49]. First the Fourier-series expansion of A_z, inside the aperture, is given in cylindrical coordinates as

$$A_z(r_0,\phi) = \sum_{k=1}^{\infty}(\mathcal{T}_k(r_0)\cos(k\phi)+\mathcal{E}_k(r_0)\sin(k\phi)), \tag{86}$$

where $\mathcal{T}_k$ and $\mathcal{E}_k$ are the Fourier coefficients computed as follows:

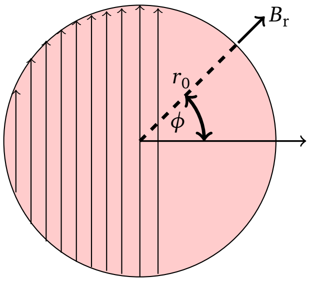

Figure 12: Radial component of the magnetic flux density on a reference circle

$$\begin{aligned}\mathscr{T}_k(r_0) &= \frac{1}{2\pi}\int_0^{2\pi} A_z(r_0,\phi)\cos(k\phi)\mathrm{d}\phi,\\ \mathscr{E}_k(r_0) &= \frac{1}{2\pi}\int_0^{2\pi} A_z(r_0,\phi)\sin(k\phi)\mathrm{d}\phi.\end{aligned} \tag{87}$$

In computational practice a discrete Fourier transform DFT is computed of the magnetic vector potential at the reference radius r_0 at N_p discrete points in the interval $[0,2\pi]$,

$$A_z^{\mathrm{DFT}} = \sum_{n=0}^{N_p-1} A_z(r_0,\phi_n)e^{-j\phi_n k}, \tag{88}$$

where $\phi_n = \frac{2\pi}{N_p}n$. The Fourier coefficients $\mathscr{T}_k$ and $\mathscr{E}_k$ are computed via the real and the imaginary part of A_z^{DFT} as follows:

$$\mathscr{T}_k(r_0) \approx \frac{1}{N_p}\mathrm{Re}(A_z^{\mathrm{DFT}}) = \frac{1}{N_p}\sum_{n=0}^{N_p-1} A_z(r_0,\phi_n)\cos(k\phi_n), \tag{89}$$

$$\mathscr{E}_k(r_0) \approx -\frac{1}{N_p}\mathrm{Im}(A_z^{\mathrm{DFT}}) = \frac{1}{N_p}\sum_{n=0}^{N_p-1} A_z(r_0,\phi_n)\sin(k\phi_n). \tag{90}$$

The radial component of the magnetic flux density is computed as:

$$B_r(r_0,\phi) = \sum_{k=1}^{\infty}(B_k(r_0)\sin(k\phi) + A_k(r_0)\cos(k\phi)), \tag{91}$$

where B_k and A_k are known as normal and skew multipole coefficients respectively and they are computed via $\mathscr{T}_k$ and $\mathscr{E}_k$ as follows:

$$\begin{aligned}B_k(r_0) &= -\frac{n\mathscr{T}_k(r_0)}{r_0},\\ A_k(r_0) &= \frac{n\mathscr{E}_k(r_0)}{r_0}.\end{aligned} \tag{92}$$

A good design typically requires $B_1/B_k < 10^{-4}$, for $k > 1$

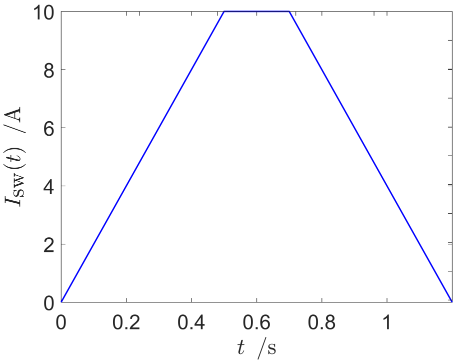

Figure 13: Ramping signal

3.5.6 Field quality computation

We are going to consider transient analysis for both, linear and nonlinear case, respectively. For simplicity we will consider only the switching mode, i.e., the electric current will be set to zero in the steerer coils. The device is captured in a circular computational domain with radius of 0.27m. The details about the geometry of the magnet can be found in [50]. The z-component of the magnetic vector potential is set to zero on the boundary. We shall denote the number of turns in the switching and steerer coil as N_{sw} and N_{st}, respectively. The currents which will be imposed by the source are denoted as I_{sw} and I_{st}. For this computations $N_{\mathrm{sw}} = 450$ and $N_{\mathrm{st}} = 260$. The number of triangles is $N_{\mathrm{t}} = 32459$. The same materials laws are hold here as in the previous example. Typical current excitation profiles for transient analysis of accelerator magnets can be found for example in [51]. Here we will consider the ramping signal shown in Fig. 13. The transient behavior of the first and third harmonic in the linear and nonlinear case is depicted in Fig. 14.

3.6 Conclusion

In this section we derived the finite element approximation of the governing equations. The temporal discretization was carried out by means of the implicit Euler method. Moreover, we addressed the nonlinear magnetoquasistatic problem by the Newton-Raphson method. Numerical results were presented related to a single phase transformer and a combined function magnet.

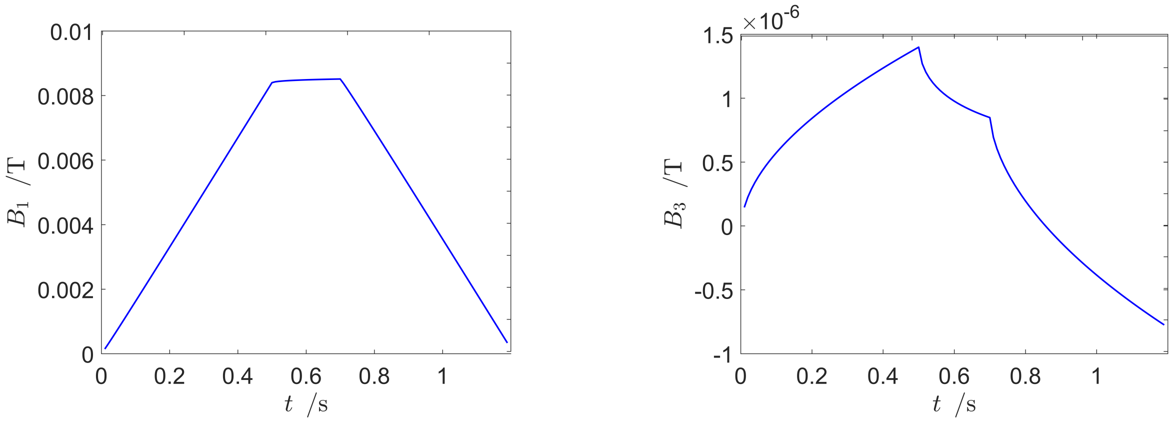

(a) First harmonic in the linear case

(b) Third harmonic in the linear case

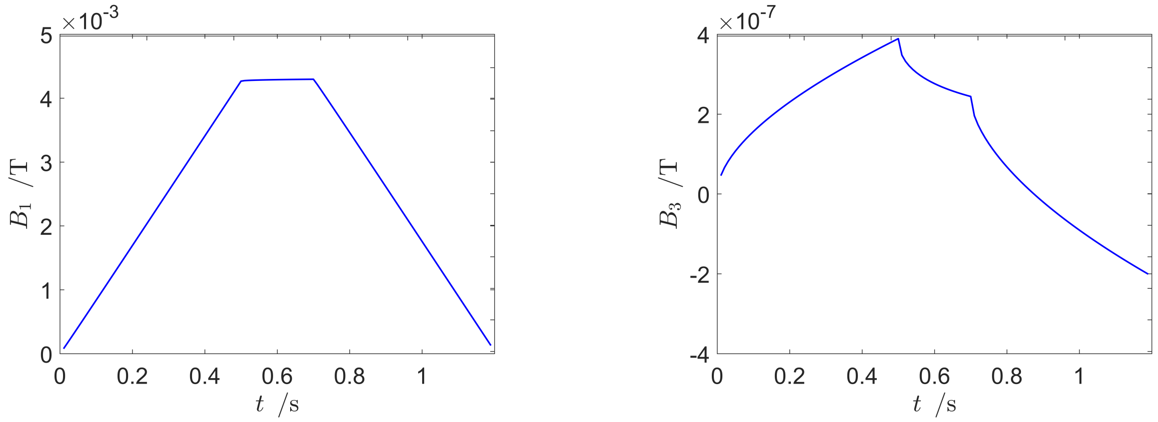

(c) First harmonic in the nonlinear case

(d) Third harmonic in the nonlinear case

Figure 14: Transient field harmonics for the linear (a)-(b) and nonlinear (c)-(d) case

4 Uncertainty Quantification

In this chapter we give a brief overview of the theory of random fields. We will cover the univariate case and its extension to the mutlivariate case. Spatial random fields will be also introduced. A Detailed description of the stochastic collocation method will be also given.

4.1 Modeling uncertainties by random fields

There are two types of uncertainties addressed in this thesis. The first type will be related to material curves. The second type, also called spatial uncertainties, will be related to the magnetic reluctivity when is considered as inhomogeneous, i.e., it depends on spatial coordinates. We start with one dimensional random field related to a single material curve. Before we proceed, we need to introduce the concept of probability space and random variables.

4.1.1 Probability space and random variables

Let us define a probability space $(\Omega, \mathscr{F}, P)$, see [4, Chapter 2], where Ω is the sample space, $\mathscr{F}$ the sigma algebra and P is the probability measure on $\mathscr{F}$. The sample space contains all possible random realization which we will denote with $\theta \in \Omega$. A real valued random variable $Y : \Omega \to \mathbb{R}$ is a measurable function from a set of possible outcomes Ω to the set of real numbers $\mathbb{R}$. For any particular choice of θ, $Y(\theta)$ is called random realization. The mean value, i.e., the expected value of the random variable Y is defined as

$$\mathbb{E}(Y) := \int_{\Omega} Y(\theta) \mathrm{d}P(\theta). \tag{93}$$

We will consider only the space of second order random variables denoted as $L_2(\Omega, P)$ defined in $(\Omega, \mathscr{F}, P)$ equipped with inner product $\langle \cdot, \cdot \rangle_{L_2(\Omega,P)}$ and associated norm $|| \cdot ||_{\Omega}$ given as

$$\langle X, Y \rangle_{L_2(\Omega,P)} := \int_{\Omega} X(\theta) Y(\theta) \mathrm{d}P(\theta) = \mathbb{E}(XY), \tag{94}$$

and

$$||Y||_{\Omega}^2 := \langle Y, Y \rangle_{L_2(\Omega,P)} < \infty, \tag{95}$$

respectively. A covariance between two random variables is defined as follows

$$\mathrm{Cov}(Y_1, Y_2) := \mathbb{E}\left((Y_1 - \mathbb{E}(Y_1))(Y_2 - \mathbb{E}(Y_2))\right) = \mathbb{E}(Y_1 Y_2) - \mathbb{E}(Y_1)\mathbb{E}(Y_2). \tag{96}$$

Two random variables are uncorrelated if the covariance between them is zero, i.e., the joint expected value can be expressed as

$$\mathbb{E}(Y_1 Y_2) = \mathbb{E}(Y_1)\mathbb{E}(Y_2). \tag{97}$$

The probability that the random variable Y takes a value in the interval $[a, b]$ is given by

$$P(a \leq Y \leq b) = \int_a^b \rho_Y(y) \mathrm{d}y = F_Y(b) - F_Y(a), \tag{98}$$

where ρ_Y is the PDF, which we assume that it exists, and F_Y is the cumulative distribution function (CDF), respectively. A collection of random variables defines a random vector $\boldsymbol{Y} = (Y_1, ..., Y_M)$. The probability that the random vector obtains value in $[a_1, b_1] \times ... \times [a_M, b_M]$ is computed as

$$P(a_1 \leq Y_1 \leq b_1, ..., a_M \leq Y_M \leq b_M) = \int_{a_1}^{b_1} ... \int_{a_M}^{b_M} \rho_Y(y_1, ..., y_M) \mathrm{d}y_1 ... \mathrm{d}y_M, \tag{99}$$

where ρ_Y is the joint PDF. The random variables $\{Y_i\}_{i=1}^{M}$ are independent if the joint pdf can be decomposed as product of the univariate ones

$$\rho_Y(\boldsymbol{y}) = \prod_{i=1}^{M} \rho_{Y_i}(y_i), \tag{100}$$

where $\boldsymbol{y} = (y_1, ..., y_M)$. If there is a function $g(\cdot)$ that takes the random vector $\boldsymbol{Y}$ as an input then its mean value is computed as

$$\mathbb{E}(g(\boldsymbol{Y})) = \int_{\Gamma} g(\boldsymbol{y}) \rho_Y(\boldsymbol{y}) \mathrm{d}\boldsymbol{y}, \tag{101}$$

where $\Gamma = \Gamma_1 \times, ..., \times \Gamma_M$ and $\Gamma_i = \left[y_i^{\min}, y_i^{\max}\right]$ is the image of the i-th random variable.

4.1.2 Univariate random field

Let us consider two functions $F_1 : I \to \mathbb{R}$ and $F_2 : I \to \mathbb{R}$, where $I \subset \mathbb{R}$, as depicted in Fig. 15. In a deterministic sense they represent two different mappings. However, for the point s_1 the two different values $F_1(s_1)$ and $F_2(s_1)$, are interpreted as two different random realizations $Y_{s_1}(\theta_1)$ and $Y_{s_1}(\theta_2)$, of the same random variable Y_{s_1}. Similarly, the two different values at the point s_2, given as $F_1(s_2)$ and $F_2(s_2)$, are two random realizations $Y_{s_2}(\theta_1)$ and $Y_{s_2}(\theta_2)$ of the random variable Y_{s_2}. Alternatively, one can think that the two random realizations θ_1 and θ_2 produce two different mappings. This interpretation brings us to the concept of real valued random field. A real valued random field is a mapping that takes the elements of the Cartesian product $I \times \Omega$ and maps them into the set of real numbers $\mathbb{R}$. The mapping is given as

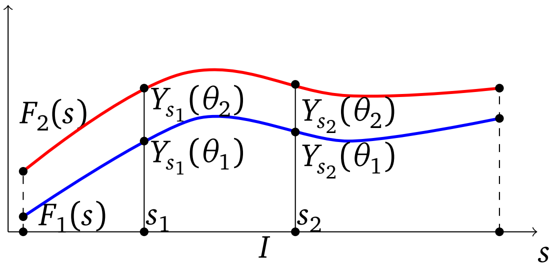

Figure 15: Random variables on material curves

$$F : I \times \Omega \to \mathbb{R}, \tag{102}$$

where $F \in L_2(I \times \Omega)$. The space of square integrable random fields is denoted as $L_2(I \times \Omega) = L_2(I) \times L_2(\Omega, P)$. The above description can be summarized as follows: for each particular choice of $s \in I$, $F(s, \cdot)$ is a random variable w.r.t. the probability space $(\Omega, \mathscr{F}, P)$ and for each random realization $\theta \in \Omega$, $F(\cdot, \theta)$ yields a mapping on I. The mean value of the random field is given as

$$\overline{F}(s) = \mathbb{E}(F(s, \theta)), \tag{103}$$

and its covariance function

$$K_F(s,t) = \mathbb{E}\left(\left(F(s,\theta) - \overline{F}(s)\right)\left(F(t,\theta) - \overline{F}(t)\right)\right). \tag{104}$$

The correlation function is computed by using the covariance function as

$$\mathrm{Cor}_F(s,t) = \frac{K_F(s,t)}{\sqrt{K_F(s,s)}\sqrt{K_F(t,t)}}, \tag{105}$$

The covariance function can be determined from experimental data as a sample covariance. In this case it is referred to as the sample covariance. In order to incorporate the random field into numerical simulation, discretization is necessary. This is achieved via the truncated KLE. In the next subsection the KLE is introduced.

4.1.3 Karhunen-Loève expansion

The second order random field (102) admits the following orthogonal decomposition:

$$F(s,\theta) = \overline{F}(s) + \sum_{i=1}^{\infty} \sqrt{\lambda_i}\phi_i(s) Y_i(\theta). \tag{106}$$

In (106) Y_i are orthonormal random variables w.r.t. the probability space, i.e., they satisfy

$$\mathbb{E}(Y_i Y_j) = \delta_{ij}, \tag{107}$$

where δ_{ij} is the Kronecker delta function defined as

$$\delta_{ij} = \begin{cases} 1 & i = j, \\ 0 & i \neq j. \end{cases} \tag{108}$$

With λ_i and ϕ_i are denoted the i-th eigenvalue and eigenfunction, respectively, that will be introduced in shortly. The eigenfunctions are orthonormal

$$\int_I \phi_i(s)\phi_j(s)\mathrm{d}s = \delta_{ij}. \tag{109}$$

Starting from (106) the zero mean of the expansion can be expressed as

$$F(s,\theta) - \overline{F}(s) = \sum_{i=1}^{\infty} \sqrt{\lambda_i}\phi_i(s) Y_i(\theta). \tag{110}$$

When (110) is substituted into (104) it is obtained that

$$K_F(s,t) = \sum_{i=1}^{\infty}\sum_{j=1}^{\infty} \sqrt{\lambda_i}\sqrt{\lambda_j}\phi_i(s)\phi_j(t)\mathbb{E}\left(Y_i(\theta)Y_j(\theta)\right), \tag{111}$$

which due to the orthonormality simplifies to

$$K_F(s,t) = \sum_{i=1}^{\infty} \lambda_i \phi_i(s)\phi_i(t). \tag{112}$$

The orthonormality of the eigenfunction is exploited such that the Fredholm integral equation is derived as follows

$$\int_I K_F(s,t)\,\phi_i(s)\mathrm{d}s = \lambda_i \underbrace{\int_I \phi_i^2(s)\mathrm{d}s}_{=1}\,\phi_i(t). \tag{113}$$

In order to obtain the eigenvalues and the eigenfunction of the KLE one has to solve the Fredholm integral equation given as

$$\int_I K_F(s,t)\,\phi_i(s)\mathrm{d}s = \lambda_i\phi_i(t). \tag{114}$$

The random field $F(\cdot,\cdot)$ is approximated with a finite number of random variables by using the truncated KLE

$$F_M(s,\boldsymbol{Y}) = \overline{F}(s) + \sum_{i=1}^{M} \sqrt{\lambda_i}\phi_i(s)Y_i(\theta). \tag{115}$$

The orthogonal decomposition given by (115) yields a minimal error, in the mean square sense, compared to any other $M-$term expansion, for instance polynomial chaos expansion. The error due to the truncation is given via the eigenvalues as follows:

$$||F_M - F||^2_{L_2(I\times\Omega)} = \sum_{i=M+1}^{\infty} \lambda_i. \tag{116}$$

The relative error is estimated as

$$e_M = \frac{||F_M - F||^2_{L_2(I\times\Omega)}}{||F||^2_{L_2(I\times\Omega)}} = \sqrt{\frac{\sum_{i\geq M+1}\lambda_i}{\sum_{i\geq 1}\lambda_i}}. \tag{117}$$

One popular criterion for choosing the number of random variables is the so called relative information criterion. It is given as follows

$$\Psi_M = \frac{\sum_{i=1}^{M}\lambda_i}{\sum_{i\geq 1}\lambda_i} \geq 0.95. \tag{118}$$

We will use this criterion later in Chapter 6.

4.1.4 The Fredholm integral equation

The Fredholm integral equation has an analytical solution for a particular choice of covariance kernel such as the exponential, see [3, Chapter 2,p. 22] and [52, Chapter 4,p. 48]. However, in general, when the covariance function is computed from experimental data and does not belong to a particular family of functions, it has to be solved numerically. The unknowns are the eigenfunctions and the eigenvalues. In order to solve (114) we multiply both sides of the equation with a test function $\mathrm{v}(\cdot)$ and integrate over the domain I

$$\int_I \int_I K_U(s,t)\phi_i(s)\mathrm{v}(s)\mathrm{d}s\mathrm{d}t = \lambda_i \int_I \phi_i(t)\mathrm{v}(t)\mathrm{d}t, \tag{119}$$

where $\mathrm{v} \in L_2(I)$. The unknown eigenfunctions are approximated as

$$\phi_i(s) = \sum_{k=1}^{N} \phi^F_{ik} N^F_k(s), \tag{120}$$

where ϕ^F_{ik} are the unknown coefficients to be determined and $N^F_k \in \mathscr{L}^{p,q}_N$. We consider $\mathscr{L}^{3,0}_N$ to be a set of cubic B-splines, see Appendix C for details. The material functions usually have some smoothness requirements which are same for the eigenfunctions. Therefor we have chosen to approximate them with the differentiable cubic splines. When (120) is substituted into (114) and the Galerkin method is applied, i.e., $\mathrm{v} \in \mathscr{L}^{3,0}_N$, the following generalized eigenvalue problem is obtained

$$\boldsymbol{A}\boldsymbol{\phi}_i = \lambda_i \boldsymbol{B}\boldsymbol{\phi}_i, \tag{121}$$

where the element of the matrices $\boldsymbol{A}$ and $\boldsymbol{B}$ are computed as

$$A_{ij} = \int_I \int_I K_F(s,t) N^F_k(s) N^F_k(t)\mathrm{d}t\mathrm{d}s, \tag{122}$$

and

$$B_{ij} = \int_I N^F_k(t) N^F_k(t)\mathrm{d}t, \tag{123}$$

respectively. Both, $\mathbb{A}$ and $\mathbb{B}$ are symmetric matrices.

4.1.5 The random variables in the Karhunen-Loève expansion

There are infinitely many random fields that share the same covariance function. This can be seen for example from (111). As long as $\mathbb{E}(Y_i Y_j) = \delta_{ij}$ in (111) the same covariance function is obtained regardless to the PDF. What distinguishes two random fields with same covariance kernel are the PDFs of the random variables in the KLE. For Gaussian random fields the uncorrelatedness of the random variables implies independence. However, in general this does not hold, i.e., uncorrelated random variables can be dependent. Within this thesis we are going to assume independence.

By exploiting the orthonormality of the eigenfunctions in (106) the random variables can be expressed as

$$Y_i(\theta) = \frac{1}{\sqrt{\lambda_i}} \int_I \left(F(s,\theta) - \overline{F}(s)\right) \phi_i(s) \mathrm{d}s. \tag{124}$$

The link between the experimental data and the random variables in the KLE is established via (124). A set of experimental values $\{Y_i^j\}_{j=1}^{N_s}$, where $Y_i^j := Y_i(\theta_j)$, can be obtained when a set of experimental data $\{F(s,\theta_j)\}_{j=1}^{N_s}$ is available. In practice the random field can be known at a finite number of points $\{F(s_i,\cdot)\}_{i=1}^{N_\mathrm{p}}$. The continuous representation is obtained via interpolation. There are two approaches to estimate a PDF of a random variable, parametric and nonparametric. The parametric approach requires that a family of PDFs is chosen. The unknown parameters of the chosen family are then estimated, e.g., by using the maximum likelihood principle. The nonparametric approach on the other hand does not require any assumption on the PDF. The most popular nonparametric approach is the kernel density estimation method, see [53, 54, 55, 56]. The estimate of the PDF for the univariate case is given as

$$\hat{\rho}_{Y_i}(y_i,h_i) = \frac{1}{N_s h_i} \sum_{j=1}^{N_s} K\left(\frac{y_i - Y_i^j}{h_i}\right), \tag{125}$$

where h_i is a smoothing parameter and K is the kernel estimator function, see [57]. The choice of the smoothing parameter is not a trivial task and it plays a crucial role, see [57, 58]. One criterion based on which the smoothing parameter can be estimated is the mean integrated square error (MISE) given as

$$\mathrm{MISE}(\hat{\rho}_{Y_i}) = \mathbb{E}(\int_\Gamma (\hat{\rho}_{Y_i}(y_i,h_i) - \rho_{Y_i}(y_i))^2 \mathrm{d}y_i). \tag{126}$$

An adaptive algorithm for the choice of h_i and estimation of the PDF based on the MISE has been developed in [59]. The random variables are independent and therefore,

$$\hat{\rho}_{\boldsymbol{Y}}(\boldsymbol{y}) = \prod_{i=1}^{M} \hat{\rho}_{Y_i}(y_i). \tag{127}$$

where $\hat{\rho}_{Y_i}(y_i) := \hat{\rho}_{Y_i}(y_i,h_i)$. In this thesis we are going to use the adaptive kernel density estimation method.

4.2 Numerical example for univariate random field

We consider a univariate random field described by its mean value $\overline{F}(s) = e^s$ on the interval $I = [0,2]$. For simplicity of notation units will be avoided here. The covariance function is given as

$$K_F(s,t) = \sigma e^{-\frac{|s-t|}{d}}, \tag{128}$$

where σ is the variance and d is the correlation length of the random field, respectively. For the numerical experiment here the variance is $\sigma = 10$ and the values $d = 0.5, 1, 10$ will be

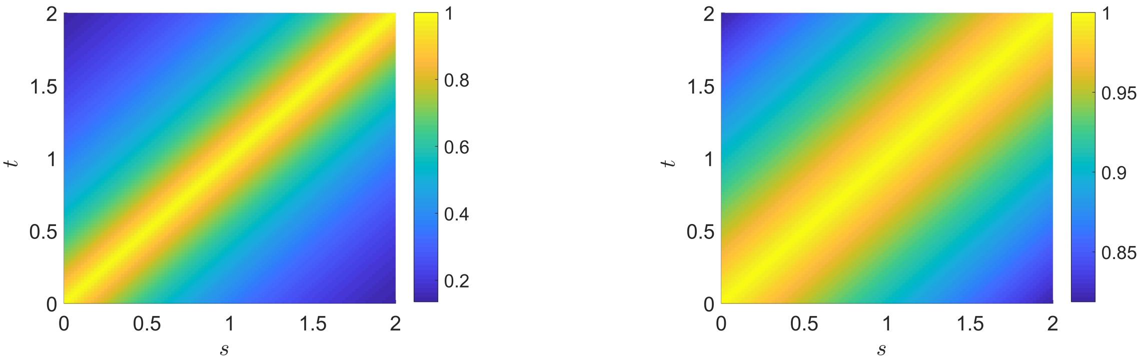

(a) Correlation function for $d = 1$

(b) Correlation function for $d = 10$

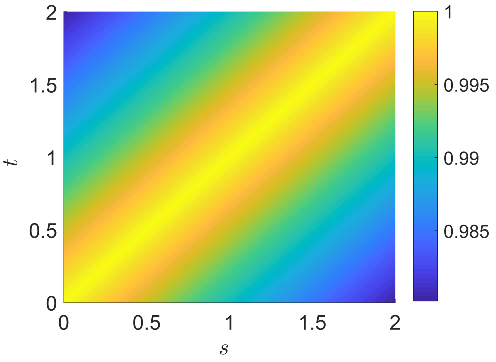

(c) Correlation function for $d = 100$

Figure 16: The correlation functions for $d = 1$ (a), $d = 10$ (b) and $d = 100$ (c)

considered. For all of the numerical examples we will assume that the random variables have a uniform PDF, i.e., $Y_i \sim \mathscr{U}(-\sqrt{3}, \sqrt{3})$. The correlation functions for the different correlation lengths are shown in Fig. 16.

The eigenvalues and the eigenfunctions that correspond to the different correlation lengths are shown in Fig. 18 and Fig. 17 , respectively. One can see from Fig. 18 that the decay of the eigenvalues is influenced by the correlation length. Namely for stronger correlation length a faster decay is observed and vice versa. In order to achieve the same order of accuracy a different number of random variables have to be taken into account. For instance, by using (117) as an estimate, one has to take $M = 3, 5, 15$ to approximate the random field $F(\cdot, \cdot)$ up to a relative error of $0.24, 0.9, 0.53\%$, respectively.

We can distinguishe weakly from strongly correlated random fields by observing the random realizations in Fig. 19. Roughly speaking, weakly correlated random field have more oscillatory behavior, see Fig. 19a, in comparison to strongly correlated, see Fig. 19c. We will use this guideline later in discussion.

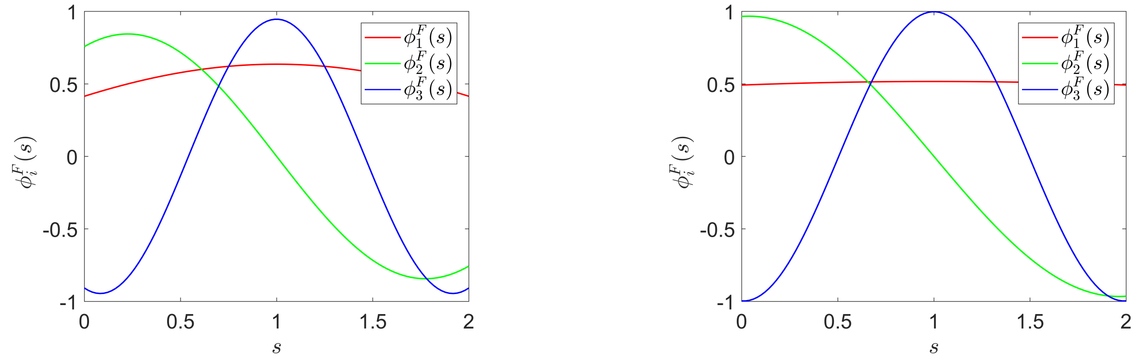

(a) Eigenfunctions for $d = 1$ **(b)** Eigenfunctions for $d = 10$

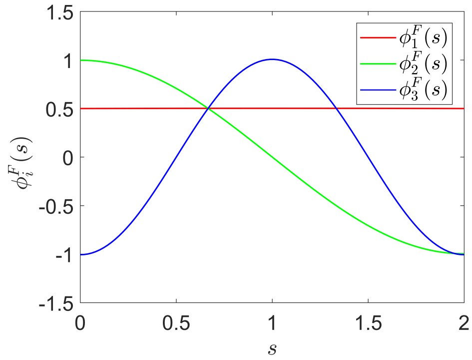

(c) Eigenfunctions for $d = 100$

Figure 17: The eigenfunctions for $d = 1$ (a), $d = 10$ (b) and $d = 100$ (c)

4.2.1 Multivariate random field

A multivariate random field consists of more than one random field. Let us consider a n-variate random field $\{F_j\}_{j=1}^n$, where $F_j : I_j \times \Omega \to \mathbb{R}$. The lengths of the interval I_j is denoted as l_j. For simplicity we consider that the intervals have equals lengths, i.e., $l = l_1 = l_2 = \ldots = l_n$. The interval I_j is given as $I_j = [(j-1)l, jl]$ The basic idea behind the multivariate case is to shift and align the univariate random fields such that they form an assembled univariate random field, see [23], as it is depicted in Fig. 20. The aligned random field is defined as

$$U(s,\theta) := \begin{cases} F_1(s,\theta) & s \in I_1, \\ \vdots & \\ F_n(s-(n-1)\cdot l,\theta) & s \in I_n. \end{cases} \tag{129}$$

The mean value if given as

$$\overline{U}(s) = \mathbb{E}(U(s,\theta)), \tag{130}$$

and its covariance function as

$$K_U(s,t) = \mathbb{E}\Big(\big(\overline{U}(s) - U(s,\theta)\big)\big(\overline{U}(t) - U(t,\theta)\big)\Big). \tag{131}$$

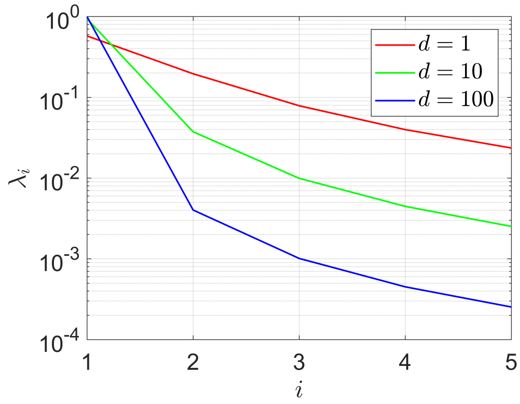

Figure 18: Eigenvalues for $d = 1, 10$ and 100

The aligned random field (129) admits the KLE

$$U(s,\theta) = \overline{U}(s) + \sum_{i=1}^{\infty} \sqrt{\lambda_i} \phi_i(s), Y_i(\theta). \tag{132}$$

where the eigenfunctions are defined as

$$\phi_i(s) = \begin{cases} \phi_i^{F_1}(s) & s \in I_1, \\ \vdots & \\ \phi_i^{F_n}(s-(n-1)\cdot l) & s \in I_n. \end{cases} \tag{133}$$

The eigenfunctions satisfy an orthonormality condition given as

$$\int_{I_1} \phi_i^{F_1}(s)\phi_j^{F_1}(s)\mathrm{d}s + \ldots + \int_{I_1} \phi_i^{F_n}(s)\phi_j^{F_n}(s)\mathrm{d}s = \delta_{ij}. \tag{134}$$

By analogy with the univariate random field the eigenvalues and eigenfunctions are obtained by solving the Fredholm integral equation,

$$\int_{I_\mathrm{t}} K_U(s,t)\phi_i(s)\mathrm{d}s = \lambda_i \phi_i(t), \tag{135}$$

where $I_\mathrm{t} = \bigcup_{j=1}^{n} I_j$. It can been shown that the Fredholm integral equation of the aligned random field can be written as

$$\int_{I_1} \begin{bmatrix} K_{F_1,F_1}(s,t) & \ldots & K_{F_1,F_n}(s,t) \\ \vdots & \ddots & \vdots \\ K_{F_n,F_1}(s,t) & \ldots & K_{F_n,F_n(s,t)} \end{bmatrix} \begin{bmatrix} \phi_i^{F_1}(s) \\ \vdots \\ \phi_i^{F_n}(s) \end{bmatrix} \mathrm{d}s = \lambda_i \begin{bmatrix} \phi_i^{F_1}(t) \\ \vdots \\ \phi_i^{F_3}(t) \end{bmatrix}. \tag{136}$$

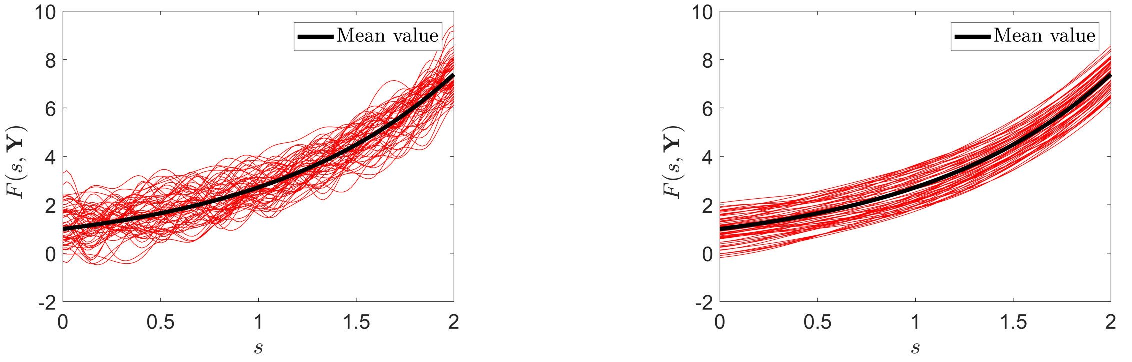

(a) Random realizations for $d = 1$ **(b)** Random realizations for $d = 10$

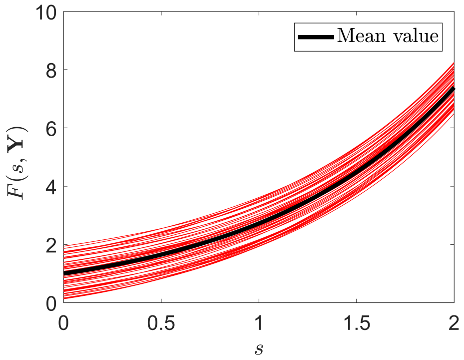

(c) Random realizations for $d = 100$

Figure 19: Sixty Random realization for $d = 1$ (a), $d = 10$ (b) and $d = 100$ (c)

The unknown eigenfunctions are approximated piecewise as

$$\phi_i(s) \approx \begin{cases} \displaystyle\sum_{k=1}^{N_{F_1}} \phi_{ik}^{F_1} N_k^{F_1}(s), & s \in I_1, \\ \vdots & \\ \displaystyle\sum_{k=1}^{N_{F_n}} \phi_{ik}^{F_n} N_k^{F_n}(s-(n-1)\cdot l) & s \in I_n. \end{cases} \tag{137}$$

By substituting the approximated eigenfunctions (137) into (136), multiplying with test function and integrating over the domain I_t, the following generalized eigenvalue problem is obtained

$$\begin{bmatrix} \boldsymbol{K}_{F_1,F_1} & \dots & \boldsymbol{K}_{F_1,F_n} \\ \vdots & \ddots & \vdots \\ \boldsymbol{K}_{F_n,F_1} & \dots & \boldsymbol{K}_{F_n,F_n} \end{bmatrix} \begin{bmatrix} \boldsymbol{\phi}_i^{F_1} \\ \vdots \\ \boldsymbol{\phi}_i^{F_n} \end{bmatrix} = \lambda_i \begin{bmatrix} \boldsymbol{M}_{F_1,F_1} & \dots & \mathbf{0} \\ \vdots & \ddots & \vdots \\ \mathbf{0} & \dots & \boldsymbol{M}_{F_n,F_n} \end{bmatrix} \begin{bmatrix} \boldsymbol{\phi}_i^{F_1} \\ \vdots \\ \boldsymbol{\phi}_i^{F_n} \end{bmatrix}, \tag{138}$$

which can be written in simplified manner as

$$\boldsymbol{K}\boldsymbol{\phi}_i = \lambda_i \boldsymbol{M}\boldsymbol{\phi}_i, \tag{139}$$

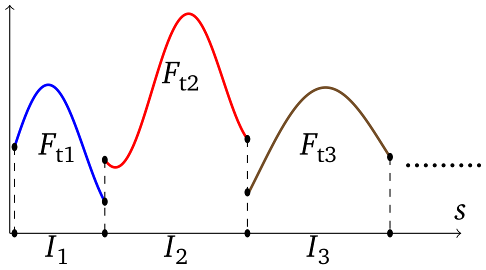

Figure 20: Aligned random fields

where $\boldsymbol{K}, \boldsymbol{M} \in \mathbb{R}^{\left(N_{F_1}+\ldots+N_{F_n}\right)\times\left(N_{F_1}+\ldots+N_{F_n}\right)}$ and $\boldsymbol{\phi}_i \in \mathbb{R}^{\left(N_{F_1}+\ldots+N_{F_n}\right)}$. The truncated KLE in this case reads

$$U_M(s,\boldsymbol{Y}) = \overline{U}(s) + \sum_{i=1}^{M} \sqrt{\lambda_i}\phi_i(s)Y_i(\theta). \tag{140}$$

The error due to the truncation is estimated by using (116).

4.3 Numerical example for trivariate random field

For the extended multivariate case we will illustrate a trivariate, i.e., $n = 3$, random field defined on the interval $I_t = I_1 \cup I_2 \cup I_3$ where $I_1 = [0,2)$, $I_2 = [2,4)$ and $I_3 = [4,6]$. The mean values of the individual random fields are given as $\overline{F}_1(s) = A_1 e^s$, $\overline{F}_2(s) = A_2 e^s$ and $\overline{F}_3(s) = A_3 e^s$ where $A_1 = 0.2$, $A_2 = 0.3$ and $A_3 = 0.5$. The covariances and cross-covariances are given as

$$\begin{aligned}
K_{F_1,F_1}(s,t) &= \sigma_{11} e^{-\frac{|s-t|}{d_{11}}}, \\
K_{F_1,F_2}(s,t) &= \sigma_{12} e^{-\frac{|s-t|}{d_{12}}}, \\
K_{F_1,F_3}(s,t) &= \sigma_{13} e^{-\frac{|s-t|}{d_{13}}}, \\
K_{F_2,F_2}(s,t) &= \sigma_{22} e^{-\frac{|s-t|}{d_{22}}}, \\
K_{F_2,F_3}(s,t) &= \sigma_{23} e^{-\frac{|s-t|}{d_{23}}}, \\
K_{F_3,F_3}(s,t) &= \sigma_{23} e^{-\frac{|s-t|}{d_{33}}},
\end{aligned} \tag{141}$$

where $\sigma_{11} = \sigma_{12} = \sigma_{13} = \sigma_{22} = \sigma_{23} = \sigma_{33} = 0.5$, and $d_{11} = 15$, $d_{12} = 5$, $d_5 = 50$, $d_{22} = 25$, $d_{23} = 5$, $d_{33} = 15$. The assembled correlation and mean value are depicted in Fig. 21a and Fig. 21b, respectively. The lining up method is implicitly applied. For $M = 4$ the trivariate random field field can be approximated up to a relative error of 0.94%. The eigenvalues and the eigenfunctions are shown in Fig. 23. The corresponding random realization of the trivariate random field for a uniform PDF are depicted in Fig. 22.

4.4 Spatial random field

When a certain function depends on spatial coordinates and moreover it is uncertain then it may be required to model it as a spatial random field. We shall denote the spatial random field as $F_s : D_s \times \Omega \rightarrow \mathbb{R}$, where D_s is a domain to be defined. The KLE of F_s is given as

$$F_s(\boldsymbol{x},\theta) = \overline{F}_s(\boldsymbol{x}) + \sum_{i=1}^{\infty} \sqrt{\lambda_i} f_i(\boldsymbol{x}) Y_i(\theta), \tag{142}$$

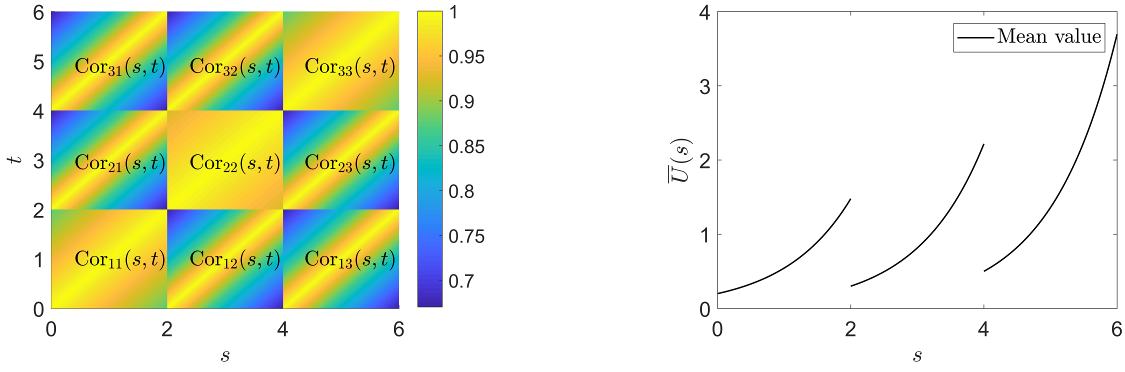

(a) Assembled correlation function

(b) Mean value

Figure 21: Assembled correlation function (a) and mean value (b) of the trivariate random field

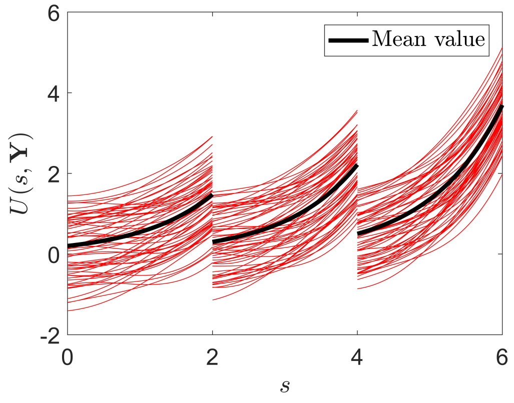

Figure 22: Realizations of the trivariate random field

where λ_i and $f_i(\cdot)$ are eigenvalues and eigenfunctions, respectively. They are obtained by solving the Fredholm integral equation

$$\int_{D_\mathrm{s}} K_\mathrm{s}(\boldsymbol{x},\boldsymbol{x}')f_i(\boldsymbol{x})\mathrm{d}x = \lambda_i f_i(\boldsymbol{x}'). \tag{143}$$

where $K_\mathrm{s}(\cdot,\cdot)$ is the covariance function of the spatial random field. The truncated KLE in this case reads

$$F_{\mathrm{s}M}(\boldsymbol{x},\boldsymbol{Y}) = \overline{F}_\mathrm{s}(\boldsymbol{x}) + \sum_{i=1}^{M} \sqrt{\lambda_i} f_i(\boldsymbol{x}) Y_i(\theta). \tag{144}$$

The error due to the truncation can be estimated by using (116). For the numerical solution of (143) we use the same triangular mesh used in the FEM. As already mentioned before the magnetic reluctivity is considered as constant within one triangular element. Hence, the unknown eigenfunctions can be approximated by a linear combination of a piecewise constant basis functions, see Fig. 24, as

$$f_i(\boldsymbol{x}) \approx \sum_{j=1}^{N_\mathrm{t}} f_{ij}\psi_j(\boldsymbol{x}). \tag{145}$$

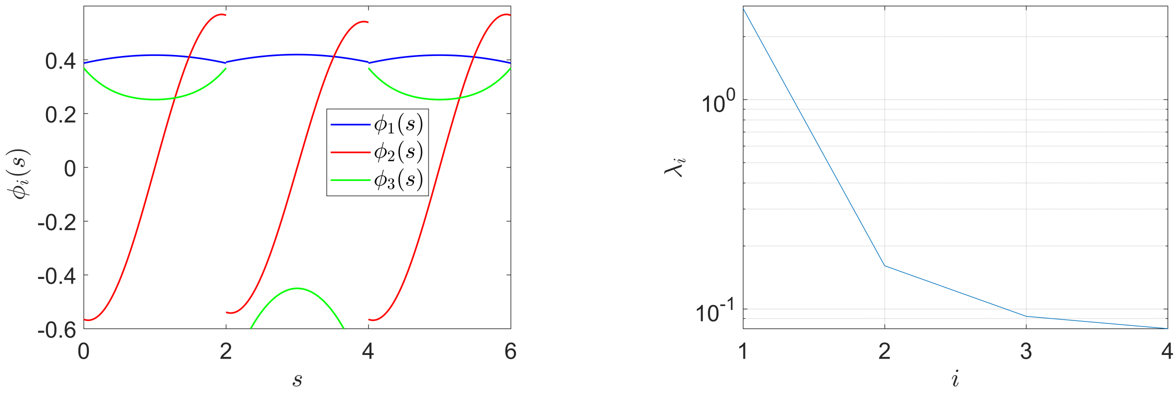

(a) The eigenfunctions of the aligned random field

(b) Eigenvalues

Figure 23: The first three eigenfunctions (a) and four eigenvalues (b) of the KLE

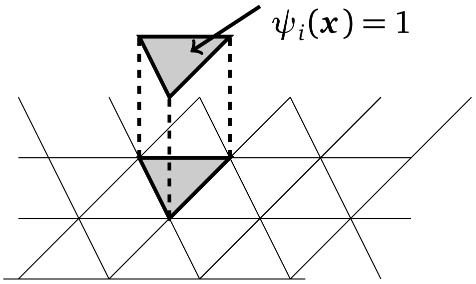

Figure 24: Piecewise constant basis function

By substituting (145) into (143) and applying the Galerkin method again a generalized eigenvalue problem is obtained

$$\boldsymbol{C}\boldsymbol{f}_i = \lambda_i \boldsymbol{V}\boldsymbol{f}_i, \tag{146}$$

where the elements of the matrices $\boldsymbol{C}$ and $\boldsymbol{V}$ are computed as

$$C_{ij} = \int_{D_s} K_s(\boldsymbol{x}, \boldsymbol{x}')\psi(\boldsymbol{x})\psi(\boldsymbol{x}')\mathrm{d}\boldsymbol{x}\,\mathrm{d}\boldsymbol{x}', \tag{147}$$

and

$$V_{ij} = \int_{D_s} \psi_i(\boldsymbol{x}')\psi_j(\boldsymbol{x}')\mathrm{d}\boldsymbol{x}', \tag{148}$$

respectively.

4.5 Numerical example

As an example we consider a random field with a mean value $\overline{F}_s = 300$ on a rectangular domain $D_s = [0, 1] \times [0, 1]$. The covariance function is given as

$$K_s(\boldsymbol{x}, \boldsymbol{x}') = \sigma e^{-\frac{||\boldsymbol{x}-\boldsymbol{x}'||_{l_1}}{d}}, \tag{149}$$

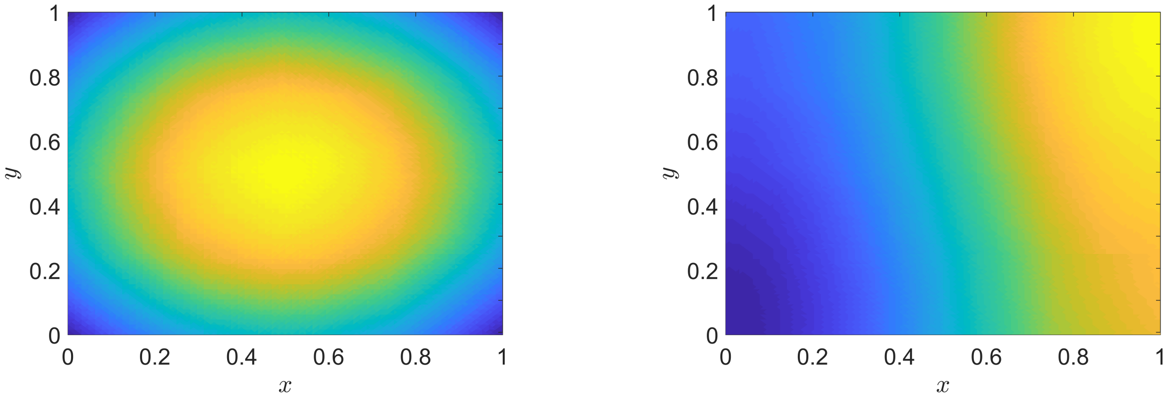

(a) First eigenfunction $f_1(\boldsymbol{x})$ **(b)** Second eigenfunction $f_2(\boldsymbol{x})$

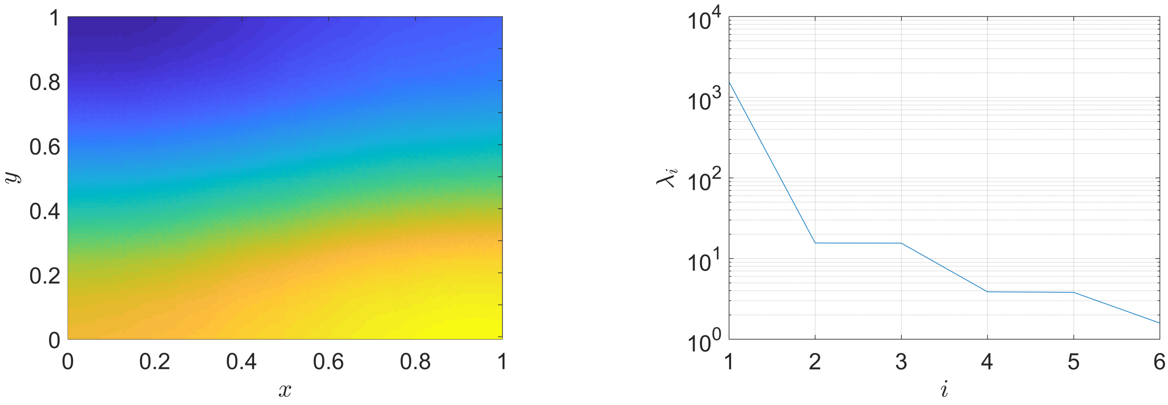

(c) Third eigenfunction $f_3(\boldsymbol{x})$ **(d)** Eigenvalues

Figure 25: Eigenfunctions (a-c) and eigenvalues (d)

where $\sigma = 40$, $d = 20$ and $||\boldsymbol{x} - \boldsymbol{x'}||_{l_1} = |x - x'| + |y - y'|$, where l_1 denotes the Manhattan norm. The number of triangles is $N_\mathrm{t} = 8321$. The random field is approximated by $M = 4$ random variables up to relative error $e_M = 1.1\%$. The first three eigenfunction and eigenvalues are shown in Fig. 25a-c and Fig. 25d, respectively.

4.6 Discussion of the eigenvalue problem

The matrices $\boldsymbol{A}$, $\boldsymbol{K}$ and $\boldsymbol{C}$ that arise in the generalized eigenvalue problems (121), (139) and (146) are dense. The number of triangles is significantly larger then the number of cubic spline basis functions for one dimensional discretization. Thus, only the generalized eigenvalue problem (146) is computationally challenging. First, the storage of $\boldsymbol{C}$ causes memory storage issues. Second, the arithmetical operation such as addition, matrix-vector and matrix-matrix multiplication are inefficient in terms of computation time. These arithmetical operations are part of the iterative algorithms for solving eigenvalue problems. We handle this issue by using hierarchical matrix format of the matrix $\boldsymbol{C}$. Details about this problem will be given in Chapter 6.

4.7 Uncertainty propagation

The uncertainty, which is modeled via the random vector $\boldsymbol{Y}$, propagates through the computational model and eventually affects the outputs. One of the methods for uncertainty propagation is the stochastic collocation (SC) method, see [52, 60, 61]. The basic idea is to construct a set of multivariate collocation points, execute the deterministic solver on each one of them and interpolate the solution by using global polynomials in order to approximate the dependency on $\boldsymbol{Y}$. These points are constructed for instance as a tensor products of one dimensional collocation points. The SC method is nonintrusive, i.e., one does not need to modify the deterministic solver.

4.7.1 Stochastic collocation method

The notation which will be used here is adopted from [10]. Let us for the sake of generality denote the QoI as Q. The approximation is given as follows

$$Q \approx \tilde{Q}(\boldsymbol{y}) = \sum_{m=1}^{N_c} Q(\boldsymbol{y}_m) L_m(\boldsymbol{y}), \tag{150}$$

where $\boldsymbol{y}_m$ and $L_m(\cdot)$ are multivariate collocation points and Lagrange polynomials, respectively. Let us have the multi-index $\boldsymbol{j} = [j_1, ..., j_M]$, such that the polynomial degrees p_n are given as a function of the indices j_n, i.e., $p_n = p(j_n)$. The detailed representation for (150) reads

$$\tilde{Q}(\boldsymbol{y}) = \sum_{i_1=0}^{\mathrm{p}(j_1)} \cdots \sum_{i_M=0}^{\mathrm{p}(j_M)} Q(y_1^{(i_1)}, ..., y_M^{(i_M)}) \prod_{n=1}^{M} l_{n,i_n}(y_n). \tag{151}$$

The collocation points are denoted as $\boldsymbol{y}^{(\boldsymbol{i})} = (y_1^{(i_1)}, y_2^{(i_2)}, ..., y_M^{(i_M)}) \in \mathrm{H}_{\boldsymbol{j},M}^{\mathrm{TP}}$, where $\mathrm{H}_{\boldsymbol{j},M}^{\mathrm{TP}} = \{y_1^{(0)}, ..., y_1^{(p(j_1))}\} \times ... \times \{y_M^{(0)}, ..., y_1^{(p(j_M))}\}$ is a tensor grid of collocation points. The univariate Lagrange polynomials are given as

$$l_{n,i_n}(y_n) := \prod_{k=0, k\neq i_n}^{\mathrm{p}(j_n)} \frac{y_n - y_n^{(k)}}{y_n^{(i_n)} - y_n^{(k)}}. \tag{152}$$

The mean value and its standard deviation of the QoI are denoted as μ_Q and σ_Q, respectively. They are approximated via numerical quadrature

$$\mu_Q \approx \tilde{\mu}_Q = \int_\Gamma \tilde{Q}(\boldsymbol{y}) \rho_Y(\boldsymbol{y}) \mathrm{d}\boldsymbol{y} = \sum_{i=1}^{N_c} w_i Q(\boldsymbol{y}_i), \tag{153}$$

and

$$\sigma_Q \approx \tilde{\sigma}_Q = \sqrt{\int_\Gamma \left(\tilde{Q}(\boldsymbol{y}) - \tilde{\mu}_Q\right)^2 \rho_Y(\boldsymbol{y}) \mathrm{d}\boldsymbol{y}} = \sqrt{\sum_{i=1}^{N_c} w_i \left(Q(\boldsymbol{y}_i) - \tilde{\mu}_Q\right)^2}, \tag{154}$$

where w_i is a multivariate weight coefficient obtained as

$$w_i = \prod_{n=1}^{M} w_{i_n}, \tag{155}$$

and w_{i_n} is a univariate weight coefficient computed as

$$w_{i_n} = \int_{\Gamma_n} l_{n,i_n}(y_n)\rho_{Y_n}(y_n)\mathrm{d}y_n. \tag{156}$$

If the isotropic case is considered, i.e., $\boldsymbol{j} = (l, ..., l)$, then the number of collocation points N_c is related to the degree of the Lagrange polynomial and the number of random variables as

$$N_c = (l+1)^M. \tag{157}$$

The "curse of dimensionality" follows from (157). The number of collocation points grow exponentially with the number of random variables. This issue has been treated, up to an extent with isotropic [5, 6, 62] and anisotropic sparse grids [63]. More recently, tensor decompositions of $Q(y_1^{(i_1)}, ..., y_M^{(i_M)})$, see [7, 8, 9, 10], have been employed. However, the development of computationally efficient uncertainty propagation is not in the focus of this thesis. Thus for our computations we will use tensor grids of collocation points for simplicity. One should keep in mind that if a weakly correlated random field is observed then one of the above mentioned remedies should be employed.

4.8 Conclusion

This chapter aimed to give brief introduction to the concept of random fields and explain how to propagate uncertainties from the input onto the output parameters. The univariate, trivariate and spatial random fields were covered. We gave a detailed explanation of the stochastic collocation method, for uncertainty propagation, which will further be used in the thesis.

5 Modeling Uncertainties in the Magnetic Behavior Law

In this chapter we will give a general description of the magnetic hysteresis phenomenon which will be followed by a brief description of its physics. We will introduce the Duhem hysteresis model as a phenomenological type of model and explain how uncertainties occurring in the hysteretic properties can be modeled by using the multivariate random field approach, see chapter 4.

5.1 General description of magnetic hysteresis

In Fig. 26a a simple ferromagnetic toroidal core is depicted. The core is surrounded with a conducting coil that consists of a large number of turns. There are certain assumptions behind this simple example in order to make the analysis easy. First, the field inside the core is considered as homogeneous, i.e., it does not depend on the spatial coordinates. Second, the lines of force that penetrate into the surrounding medium are neglected, i.e., it is considered that all of them are captured inside the core. Third, the magnetic field is considered to have only an azimuthal component, see Fig. 26a. Finally, the eddy currents are neglected. From the Ampère's law and these assumptions it follows that

$$H_{\phi}(t) = \frac{N_{\mathrm{j}} I(t)}{2\pi R}, \tag{158}$$

where N_{j} are number of turns and R is the radius of the toroidal core. We will not specify cylindrical coordinate system. We shall simply consider $H := H_{\phi}$ within the scope of this chapter. From (158) we can conclude that the magnetic field strength H is proportional to the electric current I and therefore both will have the same shape in time. From now on when we say that the material has been exposed to a magnetic field strength in our context this is achieved via a current excitation in (158). In this context we proceed by introducing the excitation $H(t)$ shown in Fig. 26b. The ferromagnetic material will respond by producing the magnetic flux density as depicted in Fig. 26c. When B is shown as function of H the typical hysteresis loop is obtained as it is illustrated in Fig. 26d. The following description can be given: when a piece of ferromagnetic material is exposed for the first time to a monotonically increasing $H(t)$, its relationship with $B(t)$ is expressed via the initial magnetization curve, see Fig. 26d. On the other hand, when the material is exposed to monotonically decreasing $H(t)$ the magnetic behavior law is given via the upper curve. During this phase two characteristic points can be recognized. The first one is the remanence point $(0, B_{\mathrm{r}})$ where even without external excitation there is a presence of a magnetic flux density. The second one is the coercive point $(-H_{\mathrm{c}}, 0)$. In this point one can see which value for the magnetic field strength is required such that the leftover magnetization vanishes. The procedure is repeated for monotonically increasing magnetic field and the bottom curve is obtained. In the next section a brief, not detailed, explanation is given about the origin of the magnetic behavior law from a physics point of view.

5.2 Origin of magnetism in materials

The magnetic behavior law establishes the relationship between the magnetic field strength vector $\boldsymbol{H}$ and the magnetic flux density vector $\boldsymbol{B}$. The induced magnetic flux density in vacuum is given as

$$\boldsymbol{B}_0 = \mu_0 \boldsymbol{H}, \tag{159}$$

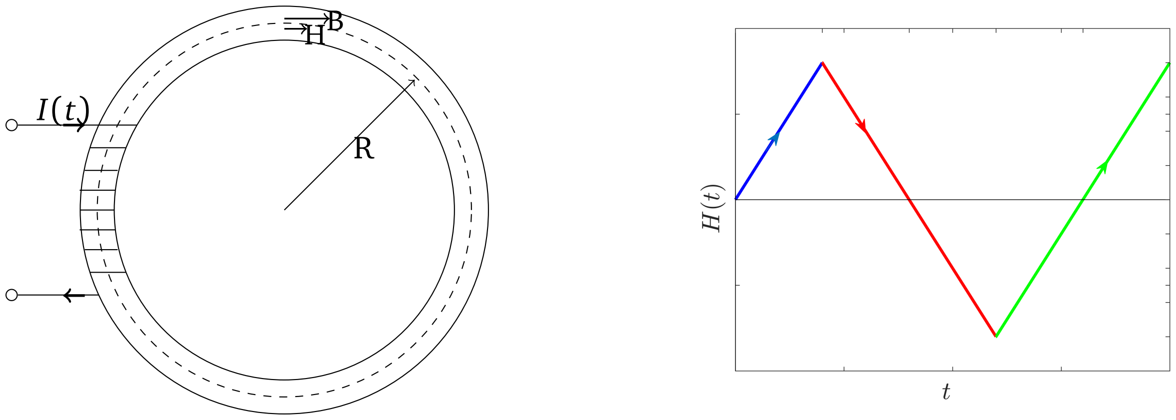

(a) Toroidal core **(b)** Magnetic field strength

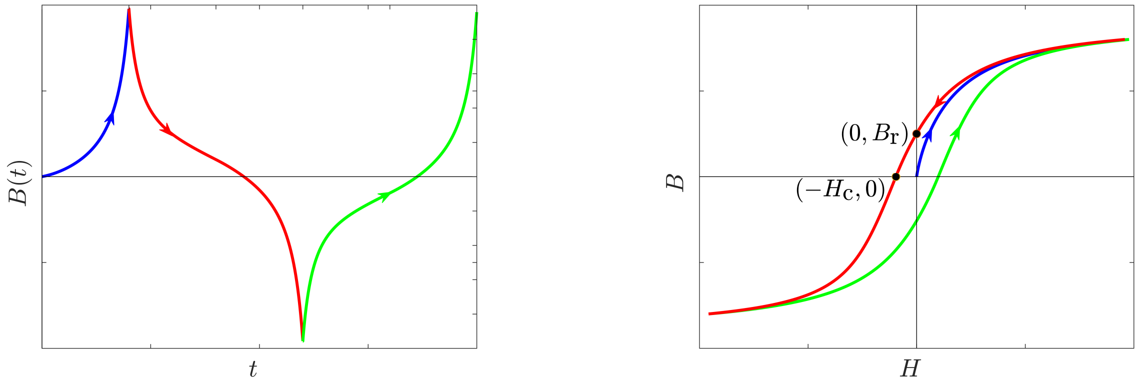

(c) Magnetic flux density **(d)** Hysteresis map

Figure 26: Toroidal core (a) excited with magnetic field strength (a) that produces a magnetic flux density (c) as a response and the hysteresis map (d)

where $\mu_0 = 4\pi \times 10^{-7}$ Hm^{-1} denotes its magnetic permeability. According to the macroscopic view on electromagnetism, the origin of magnetism in materials is the movement of the electrons around the atomic nucleus, Fig. 27.

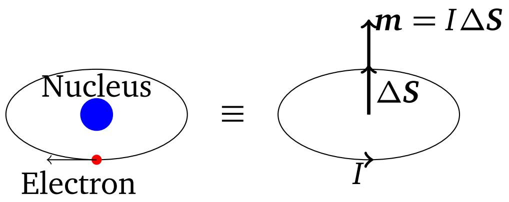

Figure 27: An atom viewed as an elementary magnetic dipole

The electron circling around the atomic nucleus can be viewed as a current in an elementary dipole. For the equations that follow we refer to [64] for details. The induced dipole moment is given as

$$\boldsymbol{m} = I\Delta \boldsymbol{S}, \tag{160}$$

where $\Delta\boldsymbol{S}$ is area of the circle. Any elementary volume ΔV of the magnetic material under consideration consists of a large number of magnetic dipoles whose induced moments are given as $\boldsymbol{m}_i$ and the density of the magnetic moments is given with the magnetization vector as

$$\boldsymbol{M} = \lim_{\Delta V \to 0} \frac{\sum_i \boldsymbol{m}_i}{\Delta V}. \tag{161}$$

When a magnetic dipole is exposed to the magnetic flux density induced by the vacuum a torque is generated, given as

$$\boldsymbol{\tau}_i = \boldsymbol{m}_i \times \boldsymbol{B}_0. \tag{162}$$

The torque tends to align the magnetic dipoles with the external field. The total magnetic flux density $\boldsymbol{B}$ is composed of the component induced by the vacuum $\mu_0\boldsymbol{H}$ and the contribution of the aligned magnetic dipoles $\mu_0\boldsymbol{M}$

$$\boldsymbol{B} = \mu_0(\boldsymbol{H} + \boldsymbol{M}). \tag{163}$$

If anisotropic material is considered then the relationship between $\boldsymbol{M}$ and $\boldsymbol{H}$ reads

$$\boldsymbol{M} = \overline{\chi}\boldsymbol{H}, \tag{164}$$

where $\overline{\chi}$ is the magnetic susceptibility tensor given as

$$\overline{\chi} := \begin{bmatrix} \chi_{\mathrm{xx}} & 0 & 0 \\ 0 & \chi_{\mathrm{yy}} & 0 \\ 0 & 0 & \chi_{\mathrm{zz}} \end{bmatrix}. \tag{165}$$

By substituting (164) in (163) the relation between $\boldsymbol{B}$ and $\boldsymbol{H}$ is established as,

$$\boldsymbol{B} = \mu_0(\overline{I} + \overline{\chi})\boldsymbol{H} = \mu_0\overline{\mu}_r\boldsymbol{H}, \tag{166}$$

where $\overline{I}$ is the unity matrix. The magnetic permeability tensor is given as,

$$\overline{\mu} = \mu_0\overline{\mu}_{\mathrm{r}}, \tag{167}$$

and $\overline{\mu}_r$ is the relative magnetic permeability tensor expressed as

$$\overline{\mu}_{\mathrm{r}} := \begin{bmatrix} \mu_{\mathrm{r,xx}} & 0 & 0 \\ 0 & \mu_{\mathrm{r,yy}} & 0 \\ 0 & 0 & \mu_{\mathrm{r,zz}} \end{bmatrix}. \tag{168}$$

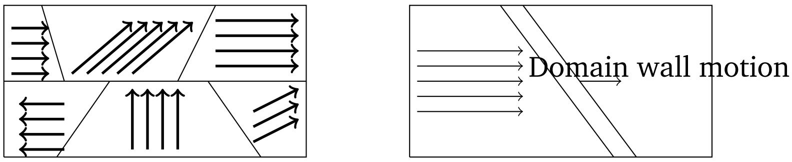

(a) Magnetic domains **(b)** Domain wall motion

Figure 28: Magnetic domains (a) and movement of the domain walls caused by external field (b)

5.2.1 Origin of magnetic hysteresis

Piere Weiss postulated, in 1907 in his paper [65], that ferromagnetic materials consist of small macroscopic regions known as magnetic domains, see Fig. 28a. The existence of the magnetic domains has been proven experimentally by Heinrich Barkhausen in 1919. The magnetic domains are separated by domain walls, where each magnetic domain is magnetized to saturation by the process known as "spontaneous magnetization", see [66, Chapter 1, page 12], which occurs below a temperature which is know as Curie temperature. In the absence of external magnetic fields the magnetic domains tend to be arbitrarily oriented, thus, leading to compensation of the overall magnetic effects. The domain walls of those magnetic domains whose magnetization vectors are positioned at the smallest angle with respect to the external field will be the first to orient and move in the direction of magnetization, hence, occupying the physical space of the neighboring domains. This physical process is known as domain wall motion, Fig. 28b. The domain wall motion is not an entirely reversible process. This means when the external magnetic field is removed some of the magnetic domains will still remain oriented. This is the physical explanation of hysteretic properties in ferromagnetic materials.

5.2.2 Modeling of magnetic hysteresis

There are mainly two categories of modeling approaches to model the behavior depicted in Fig. 26. There are physics and phenomenological based models. The physics type of models introduce discrete parameters which are closely related to the underlying process of magnetization. One instance of physics based model is the Jiles-Atherton model, see [67]. The phenomenological approach on the other hand describes the hysteresis phenomenon without necessarily providing insight, thus leading to simpler models that nonetheless capture the behavior. A review on the existing phenomenological-based models, such as the Ishlinskii, Duhem, Preisach can be found in [68].

5.3 Uncertainties in the magnetic hysteresis

As already stated in the introduction uncertainties in the magnetic behavior law occur due to manufacturing imperfections. One instance of these imperfections which is particularly important for our work has been reported in [20]. Namely in [20] the experimental data for twenty-eight samples hysteresis cycles has been given and a stochastic Jiles-Atherton model has been developed. We have implemented this model, see appendix A for details, in order to synthesize random data. Here the synthesized hysteresis cycles will serve as substitute of real experimental data. In Fig. 29 sixty random realizations of the stochastic Jiles-Atherton model are shown for illustration. The hysteresis cycles are generated in the interval $I = [-1.5, 1.5]$T.

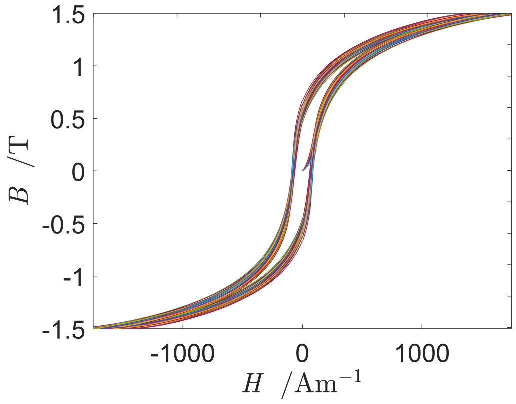

Figure 29: Sixty hysteresis cycles computed by the stochastic Jiles-Atherton model

5.4 Duhem hysteresis model

The Duhem magnetic hysteresis model falls into the category of phenomenological models. It is based on the assumption that the output changes its direction only when the input does. The model has been introduced for the first time in [69]. The governing ordinary differential equation (ODE) of the model reads

$$\frac{\mathrm{d}H}{\mathrm{d}B} = \alpha_c \cdot \mathrm{sgn}(\dot{B})(f(B) - H) + g(B) \quad B \in \mathbb{R}, \tag{169}$$

where

$$\mathrm{sgn}(\dot{B}) = \begin{cases} 1 & \dot{B} > 0, \\ -1 & \dot{B} < 0. \end{cases} \tag{170}$$

This particular version is known as the inverse Duhem model, i.e., the roles of H and B are interchanged. The right hand side of (169) is fully characterized by two material functions $f : \mathbb{R} \to \mathbb{R}$, $g : \mathbb{R} \to \mathbb{R}$ and one scalar parameter α_c. The domain in which these functions are defined theoretically is the set of real numbers $\mathbb{R}$. However, in practice measurement data usually exist on symmetric interval $I = [-B_{\max}, B_{\max}]$. We perceive the scalar paramter α_c as a constant material function on the interval I and we denote it as $\alpha : \mathbb{R} \to \mathbb{R}$. From this point we shall say that the Duhem hysteresis model is fully characterized with three material functions. The assumptions and the restrictions that the physics of ferromagnetic hysteresis imposes on these material functions are discussed in details in [22, 70, 71]. These assumptions and restrictions are important in our work and therefore we provide a brief discussion on them. The three material function of the Duhem magnetic hystereis model are assumed to satisfy

Assumption 1 $f(\cdot)$ is piecewise smooth, monotone increasing, odd, with $\lim_{B->\infty} f'(B) < \infty$.

Assumption 2 $g(\cdot)$ is piecewise continuous, even, with $\lim_{B->\infty} g(B) = \lim_{B->\infty} f'(B) < \infty$.

Assumption 3 $\alpha(B) > 0 \quad \forall B \in I$.

The physics of ferromagnetic hysteresis imposes the following assumptions

Assumption 4 $g(B) > f'(B) \quad \forall B \in I$.

Assumption 5 $g(B) \geq \alpha_c e^{\alpha_c} \int_B^\infty (g(z) - f'(z)) e^{-\alpha_c z} \mathrm{d}z \quad \forall B \in I.$

Assumption 4 has two implications. The first one is that all of the possible hysteresis paths will remain encapsulated by the so called major loop. The Major loop is a theoretical hysteresis cycle that would be obtained if the upper and bottom curve are computed starting from $(H_0, B_o) = (\pm\infty, \pm\infty)$. The second one is that the energy dissipated in all primitive loops will remain always positive. Assumption 5 is necessary and sufficient to ensure positive monotone responses, i.e., $\frac{\mathrm{d}H}{\mathrm{d}B} > 0$ [22]. The analytical solution of (169) is given as

$$H = f(B) + (H_0 - f(B_0)) e^{-\alpha_c (B - B_0) \mathrm{sgn}(\dot{B})} + e^{-\alpha_c B \mathrm{sgn}(\dot{B})} \int_{B_0}^{B} (g(z) - f'(z)) e^{\alpha_c z \mathrm{sgn}(\dot{B})} \mathrm{d}z. \quad (171)$$

The initial magnetization curve can be obtained from the analytical form by using $(H_0, B_0) = (0, 0)$ and $\mathrm{sgn}(\dot{B}) = 1$ which results in the following expression

$$H_\mathrm{i} = f(B) + e^{-\alpha_c B} \int_{B_0}^{B} (g(z) - f'(z)) e^{\alpha_c z} \mathrm{d}z. \quad (172)$$

Starting from any initial condition (H_0, B_0) one can distinguish between an ascending and descending magnetization curve. For $\mathrm{sgn}(\dot{B}) = \pm 1$ the expression for the ascending and descending portion of the curve reads

$$H_\mathrm{a} = f(B) + (H_0 - f(B_0)) e^{\alpha_c (B - B_0)} + e^{\alpha_c B} \int_{B_0}^{B} (g(z) - f'(z)) e^{-\alpha_c z} \mathrm{d}z, \quad (173)$$

and

$$H_\mathrm{d} = f(B) + (H_0 - f(B_0)) e^{-\alpha_c (B - B_0)} + e^{-\alpha_c B} \int_{B_0}^{B} (g(z) - f'(z)) e^{\alpha_c z} \mathrm{d}z, \quad (174)$$

respectively. In [22] a particular form of $f(\cdot)$ and $g(\cdot)$ has been proposed which is given as

$$f(B) = \begin{cases} A_1 \tan(A_2 B) & |B| < B_\mathrm{cl}, \\ A_1 \tan(A_2 B_\mathrm{cl}) + \dfrac{B - B_\mathrm{cl}}{\mu_\mathrm{cl}} & B > B_\mathrm{cl}, \\ -A_1 \tan(A_2 B_\mathrm{cl}) + \dfrac{B + B_\mathrm{cl}}{\mu_\mathrm{cl}}, & B < -B_\mathrm{cl}, \end{cases} \quad (175)$$

and

$$g(B) = \begin{cases} f'(B)(1 - A_3 \exp(\dfrac{A_4 |B|}{B - |B|})) & |B| < B_\mathrm{cl}, \\ f'(B) & |B| > B_\mathrm{cl}, \end{cases} \quad (176)$$

respectively, where B_cl is the magnetic flux density at which saturation of the material occurs and the magnetic permeability at that point is denotes as μ_cl. The coefficients A_1,A_2,A_3 and A_4 together with B_cl and μ_cl are determined from experimental data. For illustration purposes we compute one typical hysteresis cycle for a triangular excitation of the magnetic flux density

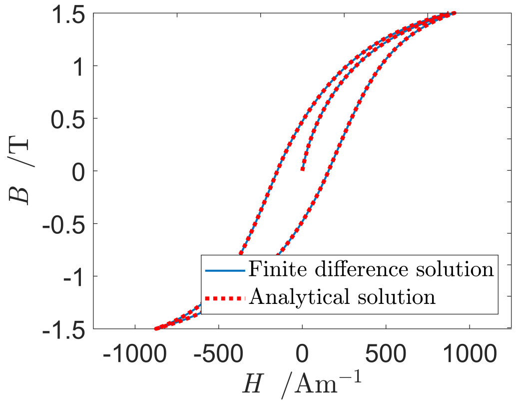

Figure 30: Comparison between finite difference and analytical solution of the Duhem ODE with $f(\cdot)$ and $g(\cdot)$ defined as in (175) and (176) for $A_1 = 500, A_2 = 0.77, A_3 = 0.71, A_4 = 1$ and $B_{\mathrm{cl}} = 2.5$.

in the interval $[-1.5, 1.5]$T. We use the typical form of the material functions given with (175) and (176) for $A_1 = 500$, $A_2 = 0.77$, $A_3 = 0.71$, $A_4 = 1$ and $B_{\mathrm{cl}} = 2.5$. and the analytical solution. The governing ODE is solved by using the explicit Euler method, i.e., we discretize (169) as

$$\frac{H_{i+1} - H_i}{\Delta B_i} = \alpha \cdot \mathrm{sgn}(\Delta B_i)(f(B_i) - H_i) + g(B_i), \tag{177}$$

where $\Delta B_i = 1.5 \cdot 10^{-6}$ and the comparison with the analytical solution is depicted in Fig. 30.

5.5 Identification of the Duhem model

In order to be as general as possible we propose to approximate the unknown material functions by using a finite number of cubic B-spline basis functions, see appendix C denoted as N_k^f and $N_k^g \in \mathscr{L}_N^{3,0}$ for the f and g function, respectively.

$$f(B) \approx \sum_{k=1}^{N_f} f_k N_k^f(B), \tag{178}$$

$$g(B) \approx \sum_{k=1}^{N_g} g_k N_k^g(B). \tag{179}$$

For our further analysis we rely on identifying the material functions based on given experimental data. By substituting (178) into the analytical solution (171) the following function can be defined

$$H = F(B, \boldsymbol{p}) = \sum_{k=1}^{N_f} f_k N_k^f(B) + (H_0 - \sum_{k=1}^{N_f} f_k N_k^f(B_0)) e^{-\alpha_c (B - B_0)\mathrm{sgn}(\dot{B})} \tag{180}$$
$$+ e^{-\alpha_c B \cdot \mathrm{sgn}(\dot{B})} \int_{B_0}^{B} \left(\sum_{k=1}^{N_g} g_k N_k^g(z) - \sum_{k=1}^{N_f} f_k \frac{\partial N_k^f(z)}{\partial z} \right) e^{\alpha_c z \mathrm{sgn}(\dot{B})} \mathrm{d}z,$$

where $\boldsymbol{p}$ is the vector of unknown coefficients expressed as

$$\boldsymbol{p} := (f_1, ..., f_{N_f}, \alpha_c, g_1, ..., g_{N_g}). \tag{181}$$

Up to this point the problem of identifying the material functions boils down to estimating the vector $\boldsymbol{p}$ based on the available set of experimental data $\{(H_j^e, B_j^e)\}_{j=1}^{N_\mathrm{p}}$. The properties of the material functions can be satisfied by enforcing certain conditions on the unknown coefficients. We use an odd number of functions such that we can allocate the middle coefficients $f_{(N_f+1)/2}$ and $g_{(N_g+1)/2}$, respectively. The oddness and the evenness of $f(\cdot)$ and $g(\cdot)$ is enforced through antisymmetry and symmetry of the coefficients w.r.t the middle coefficients, respectively. The function $f(\cdot)$ satisfies $f(0) = 0$ and as a consequence $f_{(N_f+1)/2} = 0$. The value of $g_{(N_g+1)/2}$ is related to the derivative of the initial magnetization curve at $B = 0$. Namely,

$$\left.\frac{\mathrm{d}H_\mathrm{i}}{\mathrm{d}B}\right|_{B=0} = g(0). \tag{182}$$

In practice the initial slope of the initial magnetization curve is computed as

$$\left.\frac{\mathrm{d}H_\mathrm{i}}{\mathrm{d}B}\right|_{B=0} \approx \frac{H_2^e - H_1^e}{B_2^e - B_1^e}. \tag{183}$$

The oddness and the evenness of the coefficients $\{f_i\}_{i=1}^{N_f}$ and $\{g_i\}_{i=1}^{N_g}$ is expressed as

$$f_i = -f_{N_f-i-1} \quad \text{where} \quad i \in \{1, ..., \frac{N_f - 1}{2}\}, \tag{184}$$

$$g_i = g_{N_g-i-1} \quad \text{where} \quad i \in \{1, ..., \frac{N_g - 1}{2}\}, \tag{185}$$

which results in the following linear system

$$\boldsymbol{A}_\mathrm{eq}\boldsymbol{p} = \boldsymbol{b}_\mathrm{eq}, \tag{186}$$

where $\boldsymbol{A}_\mathrm{eq} \in \mathbb{R}^{(\frac{N_f+N_g}{2}-1)\times(N_f+N_g+1)}$ and $\boldsymbol{b}_\mathrm{eq} \in \mathbb{R}^{(\frac{N_f+N_g}{2}+1)}$. The monotonicity and positivity condition can be enforced via the inequalities

$$f_i - f_{i+1} < 0 \quad \text{where} \quad i \in \{1, ..., N_f - 1\}, \tag{187}$$

and

$$-\alpha_\mathrm{c} < 0, \tag{188}$$

respectively. From these two inequalities the following matrix inequality is obtained

$$\boldsymbol{A}_\mathrm{ieq}\boldsymbol{p} < \boldsymbol{b}_\mathrm{ieq}. \tag{189}$$

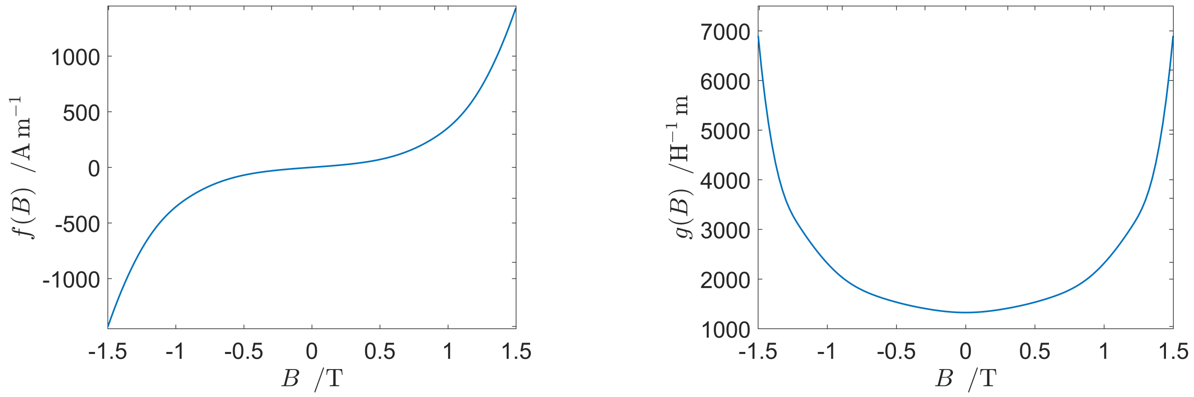

(a) Identified $f(\cdot)$ function **(b)** Identified $g(\cdot)$ function

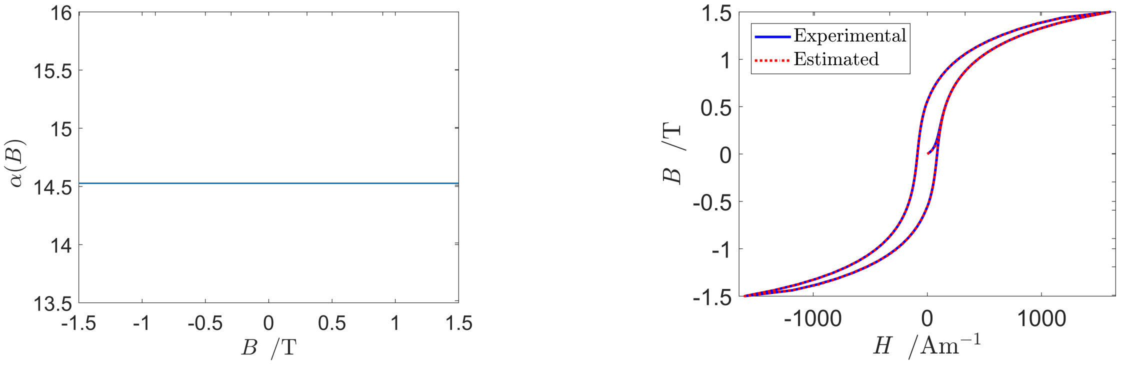

(c) Identified $\alpha(\cdot)$ function **(d)** Comparison

Figure 31: Identified material function (a-c) and comparison between the Duhem and Jiles-Atherton model (d) for $M_s = 1.71787652 \cdot 10^6$, $k_1 = 189$, $k_0 = 247.11$, $\sigma = 0.99$, $c = 0.54$, $a = 1203$ and $\alpha = 0.002$ in $N_p = 255$

where $\boldsymbol{A}_{\text{ieq}} \in \mathbb{R}^{N_f \times (N_f + N_g + 1)}$ and $\boldsymbol{b}_{\text{ieq}} \in \mathbb{R}^{N_f}$. We proceed by defining the mean square error as follows

$$e(\boldsymbol{p}) := \sum_{j=1}^{N_p} (H_j^e - F(B_j^e, \boldsymbol{p}))^2. \tag{190}$$

By having introduced the error function and how to incorporate certain properties of the material functions we are in position to formulate the following nonlinear constrained minimization problem

$$\begin{aligned} \underset{\boldsymbol{p}}{\text{minimize}} \quad & e(\boldsymbol{p}) \\ \text{subject to} \quad & \boldsymbol{A}_{\text{ieq}} \boldsymbol{p} \leq \boldsymbol{b}_{\text{ieq}}, \\ & \boldsymbol{A}_{\text{eq}} \boldsymbol{p} = \boldsymbol{b}_{\text{eq}}. \end{aligned} \tag{191}$$

We use the sequential quadratic programming (SQP) algorithm to solve (191), see [72]. The quality of the identification is quantified through the coefficient of efficiency as

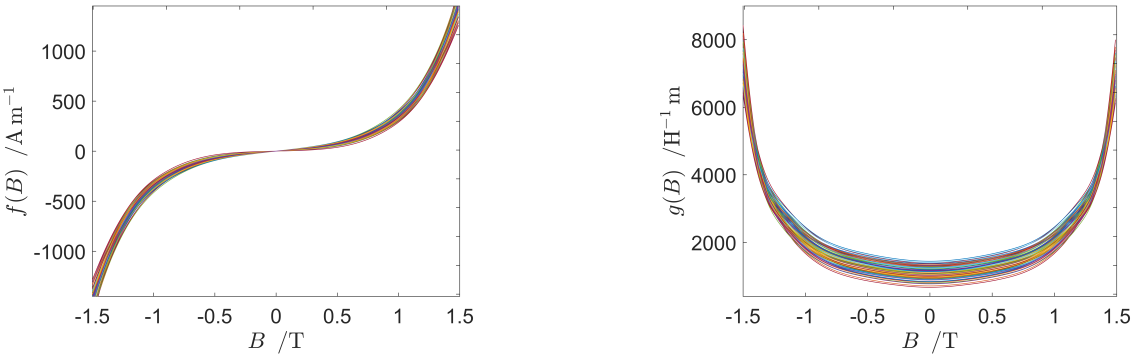

(a) Samples of the $f(\cdot,\theta)$ function **(b)** Samples of the $g(\cdot,\theta)$ function

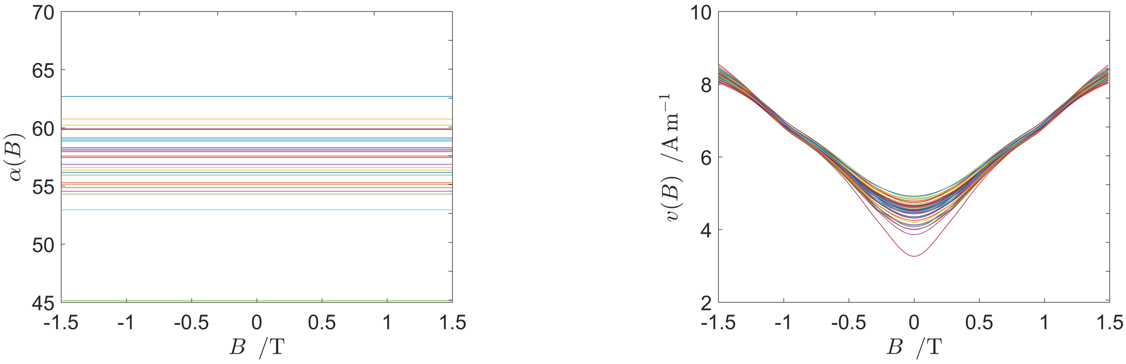

(c) Samples of the $\alpha(\cdot,\theta)$ function **(d)** Samples of transformed $v(\cdot,\theta)$ function

Figure 32: Estimated material functions from the synthesized data (a-c) and transformed material function (d)

$$R^2 = 1 - \frac{\sum_{j=1}^{N_p}(H_j^e - F(B_j^e, p^*))^2}{\sum_{j=1}^{N_p}(H_j^e - \overline{H}^e)^2}, \tag{192}$$

where p^* is the solution of the optimization problem and $\overline{H}^e$ is the mean value of the magnetic field strength over the experimental points. We are going to use a modified version of (192), see [20], which is given as

$$R_\mathrm{a}^2 = 1 - (1 - R^2)\frac{N_p - 1}{N_p - q - 1}, \tag{193}$$

where q is the number of unknown parameters. In our case $q = N_f + N_g + 1$. For illustration purposes we generate data by using the Jiles-Athrton model with the following values of the parameters: $M_s = 1.71787652 \cdot 10^6$, $k_1 = 189$, $k_0 = 247.11$, $\sigma = 0.99$, $c = 0.54$, $a = 1203$ and $\alpha = 0.002$ in $N_p = 255$ points. Then by applying the identification procedure the corresponding material functions are obtained as it is depicted in Fig. 31(a-c). The comparison between the synthesized data and the one generated with the identified model is shown in Fig. 31d. The fitting quality is $R_\mathrm{a} = 0.9999987$.

In order to incorporate the uncertain behavior of the hysteresis cycles depicted in Fig. 29 we propose to replace the three material functions $f(\cdot)$, $g(\cdot)$ and $\alpha(\cdot)$ with three random fields $f(\cdot,\cdot)$, $g(\cdot,\cdot)$ and $\alpha(\cdot,\cdot)$ defined as

$$f : I \times \Omega \to \mathbb{R}, \tag{194}$$

$$g : I \times \Omega \to \mathbb{R}, \tag{195}$$

$$\alpha : I \times \Omega \to \mathbb{R}. \tag{196}$$

Moreover we propose to align these random fields in order to obtain a univariate representation as

$$U_0(s,\theta) = \begin{cases} f(s,\theta) & s \in I_1 \\ g(s-2B_{\max},\theta) & s \in I_2 \\ \alpha(s-4B_{\max},\theta) & s \in I_3 \end{cases} \tag{197}$$

where $I_1 = I$, $I_2 = (B_{\max}, 3B_{\max})$ and $I_3 = (3B_{\max}, 5B_{\max}]$. The idea is that the uncertainty arises first in the material functions and then propagates through the ODE (169) and results in the behavior that we observe in Fig. 29. In a stochastic setting the random fields $f(\cdot,\cdot)$, $g(\cdot,\cdot)$ and $\alpha(\cdot,\cdot)$ are assumed to satisfy almost surely the following assumptions

Assumption 6 $f(\cdot,\theta)$ is piecewise smooth, monotone increasing, odd, with $\lim_{B->\infty} f'(B,\theta) < \infty \ \forall \theta \in \Omega$.

Assumption 7 $g(\cdot,\theta)$ is piecewise continuous, even, with $\lim_{B->\infty} g(B,\theta) = \lim_{B->\infty} f'(B,\theta) < \infty \quad \forall \theta \in \Omega$.

Assumption 8 $\alpha(B,\theta) > 0 \ \ \forall (B,\theta) \in I \times \Omega$.

The physics of ferromagnetic hysteresis imposes the following assumptions

Assumption 9 $g(B,\theta) > f'(B,\theta) \ \ \forall (B,\theta) \in I \times \Omega$.

Assumption 10 $g(B,\theta) \geq \alpha_c e^{\alpha_c} \int_B^\infty (g(z,\theta) - f'(z,\theta)) e^{-\alpha_c z} \mathrm{d}z \ \ \forall (B,\theta) \in I \times \Omega$.

In chapter 4 we explained that the KLE is truncated after some terms in order to obtain a finite dimensional representation of the random field. After truncation it is important that each random realization of the random field, i.e., the material functions still fulfill the assumptions 6-10. In order to guarantee monotonicity of $f(\cdot,\theta)$ we introduce the following transformation

$$v(s,\theta) := \ln\left(\frac{\partial f(s,\theta)}{\partial s}\right). \tag{198}$$

By using (198) $f(\cdot,\cdot)$ is expressed as

$$f(s,\theta) = \int_0^s e^{v(s,\theta)} \mathrm{d}z + C, \tag{199}$$

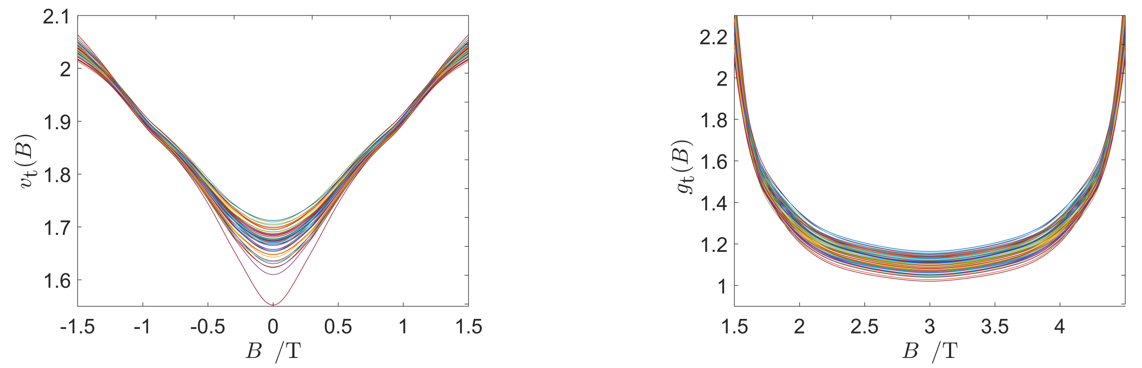

(a) Samples of the $v_{\mathrm{t}}(\cdot,\theta)$ function

(b) Samples of the $g_{\mathrm{t}}(\cdot,\theta)$ function

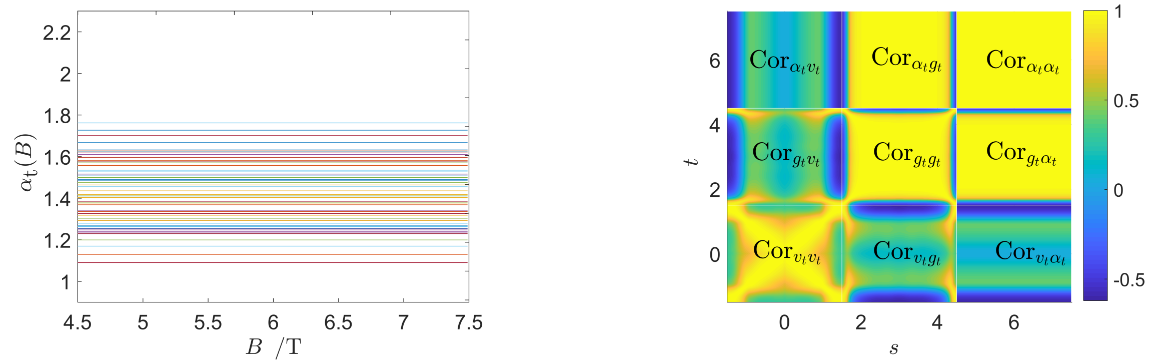

(c) Samples of the $\alpha_{\mathrm{t}}(\cdot,\theta)$ function

(d) Assembled correlation function

Figure 33: Transformed estimated material functions from the experimental cycles (a-c) and assembled correlation function (d)

where the constant C is determined from the initial condition $f(0,\theta)=0 \Rightarrow C=0$. We will consider $v(\cdot,\cdot)$ as part of the aligned random field and obtain $f(\cdot,\theta)$ by using (199) which guarantees monotonicity. This approach is known in the literature as monotonic regression, see [73]. The satisfaction of other properties will be addressed after we introduce the KLE of the trivariate random field and the modeling approach related to the random variables. In order to compensate for the different scales we propose to rescale the data. The aligned rescaled random field that also incorporates the transformation (198) reads

$$U(s,\theta) := \begin{cases} v_{\mathrm{t}}(s,\theta) = A_{\mathrm{v}}(v(s,\theta) - C_{\mathrm{v}}) + D_{\mathrm{v}} & s \in I_1, \\ g_{\mathrm{t}}(s,\theta) = A_{\mathrm{g}}(g(s-2B_{\max},\theta) - C_{\mathrm{g}}) + D_{\mathrm{g}} & s \in I_2, \\ \alpha_{\mathrm{t}}(s,\theta) = A_{\alpha}(\alpha(s-4B_{\max},\theta) - C_{\alpha}) + D_{\alpha} & s \in I_3. \end{cases} \tag{200}$$

The rescaling is achieved by the coefficients $A_{\mathrm{v}}, A_{\mathrm{g}}, A_{\alpha}, C_{\mathrm{v}}, C_{\mathrm{g}}, C_{\alpha}, D_{\mathrm{v}}, D_{\mathrm{g}}, D_{\alpha}$. They are computed based on the desired range $[n_{\min}, n_{\max}]$ and the currently observed ranges in the material curves $[c^v_{\min}, c^v_{\max}]$, $[c^g_{\min}, c^g_{\max}]$ and $[c^{\alpha}_{\min}, c^{\alpha}_{\max}]$. The currently observed range of values is computed based on the curve that bounds all other random realizations of the random field from below. For example, the rescaled v_{t} random field is given as

$$v_{\mathrm{t}}(s,\theta) = (v(s,\theta) - c_{\min}) \frac{(n_{\max} - n_{\min})}{(c_{\max} - c_{\min})} + n_{\min}, \tag{201}$$

from where we can see that $A_{\mathrm{v}} = \frac{(n_{\max}-n_{\min})}{(c_{\max}-c_{\min})}$, $C_{\mathrm{v}} = c^{v}_{\min}$ and $D_{\mathrm{v}} = n_{\min}$. The same reasoning applies to the other coefficients. We proceed with by constructing the corresponding KLE of the trivariate random field given as a special case of (132) for choosing $n = 3$. The eigenvalues and eigenfunction are obtained by solving the Fredholm integral equation

$$\int_{I_t} K_U(s,t)\phi_i(t)\mathrm{d}t = \lambda_i \phi_i(s). \tag{202}$$

The system matrix (202) can be decomposed

$$\int_I \begin{bmatrix} \mathrm{K}_{v_\mathrm{t} v_\mathrm{t}}(s,t) & \mathrm{K}_{v_\mathrm{t} g_\mathrm{t}}(s,t) & \mathrm{K}_{v_\mathrm{t} \alpha_\mathrm{t}}(s,t) \\ \mathrm{K}_{g_\mathrm{t} v_\mathrm{t}}(s,t) & \mathrm{K}_{g_\mathrm{t} g_\mathrm{t}}(s,t) & \mathrm{K}_{g_\mathrm{t} \alpha_\mathrm{t}}(s,t) \\ \mathrm{K}_{\alpha_\mathrm{t} v_\mathrm{t}}(s,t) & \mathrm{K}_{\alpha_\mathrm{t} g_\mathrm{t}}(s,t) & \mathrm{K}_{\alpha_\mathrm{t} \alpha_\mathrm{t}}(s,t) \end{bmatrix} \begin{bmatrix} \phi_{v_\mathrm{t},i}(t) \\ \phi_{g_\mathrm{t},i}(t) \\ \phi_{\alpha_\mathrm{t},i}(t) \end{bmatrix} \mathrm{d}t = \lambda_i \begin{bmatrix} \phi_{v_\mathrm{t},i}(s) \\ \phi_{g_\mathrm{t},i}(s) \\ \phi_{\alpha_\mathrm{t},i}(s) \end{bmatrix}. \tag{203}$$

There is one crucial difference between the approximation of the eigenfunctions given by (137) and the one related to the trivariate case here. Namely, there is no necessity to approximate the $\phi_{\alpha_{\mathrm{t},i}}$ with B-splines basis functions since it gives a KLE representation of constant function $\alpha(\cdot,\theta)$. It is naturally to approximate it with constant eigenfunctions within the interval I_3. Therefore, the eigenfunctions are approximated as

$$\phi_i(s) \approx \begin{cases} \displaystyle\sum_{m=1}^{N_{v_\mathrm{t}}} \phi^{v_\mathrm{t}}_{im} N^{v_\mathrm{t}}_m(s) & s \in I_1 \\ \displaystyle\sum_{m=1}^{N_{g\mathrm{t}}} \phi^{g_\mathrm{t}}_{im} N^{g_\mathrm{t}}_m(s - 2B_{\max}) & s \in I_2, \\ \phi^{\alpha_\mathrm{t}}_i & s \in I_3. \end{cases} \tag{204}$$

By substituting the approximated eigenfunctions, (204), into the Fredholm integral equation (203), and multiplying it with test function and integrating over the computational domain, we obtain the generalized eigenvalue problem

$$\begin{bmatrix} \boldsymbol{K}_{v_\mathrm{t} v_\mathrm{t}} & \boldsymbol{K}_{v_\mathrm{t} g_\mathrm{t}} & \boldsymbol{K}_{v_\mathrm{t} \alpha_\mathrm{t}} \\ \boldsymbol{K}_{g_\mathrm{t} v_\mathrm{t}} & \boldsymbol{K}_{g_\mathrm{t} g_\mathrm{t}} & \boldsymbol{K}_{g_\mathrm{t} \alpha_\mathrm{t}} \\ \boldsymbol{K}_{\alpha_\mathrm{t} v_\mathrm{t}} & \boldsymbol{K}_{\alpha_\mathrm{t} g_\mathrm{t}} & \boldsymbol{K}_{\alpha_\mathrm{t} \alpha_\mathrm{t}} \end{bmatrix} \begin{bmatrix} \boldsymbol{\phi}^{v_\mathrm{t}}_i \\ \boldsymbol{\phi}^{g_\mathrm{t}}_i \\ \boldsymbol{\phi}^{\alpha_\mathrm{t}}_i \end{bmatrix} = \lambda_i \begin{bmatrix} \boldsymbol{M}_{v_\mathrm{t} v_\mathrm{t}} & \boldsymbol{0} & \boldsymbol{0} \\ \boldsymbol{0} & \boldsymbol{M}_{g_\mathrm{t} g_\mathrm{t}} & \boldsymbol{0} \\ \boldsymbol{0} & \boldsymbol{0} & \boldsymbol{M}_{\alpha_\mathrm{t} \alpha_\mathrm{t}} \end{bmatrix} \begin{bmatrix} \boldsymbol{\phi}^{v_\mathrm{t}}_i \\ \boldsymbol{\phi}^{g_\mathrm{t}}_i \\ \boldsymbol{\phi}^{\alpha_\mathrm{t}}_i, \end{bmatrix} \tag{205}$$

or written in simplified manner,

$$\boldsymbol{K}\boldsymbol{\phi}_i = \lambda_i \boldsymbol{M}\boldsymbol{\phi}_i, \tag{206}$$

with $\boldsymbol{K}, \boldsymbol{M} \in \mathbb{R}^{(N_{v_\mathrm{t}}+N_{g_\mathrm{t}}+1)\times(N_{v_\mathrm{t}}+N_{g_\mathrm{t}}+1)}$.

We use the synthesized data to identify the corresponding material functions, see Fig. 32. We conducted the identification procedure for $N_f = N_g = 13$ cubic spline basis functions. This number is chosen by experimentation, i.e., by taking different numbers we observe which one yields better accuracy. In chapter 4 in Fig. 19 we showed random realizations of weakly and strongly correlated material functions. By observing the identified material data in Fig. 32a and Fig. 32b one can say intuitively that a strong correlation is present. A maximum correlation will

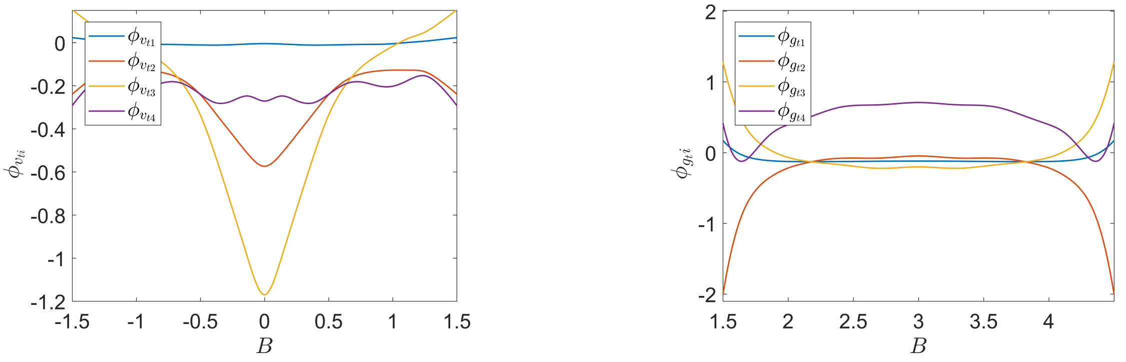

(a) Eigenfunctions $\phi_{v_{\mathrm{ti}}}(\cdot)$ **(b)** Eigenfunctions $\phi_{g_{\mathrm{ti}}}(\cdot)$

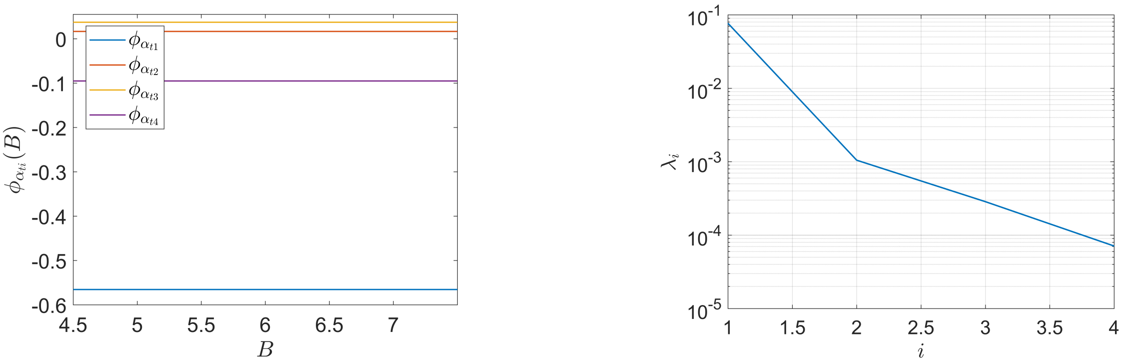

(c) Eigenfunctions $\phi_{\alpha_{\mathrm{ti}}}$ **(d)** Eigenvalues

Figure 34: Eigenfunction (a,b,c) and eigenvalues (d) of (203)

be observed in the $\alpha(\cdot,\cdot)$ because by construction all random realization are constant within the interval I_3. We set up the desired range for rescaling by choosing $n_{\min} = 1, n_{\max} = 2$. The rescaling coefficients are $A_{\mathrm{v}} = 0.0865, A_{\mathrm{g}} = 0.00018578, A_{\alpha} = 0.1080, C_{\mathrm{v}} = -3.6676, C_{\mathrm{g}} = 556.5599,$ $C_{\alpha} = 8.6404$, and $D_{\mathrm{v}} = D_{\mathrm{g}} = D_{\alpha} = 1$. The total number of experimental points is $N_p = 225$. The rescaled material functions and the assembled correlation function are depicted in Fig. 33. The smallest observed value for the coefficient of efficiency, therefore the worst fit, is $R_{\mathrm{a}} = 0.99998$. We solve the Fredholm integral equation by using the estimated sample covariance function for $N_{v_{\mathrm{t}}} = N_{g_{\mathrm{t}}} = 27$ basis functions. The first four eigenfunctions and eigenvalues are depicted in Fig. 34a-c and Fig. 34d, respectively. In order to estimate the error of the Galerkin discretization we repeated the computation of the eigenvalues and eigenfunctions for $N_{v_{\mathrm{t}}} = N_{g_{\mathrm{t}}} = 28$ basis functions. The maximal mean square error among the first four eigenfunctions is below $1.2 \cdot 10^{-4}$ and the maximal absolute error among the eigenvalues is below $4.9 \cdot 10^{-9}$.
We observe a relatively quick decay in the eigenvalues, see Fig. 34d which allows to truncate the KLE after $M = 4$ terms. According to (117) the relative error due to the truncation is 3.1%. It should be noticed that the relative information criterion is satisfied since $\Psi_M = 0.99 > 0.95$. The probability distribution functions of the four random variables are shown in Fig. 35. To obtain these pdfs we used a Gaussian kernel and we set the $\mathrm{MISE}(\hat{\rho}_{Y_i}) < 10^{-8}$, as it is defined with (126). The random variables that are introduced in Fig. 35 are bounded, i.e.,

$$||Y_i||_{L_\infty(\Omega,P)} \leq C_{Y_i}, \quad \forall i \geq 1 \tag{207}$$

where $C_{Y_i} \geq 0$. Based on this modeling approach we provide proofs in appendix B that some of the physical restrictions on the material functions can be preserved within the truncated KLE.

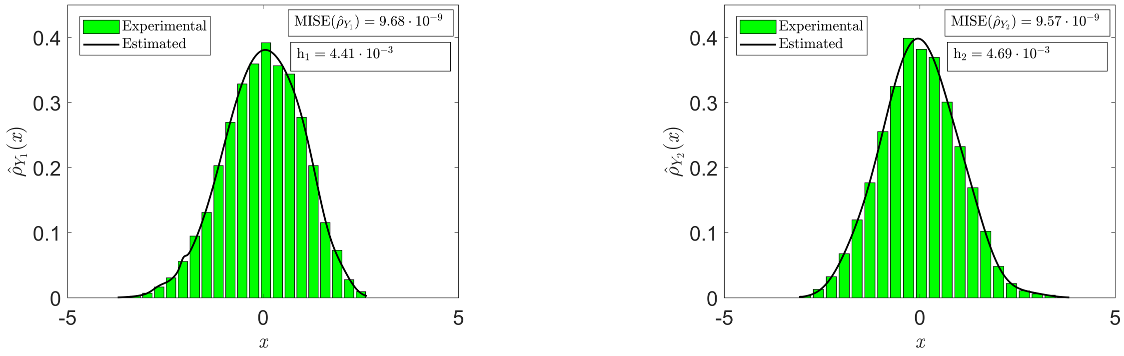

(a) Pdf of Y_1

(b) Pdf of Y_2

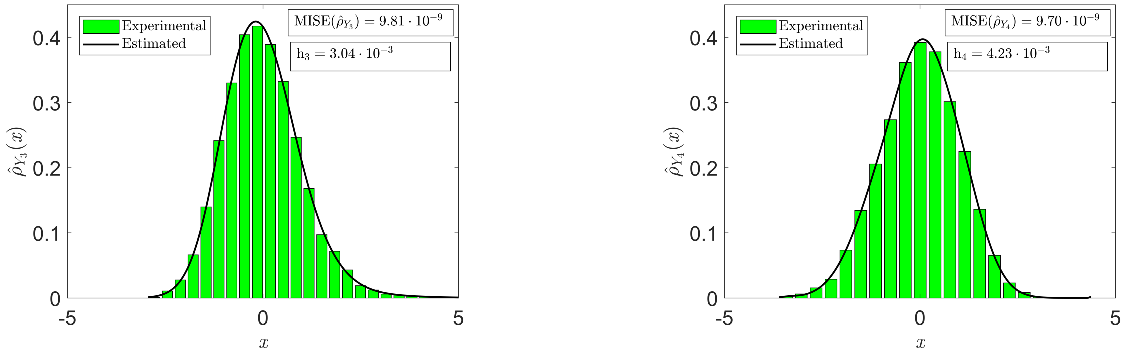

(c) Pdf of Y_3

(d) Pdf of Y_4

Figure 35: Probability distribution functions

5.7 Numerical example

In this section we will illustrate how to apply the stochastic Duhem model to compute the mean value and the standard deviation of the hysteresis loss in a simple toroidal transformer which is depicted in Fig. 36c. In practice one may be interested in the statistics of its technical parameters for different amplitudes of the current excitation. The primary coil is excited with a sinusoidal current $I(t) = I_0 \sin(\omega t)$, where $\omega = 1\mathrm{rad}/s$. The number of turns is $N_j = 1000$. The range of amplitudes is given as $I_0 \in [0.2, 0.55]$A. Eddy currents are neglected. Using the relationship between the magnetic field strength and the magnetic flux density we obtain

$$F(B(t), H_0, B_0) = \frac{N_t I(t)}{l}. \tag{208}$$

Hence, the unknown $B(t)$ is given as the root of the following nonlinear equation:

$$\Phi(B(t)) = F(B(t), H_0, B_0) - \frac{N_t I(t)}{l} = 0. \tag{209}$$

Once the trajectory is obtained in the BH plane, the hysteresis loss is readily computed as

$$P_\mathrm{h} = \frac{\mathrm{d}W_\mathrm{m}}{\mathrm{d}V} = \oint_C H \mathrm{d}B, \tag{210}$$

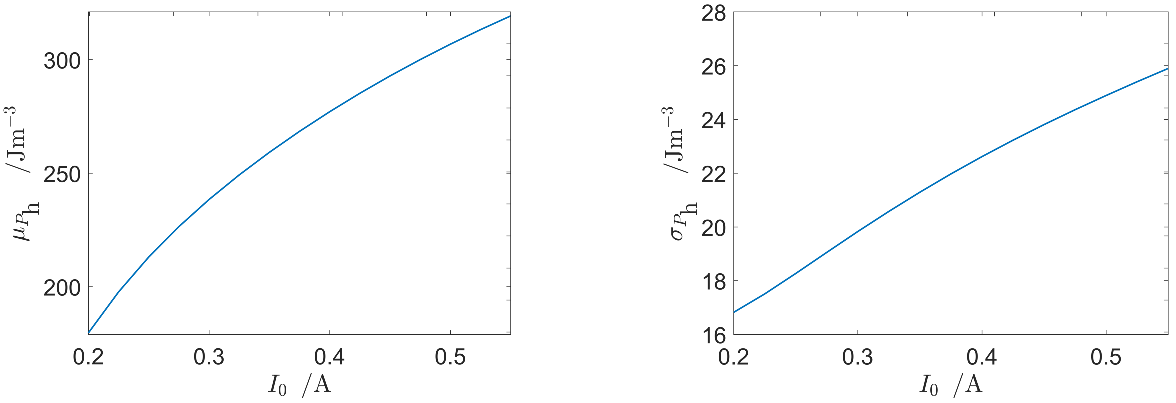

(a) The mean value of the hysteresis loss **(b)** The standard deviation of the hysteresis loss

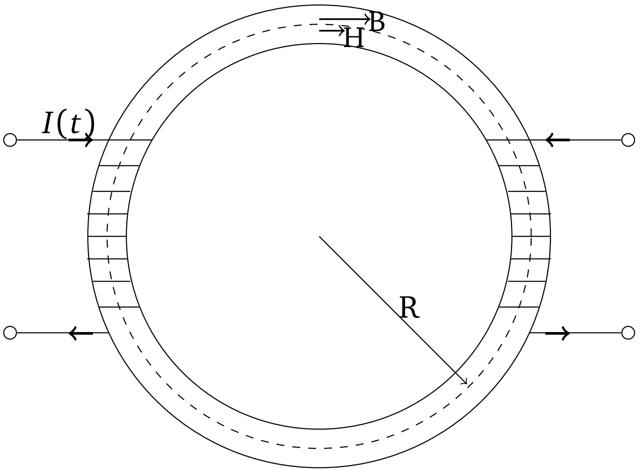

(c) Toroidal single phase transformer

Figure 36: Mean value (a) and standard deviation (b) of the hysteresis loss in a toroidal single phase transformer (c)

where W_m is the magnetic energy. The hysteresis loss is equivalent to the area encapsulated by the trajectory C and it expresses the energy dissipation per unit volume V due to the magnetic hysteresis. The mean value and the standard deviation are computed by using (153) and (154), respectively. We construct a tensor grid by using seven Gauss-Legendre collocation points per dimension. We repeated the computation for eight collocation points per dimension and estimated that the maximal relative error is below $9.6 \cdot 10^{-6}$ and $3.9 \cdot 10^{-4}$ for the mean value and standard deviation, respectively. The computed mean value and standard deviation are depicted in Fig. 36a and Fig. 36b, respectively.

5.8 Conclusion

In this chapter we introduced the magnetic hysteresis phenomenon. The Duhem model was explained and the basic equations stated. We explained how to model uncertainties arising from manufacturing imperfections. Namely, we proposed that the material functions describing the Duhem model can be modeled as cross-correlated random fields. The synthesized data from the stochastic Jiles-Atherton model justified our modeling approach. The approach was applied to a simple benchmark example, a toroidal transformer, in order to illustrate its practical relevance in a realistic scenario.

6 Hierachical Matrices and Lanczos Algorithm

The decay of the eigenvalues in the KLE provides a guideline for the truncation. Only the most influential terms, i.e., the eigenvalues with highest values are taken into account. The Krylov-subspace Lanczos algorithm, or only Lanczos algorithm, for computing the most important eigenvalues is a suitable choice, see [74, 75, 76, 77]. The Lanczos algorithm is an iterative algorithm where matrix vector multiplications involving the dense matrix $\boldsymbol{C}$ are required. The algorithm is significantly slowed down when the number of entries in $\boldsymbol{C}$ is relatively large. Memory issues also arise in order to store the matrix $\boldsymbol{C}$. There are two approaches suggested in the literature in order to remedy this issue. The first approach [78] is based on accelerating the matrix-vector multiplications in the Lanczos algorithm by using the fast multipole method and the second one, see [79], on the hierarchical matrix technique. In this work we adopt the hierarchical matrix compression techniques because it has been shown that it is simpler to implement in this context compared to the fast multipole method, see [80]. In the next sections we will introduce the simplest version of the Lanczos algorithm and the basic idea behind the hierarchical matrix technique. The sections that follow are a reformulation of the work presented in [24]

6.1 Lanczos algorithm

The generalized eigenvalue problem (146) can be rewritten as the standard one,

$$\boldsymbol{C}_{\mathrm{t}}\boldsymbol{f}_i = \lambda_i \boldsymbol{f}_i \tag{211}$$

where $\boldsymbol{C}_{\mathrm{t}} = \boldsymbol{V}^{-1}\boldsymbol{C}$. The main idea of the Lanczos method is to apply an orthonormal similarity transformation to the matrix $\boldsymbol{C}_{\mathrm{t}}$ as

$$\boldsymbol{T} = \boldsymbol{Q}^T\boldsymbol{C}_{\mathrm{t}}\boldsymbol{Q}, \tag{212}$$

where $\boldsymbol{Q} = [\boldsymbol{q}_1, ..., \boldsymbol{q}_M] \in \mathbb{R}^{N_{\mathrm{t}}\times M}$, and $\boldsymbol{q}_i \in \mathbb{R}^{N_{\mathrm{t}}}$, is an orthonormal basis of the Krylov subspace $\boldsymbol{K}_M := \mathrm{Span}\{\boldsymbol{q}_1, ..., \boldsymbol{q}_M\} = \mathrm{Span}\{\boldsymbol{q}_1, \boldsymbol{C}_{\mathrm{t}}\boldsymbol{q}_1, ..., \boldsymbol{C}_{\mathrm{t}}^{M-1}\boldsymbol{q}_1\}$. The matrix $\boldsymbol{T} \in \mathbb{R}^{M\times M}$ is a tridiagonal matrix given as

$$\boldsymbol{T} = \begin{bmatrix} \alpha_1 & \beta_1 & \dots & \dots & 0 \\ \beta_1 & \alpha_2 & \beta_2 & \dots & 0 \\ \vdots & \vdots & \ddots & \ddots & \vdots \\ \vdots & \vdots & \vdots & \alpha_{M-1} & \beta_{M-1} \\ 0 & 0 & 0 & \beta_{M-1} & \alpha_M \end{bmatrix}, \tag{213}$$

where the elements α_i and β_i as well as the orthonormal vectors $\{\boldsymbol{q}_i\}_{i=1}^M$ are computed by the iterative Algorithm 1. The similarity transformation preserves the eigenvalues, i.e., the first M eigenvalues of the matrix $\boldsymbol{C}_{\mathrm{t}}$ and $\boldsymbol{T}$ are identical. If $(\lambda_i, \boldsymbol{y}_i)$ is the $i-$th eigenpair of the tridiagonal matrix $\boldsymbol{T}$ then $(\lambda_i, \boldsymbol{Q}\boldsymbol{y}_i)$ is the $i-th$ eigenpair of the original matrix $\boldsymbol{C}_{\mathrm{t}}$. In practice the Lanczos algorithm encounters one drawback related to the matrix $\boldsymbol{Q}$. Namely, the orthogonality between the vectors is lost due to round-off errors. This issue has been explained in [81]. Thus, we shall consider full reorthogonalization, see Algorithm 1 line 10. For this thesis we have implemented Algorithm 1 in the C-programing language.

Algorithm 1 Lanczos algorithm

```
Initialization: $q_0 := 0$; $\beta_1 := 0$; $Q_1 := [q_1]$; $q_1 := \text{rand}(N_t, 1)$;
for $j = 2, 3, .., M$ do
    $\alpha_j := q_j^T C_t q_j$
    $r_j := C_t q_j - \alpha_j q_j - \beta_j q_{j-1}$
    $\beta_{j+1} := ||r_j||$
    if ($\beta_j = 0$) then
        return $Q \in \mathbb{R}^{N_t \times j}$ $\alpha_1, ..., \alpha_j$ and $\beta_1, ..., \beta_j$
        Break
    end if
    $r_j := r_j - QQ^T q_j$ full reorthogonalization
    $q_{j+1} = r_j / \beta_{j+1}$
    $Q_{j+1} = [Q_j, q_{j+1}]$
end for
return $Q \in \mathbb{R}^{N_t \times M}$ $\alpha_1, ..., \alpha_M$ and $\beta_1, ..., \beta_M$
```

6.2 Hierachical matrices

The key idea in the hierarchical matrix technique is to find subblocks in the dense matrix **C** that have small entries because they are far away from each other and weakly coupled and apply a low-rank approximation to them. The low rank approximation decreases the computational costs of the basic arithmetical operations such as matrix-matrix multiplication, addition and matrix-vector multiplication and reduces the memory storage requirements. The basic elements of building a hierarchical matrix representation of a dense matrix are cluster tree and block cluster tree. The indices of the potential candidates (subblocks) for a low rank approximation are kept in a block cluster tree whose elements are obtained as a Cartesian product between the elements of a cluster tree. For the fundamental theory behind the hierarchical matrices we refer to [82, 83, 84] and [85, 86, 87]. In the next three sections we give a brief explanation about the cluster tree, block cluster tree and the low rank approximation technique.

6.2.1 Cluster tree

Let I be an index set $I = \{0, 1, 2, ..., N_t - 1\}$. Each element $i \in I$ references a domain Ω_i described by

$$\Omega_i := \text{supp}(\phi_i). \tag{214}$$

A piecewise constant basis function is defined as

$$\phi_i(\boldsymbol{x}) := \begin{cases} 1 & \text{if } \boldsymbol{x} \in \tau_i \\ 0 & \text{otherwise.} \end{cases} \tag{215}$$

From (215) it is concluded that the domain Ω_i corresponds to the domain of τ_i, i.e., the $i -$th triangle in the triangular mesh.
The tree T_I is called a **cluster tree** over the index set I when the following conditions hold:

- The set I is the root of the cluster tree.

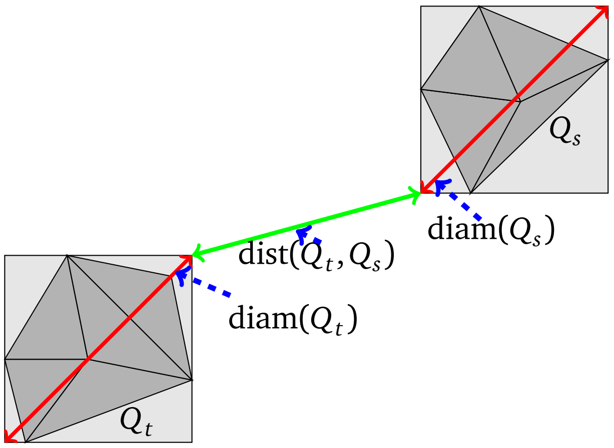

Figure 37: Example of two separated cluster domains

- If $t \in T_I$ is not a leaf, then it is a disjoint union of its sons $S(t)$.
- If $t \in T_I$ is a leaf, then $\#t \leq n_{\min}$ for a fixed number $n_{\min}$.

The operation # represents the cardinality of a set. There are many different approaches to build a cluster tree, for instance geometrical, algebraic, cardinality-balanced and box-tree clustering algorithms [88]. The basic idea behind of all the approaches is to split the index set I into two disjoint subsets which become sons of the root cluster. This procedure is repeated recursively for the son clusters. In this paper the box-tree clustering algorithm is used because of certain advantages over the other algorithms, see [88, Chapter 2, p. 30].
The clusters $t \in T_I$ define cluster domains Ω_t,

$$\Omega_t := \bigcup_{i \in t} \operatorname{supp}(\phi_i), \tag{216}$$

i.e., Ω_t is the minimal subset of $\mathbb{R}^2$ that contains the supports of the basis functions $\{\phi_i\}_{i\in t}$. The potential candidates for low rank approximation are those subblocks in the matrix $\mathbf{A}$ whose indices are kept in the clusters $t, s \in T_I$ and their domains Ω_t and Ω_s defined with equation (216) satisfy the admissibility condition,

$$\min(\operatorname{diam}(\Omega_t), \operatorname{diam}(\Omega_s)) \leq \eta \operatorname{dist}(\Omega_t, \Omega_s), \tag{217}$$

where diam$(\cdot)$ is the Euclidean diameter of a set and dist$(\cdot,\cdot)$ is the Euclidean distance of two sets. The parameter η allows to adjust the number of admissible blocks. In practice, computing the diameters of possibly complicated domains Ω_t and Ω_s, as well the distance between them, can be a time consuming procedure. Thefore, they are replaced by axis-parallel rectangles Q_t and Q_s such that $\Omega_t \subseteq Q_t$ and $\Omega_s \subseteq Q_s$ holds as it is shown in Fig. 37. The admissibility now reads

$$\min(\operatorname{diam}(Q_t), \operatorname{diam}(Q_s)) \leq \eta \operatorname{dist}(Q_t, Q_s). \tag{218}$$

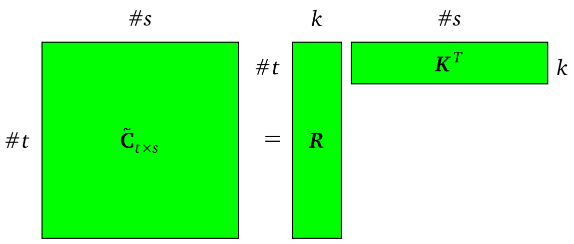

Figure 38: Low rank approximation of a subblock

6.2.2 Block cluster tree

The tree $T_{I\times I}$ is called a **block cluster tree** over the Cartesian product $I \times I$ if the following holds:

- The root of the block cluster tree is $I \times I$.
- Each element $b \in T_{I\times I}$ has the form $b = t \times s$ where $t, s \in T_I$.

The block cluster tree is built by taking a Cartesian product between the elements $t, s \in T_I$ that belong to the same level in the cluster tree T_I and the procedure is repeated recursively until the admissibility condition is satisfied or t and s are leaves. The block cluster tree is a quadtree with leaves on different levels that could be admissible or inadmissible. A hierarchical matrix represents also a cluster tree with an equivalent structure as the block cluster tree. The inadmissible leaves of the hierarchical matrices contain matrices in the standard full format and the admissible leaves contain low rank approximated matrices.

6.3 Low rank approximation

The subblock $\mathbf{C}_{t\times s}$ is approximated by the matrix subblock $\tilde{\mathbf{C}}_{t\times s}$, if the clusters t and s satisfy the admissibility condition as

$$\tilde{\mathbf{C}}_{t\times s} = \mathbf{R}\mathbf{K}^T, \tag{219}$$

where $\mathbf{R} \in \mathbb{R}^{p\times k}$, $\mathbf{K} \in \mathbb{R}^{q\times k}$ and $p = \#t$, $q = \#s$. Pictographically this is illustrated in Fig. 38. The rank is denoted as k. The matrices $\mathbf{R}$ and $\mathbf{K}$ are computed by using the adaptive cross approximation (ACA) technique, see [89]. ACA computes a low rank approximation with a-priori given accuracy ε

$$\left\|\mathbf{C}_{t\times s} - \tilde{\mathbf{C}}_{t\times s}\right\|_F \leq \varepsilon \left\|\mathbf{C}_{t\times s}\right\|_F, \tag{220}$$

where $\|\cdot\|_F$ is the Frobenius norm.

6.4 Numerical experiments

The details of the most of the computations that follow can be found in [24]. For the hierarchical matrix part we use the H2Lib library [90]. To illustrate the relevance of the hierarchical matrix compression we adopt the single phase transformer [43]. We will consider the magnetic reluctivity as a linear and isotropic spatial random field, i.e., $\nu(\boldsymbol{x},\theta) = F_s(\boldsymbol{x},\theta)$. The approximated random field by the truncated KLE is given as

$$\nu(\boldsymbol{x},\theta) \approx \nu_M(\boldsymbol{x},\boldsymbol{Y}) = \overline{\nu}(\boldsymbol{x}) + \sum_{i=1}^{M} \sqrt{\lambda_i} f_i(\boldsymbol{x}) Y_i(\theta), \tag{221}$$

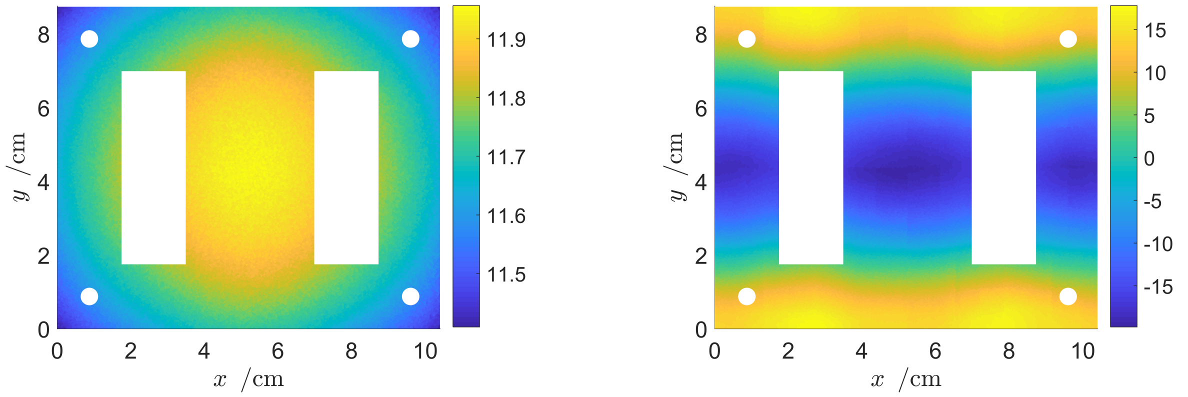

(a) 1st Eigenfunction

(b) 5th Eigenfunction

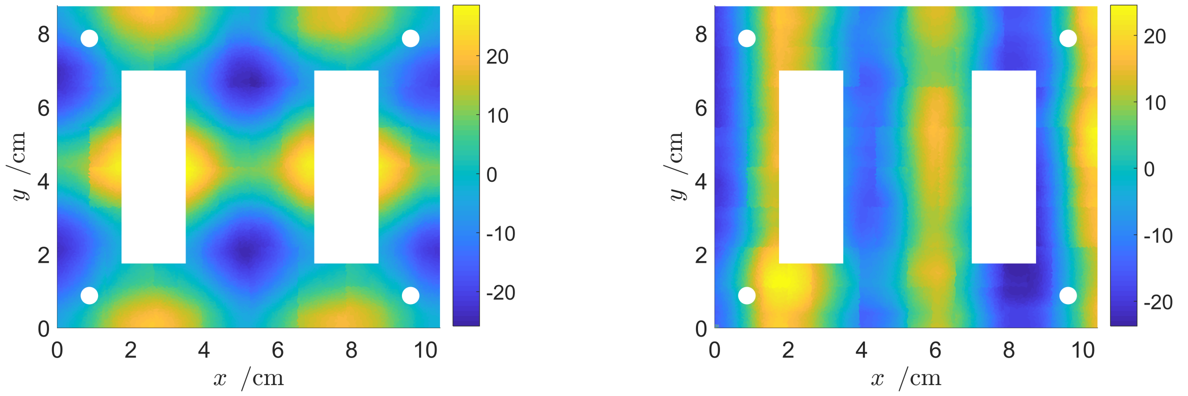

(c) 8th Eigenfunction

(d) 10th Eigenfunction

Figure 39: The 1st (a) 5th (b) 8th (c) 10th (d) eigenfunction

as it was explained in Section 4.4. The mean value of the random field is $\overline{\nu}(\boldsymbol{x}) = 795.774\mathrm{H}^{-1}\mathrm{m}$. The covariance function is assumed to be the exponential (149). The generalized problem (211) is solved for the $N_\mathrm{t} = 24810$ triangles, $d = 100\mathrm{cm}$, $\sigma = 1$. Some of the eigenfunctions are depicted in Fig. 39. The same eigenvalue problem is solved for different correlation lengths and the decay of the eigenvalues is shown in Fig. 41. For the hierarchical matrix compression part we used $n_\mathrm{min} = 256$, $\eta = 1.0$ and $\varepsilon = 0.01$. In order to obtain visual insight into the structure of the hierarchical matrix we show two of them in Fig. 40.

N_t	$\mathbf{C}$	$\tilde{\mathbf{C}}(d = 5\mathrm{cm})$	Δ	$\tilde{\mathbf{C}}(d = 200\mathrm{cm})$	Δ
3838	112 MB	59 MB	$2.25 \cdot 10^{-4}$	57 MB	$1.05 \cdot 10^{-3}$
9102	632 MB	182 MB	$3.39 \cdot 10^{-4}$	170 MB	$1.25 \cdot 10^{-3}$
24697	4653 MB (nem)	599 MB	———	548 MB	———
35295	9504 MB (nem)	942 MB	———	861 MB	———

Table 1: Memory requirements for the full format and hierarchical format of matrices. Details about this computations can be found in [24, Table 1].

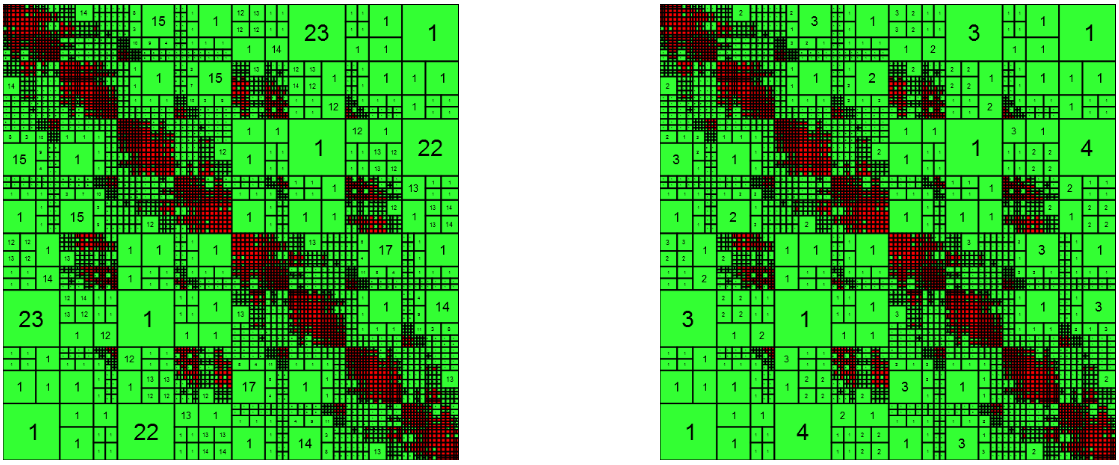

(a) Hierarchical matrix for $d = 10\text{cm}$ **(b)** Hierarchical matrix for $d = 100\text{cm}$

Figure 40: Hierarchical matrices for different correlation lengths

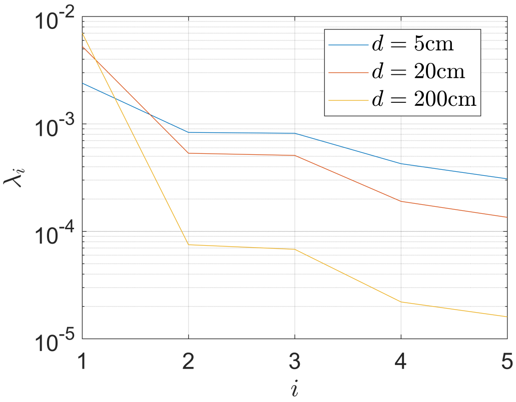

Figure 41: Eigenvalues for $d = 5\text{cm}, 20\text{cm}, 200\text{cm}$, [24, Fig. 4].

6.5 Memory storage benefits

The memory requirements in order to store the full matrix $\mathbf{C}$ and the hierarchical matrix $\tilde{\mathbf{C}}$ as well as the l_2-norm due to the hierarchical compression are shown in table 3. The correlation lengths $d = 5\text{cm}$ and $d = 10\text{cm}$ are considered. The error due to the hierarchical representation is given as

$$\Delta = \frac{\left\|\mathbf{C} - \tilde{\mathbf{C}}\right\|_{l_2}}{\|\mathbf{C}\|_{l_2}}. \tag{222}$$

As it can be seen from table 3, for $N_t = 3838$ the memory storage benefits are not significant. However, when $N_t \geqslant 24697$ the memory allocation fails on a 64 bit desktop computer with 24 GB RAM memory (not enough memory - "nem"). This kind of memory issues have been are also reported in [79]. The data in table 3 shows that the compression of the dense matrix becomes better when the correlation length is increased.

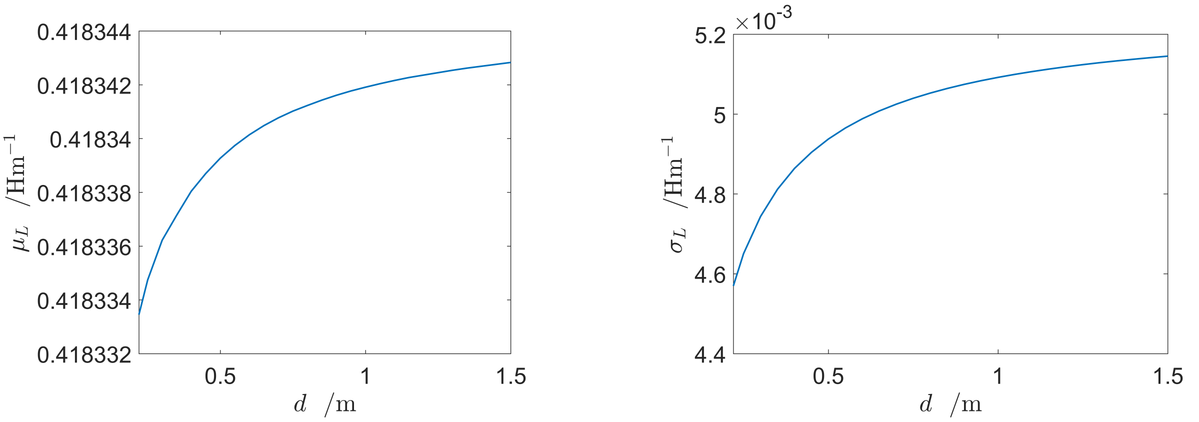

(a) Mean value, [24, Fig. 7] **(b)** Standard deviation, [24, Fig. 7]

Figure 42: Mean value (a) and standard deviation of the inductance (b)

6.6 Statistics of the inductance

For the computation of the mean value and the standard deviation of the inductance we will consider the static case. If we use the approximated random magnetic reluctivity (221) the following expression is obtained for the stiffness matrix

$$\mathbf{K} \approx \overline{\mathbf{K}} + \sum_{i=1}^{M} \overline{\mathbf{K}}_i Y_i(\theta). \tag{223}$$

We set the number turns in the primary coil $N_\mathrm{j} = 260$ and consider random variables with uniform pdf. We compute the statistics of the inductance in the range of correlation lengths $d = [20, 160]\mathrm{cm}$ and $\sigma = 10$. For the stochastic collocation method we use a polynomial degree $l = 2$ in each dimension. We chose the number of random variables based on the relative information criterion $\Psi_M > 0.95$. The mean value and the standard deviation are shown in Fig. 42.

6.7 Discussion on the physical interpretation

When we considered uncertainties in the magnetic hysteresis the covariance function was computed from synthesized data. Even though this data cannot be considered as really experimental data still it is a good replacement because it is generated by a model that is constructed to capture uncertainties. It has been reported in the literature that the manufacturing process modifies spatially the magnetic properties, see [91, 92]. To this end we did not succeed find data documented in such a way that we can extract the covariance function and gain insight into the qualitative behavior of the spatial uncertainties. Thus we assumed the covariance function and the PDF of the random variables.

6.8 Conclusion

In this chapter we use the hierarchical matrix compression and the Lanczos algorithm in order to compute efficiently the KLE of a spatial spatial random field. The compressed matrices were used in the iterative Lanczos algorithm in order to solve a generalized eigenvalue problem. This technique plays a significant role in reducing memory requirements in some scenarios where the memory allocation would not have even been possible if the full format was used. The approach was used to compute the statistics of the inductance of a single phase transformer for illustrating its practical relevance.

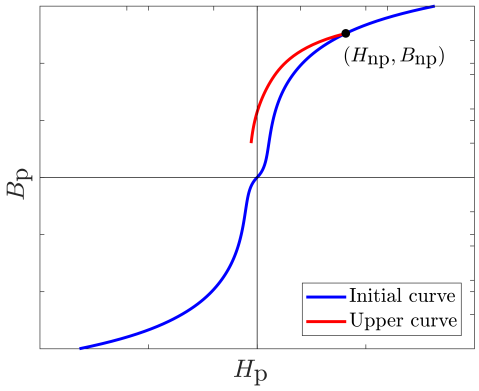

Figure 43: Initial and upper nonlinear curve and turning point

7 Simulation of Remanence Effects in the Combined Function Magnet

When hysteretic properties are neglected one can conclude that if the current sources are switched off (their value is set to zero) the magnetic field vanishes. If eddy currents are present in the system they will remain for some transient period and their effect (they act as a secondary source for the magnetic field) will eventually disappear. From the general description of magnetic hysteresis that we gave in chapter 5, Fig. 26, one can see that even when the current source is switched off the toroidal core remains in a magnetized state. It is this remanent magnetization that influences the performance of electrical devices, see for example [93, 94, 95]. The left over magnetization has to be taken into account in the simulation in order to properly design the electrical device of interest. Within the scope of this thesis only the combined function magnet explained in chapter 3 will be the subject of this additional consideration.

A simplified analysis of the combined function magnet has been carried out by using a magnetic equivalent circuit (MEC) approach in [50]. The MEC method has two benefits. First it is computationally cheap since the device is represented as network of lumped elements where classical or modified nodal analysis can be applied. Second, it is comprehensive for electrical engineers because it follows their intuition gained from circuit theory. However, in the same work [50] it has been shown, by comparison between the magnetic flux densities in the center of the device computed by a 2D FE model and MEC, that even an improved MEC gives less accurate results.

In [50] the remanence magnetization is computed by drawing a tangent line at the current working point on the $B-H$ curve. The point at which the tangent line intersects the B_{p}—axis, for $H_{\text{p}} = 0$, is incorporated as constant source of magnetic flux density in the circuit representation. The magnetic flux density is an analogy to an electric current in classical electric circuits.

We propose an extension to the work in [50] in two aspects. First, instead of using tangent lines we propose computing the actual demagnetization curves by using the Duhem model. Second, we propose a solution of the governing equation in which the magnetic reluctivity is extracted from the computed curves. To proceed we will first redefine the magnetic reluctivity for the hysteretic case and we shall conceptually explain how to conduct numerical simulation with hysteretic properties taken into account.

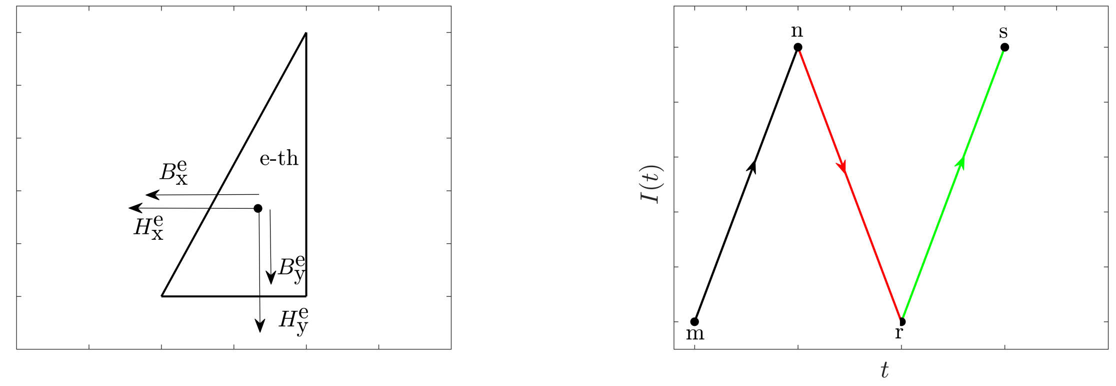

(a) One triangular element from the mesh

(b) Electric current signal

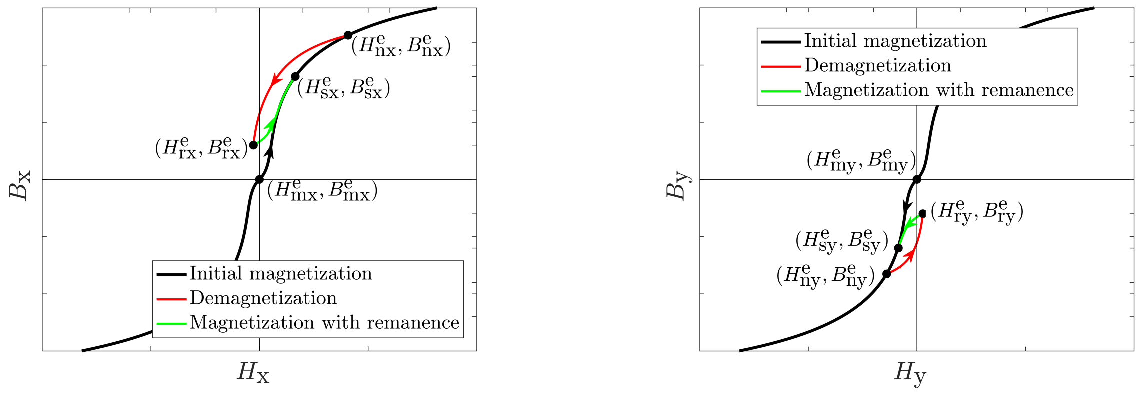

(c) Magnetization history of the x—component

(d) Magnetization history of the y—component

Figure 44: Magnetization history of the $\mathrm{x}-\mathrm{y}$ components (c-d) in the e—th element (a) under the excitation (b)

7.1 Nonlinear magnetic reluctivity with magnetic hysteresis

Let us consider the initial and upper $B-H$ curve as it is depicted in Fig. 43. We propose a definition of the magnetic reluctvity which w.r.t. the turning point $\left(H_{\mathrm{np}}, B_{\mathrm{np}}\right)$ given as

$$\nu_{\mathrm{pp}}(B_{\mathrm{p}}) := \frac{H_{\mathrm{p}} - H_{\mathrm{np}}}{B_{\mathrm{p}} - B_{\mathrm{np}}}. \tag{224}$$

This definition gives rise to the following constitutive relation

$$\boldsymbol{H} = \overline{\nu}(\boldsymbol{B} - \boldsymbol{B}_{\mathrm{n}}) + \boldsymbol{H}_{\mathrm{n}}, \tag{225}$$

which can be rewritten as

$$\boldsymbol{H} = \overline{\nu}\boldsymbol{B} + \boldsymbol{H}_{\mathrm{n}}^{\star}, \tag{226}$$

where

$$\boldsymbol{H}_{\mathrm{n}}^{\star} = \boldsymbol{H}_{\mathrm{n}} - \overline{\nu}\boldsymbol{B}_{\mathrm{n}}. \tag{227}$$

The vector of the magnetic field strength given by (227) can be thought of as accumulated, i.e., leftover magnetic field from a previous operation mode. Alternatively one can think of $\boldsymbol{H}_{\mathrm{n}}^{\star}$ as magnetic field strength arising from a permanent magnet. The magnetic reluctivity defined in (38) preserves the positivity w.r.t. the turning point $\left(H_{\mathrm{np}}, B_{\mathrm{np}}\right)$.

7.2 Simulation flow

When the combined function magnet is never set into a working mode before all of the triangular elements belong to a region whose magnetic properties can be described via the initial magnetization curve. This holds true for the initial excitation, i.e., when the signal depicted in Fig. 44b goes from point m to point n. During this portion of the excitation signal, the region of e—th the element is brought from the state $(0,0)$ to $(H^{\mathrm{e}}_{\mathrm{np}}, B^{\mathrm{e}}_{\mathrm{np}})$, see Fig. 44c-d. The constitutive relation in this case is given as follows

$$\boldsymbol{H}^{\mathrm{e}} = \overline{\nu}^{\mathrm{e}}\boldsymbol{B}^{\mathrm{e}} + \boldsymbol{H}^{\mathrm{e}\star}_{\mathrm{m}} \quad t \in [t_{\mathrm{m}}, t_{\mathrm{n}}], \tag{228}$$

where $\boldsymbol{H}^{\mathrm{e}\star}_{\mathrm{m}} = (H^{\mathrm{e}\star}_{\mathrm{mx}}, H^{\mathrm{e}\star}_{\mathrm{my}}) = (0,0)$. When the electric currents starts to decrease, i.e., it goes from n to r, see Fig. 44b, the turning point occurs. In fact each triangle of the mesh can be described via its own turning point and descending portion of the $B - H$ curve computed by (174). The constitutive relation now reads

$$\boldsymbol{H}^{\mathrm{e}} = \overline{\nu}^{\mathrm{e}}\boldsymbol{B}^{\mathrm{e}} + \boldsymbol{H}^{\mathrm{e}\star}_{\mathrm{n}} \quad t \in [t_{\mathrm{n}}, t_{\mathrm{r}}]. \tag{229}$$

During this phase the e—th triangle is brought from the state $(H^{\mathrm{e}}_{\mathrm{np}}, B^{\mathrm{e}}_{\mathrm{np}})$ to $(H^{\mathrm{e}}_{\mathrm{rp}}, B^{\mathrm{e}}_{\mathrm{rp}})$. When the electric current signal reaches the point r the device ends up in a certain status that can be computed if the governing equation is derived based on (229) and solved. Similarly, the constitutive relation, when the device is set again into a working mode by the r-q portion of the excitation signal, the constitutive relation is given as

$$\boldsymbol{H}^{\mathrm{e}} = \overline{\nu}^{\mathrm{e}}\boldsymbol{B}^{\mathrm{e}} + \boldsymbol{H}^{\mathrm{e}\star}_{\mathrm{r}} \quad t \in [t_{\mathrm{r}}, t_{\mathrm{s}}]. \tag{230}$$

The magnetization history of the $\mathrm{x}-\mathrm{y}$ components e—th element is depicted in Fig. 44c-d.

7.3 Governing equation and its numerical approximation

Let us denote the different states with $\mathrm{c} \in \{\mathrm{m}, \mathrm{n}, \mathrm{r}, \mathrm{s}\}$. The constitutive relation can be expressed as

$$\boldsymbol{H} = \overline{\nu}\boldsymbol{B} + \boldsymbol{H}^{\star}_{\mathrm{c}}. \tag{231}$$

By using the magnetic vector potential representation we obtain

$$\nabla \times (\overline{\nu}\nabla \times \boldsymbol{A}) = \boldsymbol{J}_{\mathrm{o}} - \nabla \times \boldsymbol{H}^{\star}_{\mathrm{c}}, \tag{232}$$

which under the assumptions of the $2D$ simplification reads

$$-\nabla \cdot (\overline{\nu}_{\mathrm{d}}\nabla A_{\mathrm{z}}) = J_{\mathrm{z}} - \left(\frac{\partial H^{\star}_{\mathrm{cy}}}{\partial x} - \frac{\partial H^{\star}_{\mathrm{cx}}}{\partial y}\right). \tag{233}$$

The eddy currents are neglected because the core is usually laminated in z—direction. We derive the weak formulation as follows

$$-\int_D v\nabla \cdot (\overline{\nu}_{\mathrm{d}}\nabla A_{\mathrm{z}})\mathrm{d}\boldsymbol{x} = \int_D J_{\mathrm{z}} v\,\mathrm{d}\boldsymbol{x} - \int_D \left(\frac{\partial H^{\star}_{\mathrm{cy}}}{\partial x} - \frac{\partial H^{\star}_{\mathrm{cx}}}{\partial y}\right) v\,\mathrm{d}\boldsymbol{x}. \tag{234}$$

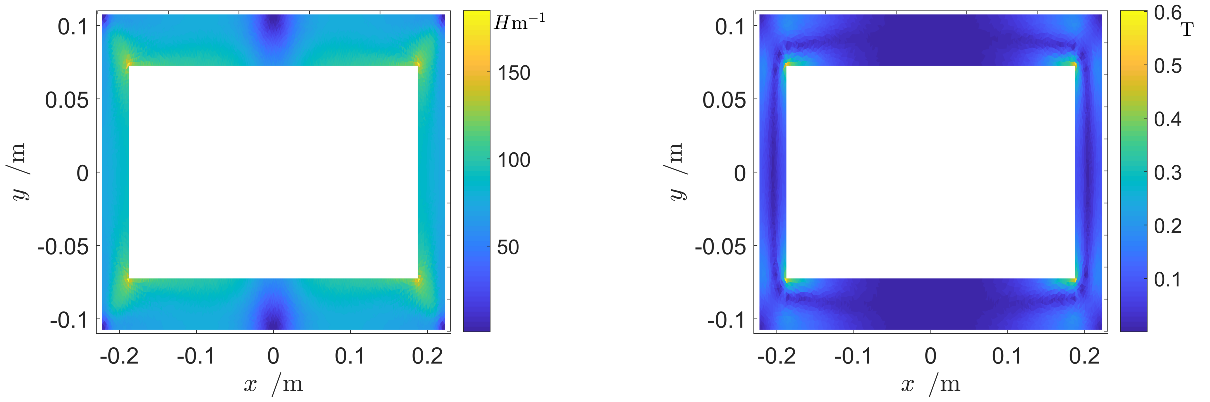

(a) Remanent magnetic field strength **(b)** Remanent magnetic flux density

Figure 45: Remanent magnetic field strength (a) and remanent magnetic flux density (b)

After applying the following integration by parts equations

$$\int_D v \frac{\partial H^\star_{\mathrm{cy}}}{\partial x} \mathrm{d}\boldsymbol{x} = -\int_D H^\star_{\mathrm{cy}} \frac{\partial v}{\partial x} \mathrm{d}\boldsymbol{x} + \int_{\partial D} \underbrace{v\left(\boldsymbol{n_0} H^\star_{\mathrm{cy}}\right)}_{0} \mathrm{d}\boldsymbol{x}, \tag{235}$$

$$\int_D v \frac{\partial H^\star_{\mathrm{cx}}}{\partial y} \mathrm{d}\boldsymbol{x} = -\int_D H^\star_{\mathrm{cx}} \frac{\partial v}{\partial y} \mathrm{d}\boldsymbol{x} + \int_{\partial D} \underbrace{v\left(\boldsymbol{n_0} H^\star_{\mathrm{cx}}\right)}_{0} \mathrm{d}\boldsymbol{x}, \tag{236}$$

the weak formulation equation is written as

$$\int_D \overline{\nu}_{\mathrm{d}} \nabla A_{\mathrm{z}} \cdot \nabla v \mathrm{d}x = \int_D J_{\mathrm{z}} v \mathrm{d}\boldsymbol{x} + \int_D \left(H^\star_{\mathrm{cy}} \frac{\partial v}{\partial x} - H^\star_{\mathrm{cx}} \frac{\partial v}{\partial y} \right) \mathrm{d}\boldsymbol{x}. \tag{237}$$

The discrete FEM equation of (237) reads

$$\boldsymbol{K}^n \boldsymbol{a}^n = \boldsymbol{F}^n + \boldsymbol{F}^\star_c. \tag{238}$$

The nonlinear analysis that was introduced in chapter 3 applies here as well with an additional vector $\boldsymbol{F}^\star_c$ incorporated into the right hand side of the equation that is supposed to capture the remanence effects.

7.4 Simulation via three static simulations

When the eddy currents are neglected, the analysis of the remanence effects can be significantly simplified by considering a static simulation instead of a transient. Namely, if one is interested only in the final values for the magnetic field and field harmonics then three magnetostatics problems are solved. The Newton-Raphson equation reads

$$\boldsymbol{J}^k(\boldsymbol{a}^{k+1} - \boldsymbol{a}^k) = \boldsymbol{F}^k + \boldsymbol{F}^\star_c - \boldsymbol{K}^k \boldsymbol{a}^k, \tag{239}$$

where $\boldsymbol{J}^k$ is the static Jacobian matrix which is obtained when (74) is assembled without the eddy current part. For illustration purposes we set up a numerical simulation. We use $N_{\mathrm{sw}} =$

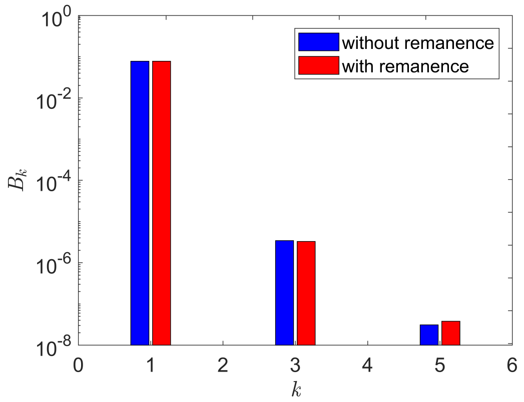

Figure 46: Field harmonics with and without remanence magnetization

Field harmonic	Nominal	Mean	Std
B_1	0.077591 T	0.077862 T	4.30 10^{-4} T

Table 2: Mean value and standard deviation of the field harmonics with considering a remanent magnetic field

100 and $I_{\mathrm{sw}} = 90A$. The number of triangles is $N_{\mathrm{t}} = 51473$. The combined function magnet is encapsulated into a circular computational domain with radius of 0.27m. To compute the remanence magnetic field we switch off the source current. For computing the demagnetization curves and magnetization curves we used the Jiles-Atherton model for $M_s = 1.6376 \cdot 10^6$, $k_1 = 189$, $k_0 = 409.1523$, $\sigma = 0.99$, $c = 0.5628$, $a = 981.8209$ and $\alpha = 0.0017$ and we identified the corresponding material functions of the Duhem model. The tolerance in the Newton-Raphson method is set to 10^{-6}. The spatial distributions of the amplitudes of the remanent magnetic field strength and the magnetic flux density are depicted in Fig. 45a and Fig. 45b, respectively. The remanent field is particularly strong at the sharp edges. This is expected since the magnetic field has the highest value at this location. The first three field harmonics with and without remanence magnetization are depicted in Fig. 46. The remanence magnetization gives a slight rise to the fifth multipole. In this scenario the influence of the remanence magnetization is negligible.

7.5 Statistics of the field harmonics

In order to compute to the statistics of the field harmonics we use the stochastic collocation method as described in chapter 4. We set the polynomial degree to be $l = 3$ in each direction. For the KLE we use the same data used in chapter 5. We assume that random variables in the KLE are uniformly distributed. The mean value and the standard deviation of the first field harmonic with considering remanence effects are shown in Table 2.

7.6 Conclusion

In this section a methodology was presented for simulating remanence effects in a combined function magnet. The magnetic reluctivity was redefined in the hysteretic case with respect to the turning point. The governing equations were derived based on the redefined magnetic reluctivity. On top of the deterministic scenario we computed the statistics of the first field harmonics. The analysis was significantly simplified by considering only three static simulations and neglecting eddy currents. The results presented in Fig. 45 show that if hysteretic properties are neglected, remanence effect would have been unpredicted by the analyst.

8 Summary and Outlook

8.1 Summary

In this thesis, we dealt with modeling uncertainties in the magnetic behavior law of ferromagnetic materials. There are two main contributions of this work. First, a modeling approach was proposed to model aleatoric uncertainties that occur in ferromagnetic materials due to manufacturing imperfections. The approach is based on multivariate random fields and a phenomenological type of hysteresis model known as the Duhem model. The key observation in this case was that a probabilistic hysteresis model can be obtained by modeling the material functions of the model as cross-correlated random field. The presence of correlation in the identified material function, see Fig. 33a-c, was observed. The cross-correlation between the data was further investigated. It was found that $\alpha(\cdot)$ exhibits strong and weak correlation with $g(\cdot)$ and $f(\cdot)$, respectively. The functions individually manifested strong self-correlation. The implication of the correlation was a quick decay of the eigenvalues which enabled approximating the trivariate random field by taking only four terms in the Karhunen-Loève expansion. The second contribution of this thesis is related with the application the hierarchical matrix technique to compress dense matrices arising from the Galerkin discretization in the spatial domain. We implemented our own solver based on the Lanczos algorithm where in the iterative steps we used a hierarchical format of the dense matrices. Huge memory savings could be achieved in this way. We observed better compression for strongly correlated random fields. The proposed modeling approach was further used to compute a mean value and a standard deviation of the an important QoIs by using the stochastic collocation method.

8.2 Outlook

There are some interesting and also important aspects of the presented work that could not be covered in this thesis. When we dealt with uncertainties occurring in the magnetic hysteresis case we supported the theoretical work with synthesized data for the major loop cycles by using the stochastic Jiles-Athrton model. On the other hand when we addressed the spatial uncertainties the covariance function and the PDF of the random variables were assumed to be the exponential and uniform distribution function, respectively. It would be interesting to assess these assumptions in view of real data, although it is difficult to measure spatial variation in practice.

Regarding the magnetic hysteresis some questions were not entirely addressed. The physical restriction on the material functions given with the Assumption 10 was not proven to hold within the truncated KLE. This assumption is responsible to guarantee a monotonic response of the ferromagnetic material. In our computations we never observed any violations of this assumption. The obtained $B-H$ paths were always monotone when the multivariate random field was approximated with the truncated KLE. This gives us an intuitive feeling that the assumption holds in the stochastic setting. However, a rigorous proof is still lacking. We already provided a proof for the Assumption 9. It also remained unclear a priori how large the number of random variables has to be chosen such that the property is not violated. The proof that we provided only shows that it is possible to satisfy the physical property by eventually taking a certain number of random variables. In case of proving the Assumption 10 answering the same question is required.

The number of collocation points in the stochastic collocation method can be reduced by using the approach known as anisotropic sparse grid, see [96]. The basic idea is to take lower polynomial degree in some of the directions. In our case the decay of the eigenvalues in the KLE provides a guideline in which direction one can reduce the number of points. It would be interesting to use the anisotropic approach for the introduced benchmark examples in this thesis.

In the last chapter we provided a simplified static analysis of the field quality in a combined function magnet. What would be interesting for future work is a full transient analysis with uncertainty quantification. Another simplification in this thesis was the 2D representation of the benchmark examples. It will be interesting to consider sophisticated 3D models in future.

A Stochastic Jiles-Atherton model

In this section the basic equations and parameters related to the Jiles-Atherton model are given. The derivative of the magnetization with respect to the magnetic flux density is given as, see [20]

$$\frac{\mathrm{d}M}{\mathrm{d}B} = \frac{(1-c)\frac{\mathrm{d}M_{\mathrm{irr}}}{\mathrm{d}B_e} + c\frac{\mathrm{d}M_{\mathrm{anh}}}{\mathrm{d}B_e}}{1+\mu_0(1-c)(1-\alpha)\frac{\mathrm{d}M_{\mathrm{irr}}}{\mathrm{d}B_e} + \mu_0 c(1-\alpha)\frac{\mathrm{d}M_{\mathrm{anh}}}{\mathrm{d}B_e}}. \tag{240}$$

In this relation, M_{anh} and M_{irr} denote respectively the anhysteretic magnetization and the irreversible magnetization. With B_e the effective magnetic flux density is denoted. The anhysteretic magnetization is computed as,

$$M_{\mathrm{anh}} = M_s(\coth\frac{H+\alpha M}{a} - \frac{a}{H+\alpha M}), \tag{241}$$

and its derivative with respect to B_e,

$$\frac{\mathrm{d}M_{\mathrm{anh}}}{\mathrm{d}B_e} = \frac{M_s}{a\mu_0}(1-\coth^2(\frac{H+\alpha M}{a}) + (\frac{a}{H+\alpha M})^2). \tag{242}$$

The irreversible magnetization is given with the following relation:

$$M_{\mathrm{irr}} = \frac{M - cM_{\mathrm{anh}}}{1-c}, \tag{243}$$

and its derivative,

$$\frac{\mathrm{d}M_{\mathrm{irr}}}{\mathrm{d}B_e} = \frac{M_{\mathrm{anh}} - M_{\mathrm{irr}}}{\mu_0 k\delta}. \tag{244}$$

The directional parameter is denoted as δ where,

$$\delta = \begin{cases} 1 & \dot{B} > 0 \\ -1 & \dot{B} < 0. \end{cases} \tag{245}$$

The equations (244) and (242) are substituted into (240) with their right hand sides. The parameter k is given as follows:

$$k = k_1 + k_0 e^{-\frac{H^2}{2\sigma^2}}. \tag{246}$$

In the Jiles Atherton model there are 6 parameters (M_s,k_0,c,a,α,σ) which are related to the magnetic properties of the material under interest.
The equation (240) is actually used in the following update relationship:

$$M_{i+1} = M_i + \frac{\mathrm{d}M}{\mathrm{d}B}\Delta B_i. \tag{247}$$

And the new value M_{i+1} is used to obtain the new value of the magnetic field strength:

$$H_{i+1} = \frac{B_{i+1}}{\mu_0} - M_{i+1}. \tag{248}$$

In the stochastic Jiles-Atherton model the discrete parameters are modeled as random variables whose probability distribution functions are depicted in Fig. 47.

The correlation matrix is given in the following table:

	M_s	k_0	c	a	α	σ
M_s	1	−0.509	−0.837	0.959	0.942	0.567
k_0	−0.509	1	0.746	−0.415	−0.362	−0.918
c	−0.837	0.746	1	−0.787	−0.759	−0.778
a	0.959	−0.415	−0.787	1	0.99	0.516
α	0.942	−0.362	−0.759	0.992	1	0.470
σ	0.567	−0.918	−0.778	0.5162	0.470	1

Table 3: Correlation matrix from [20]

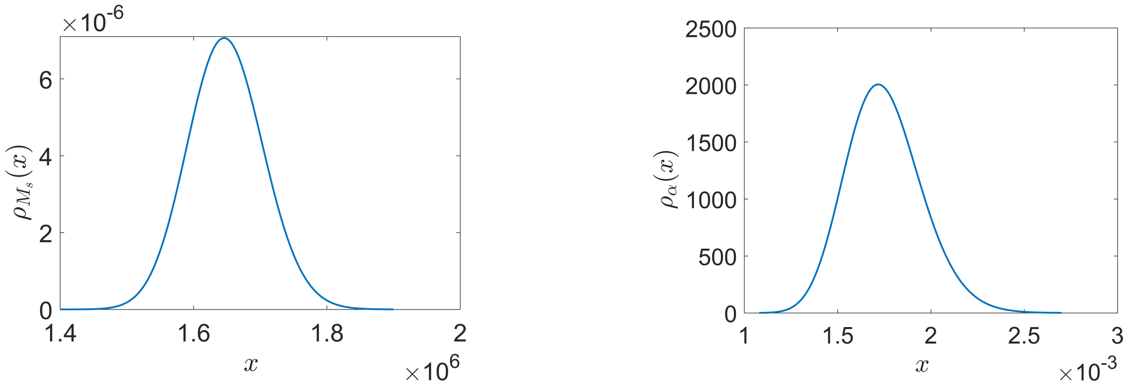

(a) $M_s = \mathrm{logN}(14.315, 0.0343)$ **(b)** $\alpha = \mathrm{logN}(-6.3536, 0.1151)$

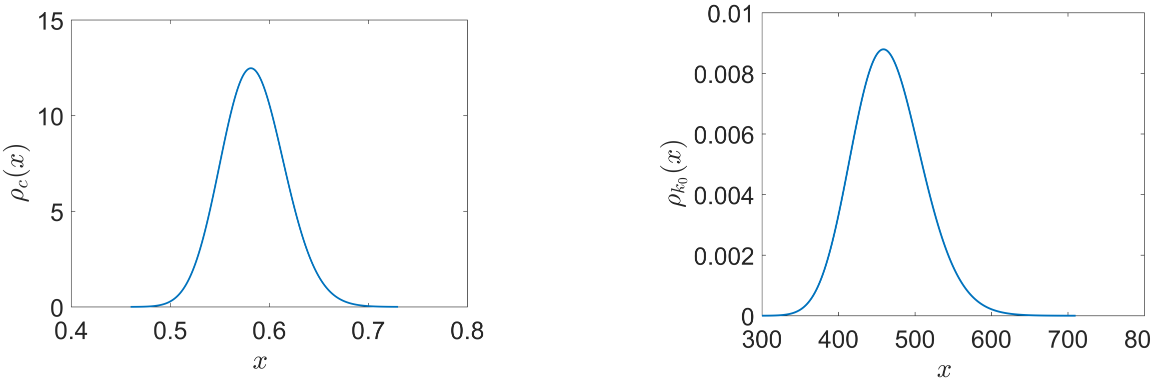

(c) $c = \mathrm{logN}(-0.5392, 0.0549)$ **(d)** $k_0 = \mathrm{logN}(6.1384, 0.0984)$

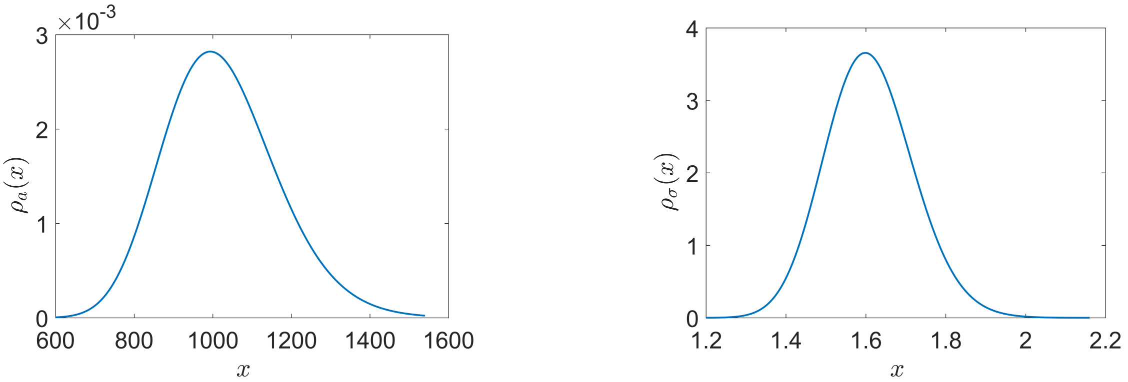

(e) $a = \mathrm{logN}(6.9214, 0.1409)$ **(f)** $\sigma = \mathrm{logN}(0.4738, 0.0681)$

Figure 47: Probability distribution functions of the Jiles-Athrton model parameters

B Truncated Karhunen-Loève theorem and physical properties

Lemma 1 *Let the random variables* $\{Y_i\}_{i=1}^M$ *are uniformly bounded with* $C_Y > 0$*. If the following inequality holds*

$$g(B,\cdot) - f'(B,\cdot) \geq C > 0, \quad \forall B > 0 \tag{249}$$

then the following inequality also holds

$$g_M(B,\cdot) - f'_M(B,\cdot) \geq \tilde{C} > 0, \quad \forall B > 0 \tag{250}$$

Proof 1 *For the case when the random variables are bounded it holds*

$$||g - g_M||_{L_\infty} = C_{g,M} < \infty, \tag{251}$$

For this proof $L_\infty := L_\infty(\Omega, P)$*. For the derivative of* $f(\cdot,\cdot)$ *we have*

$$f'(B,\theta) = e^{\upsilon(B,\theta)}, \tag{252}$$

$$f'_M(B,Y) = e^{\upsilon_M(B,Y)}, \tag{253}$$

Due to the Lipschitz continuity of the exponential function it holds

$$||f' - f'_M||_{L_\infty} = C_{f,M} < \infty. \tag{254}$$

By applying the triangular inequality we obtain

$$||\left(g - f'\right) - \left(g_M - f'_M\right)||_{L_\infty} \leq ||f' - f'_M||_{L_\infty} + ||g - g_M||_{L_\infty} = C_M, \tag{255}$$

where $C_M := C_{f,M} + C_{g,M}$ *The last inequality implies two inequalities*

$$\left(g - f'\right) - \left(g_M - f'_M\right) \leq C_M, \tag{256}$$

$$\left(g - f'\right) - \left(g_M - f'_M\right) \geq -C_M. \tag{257}$$

From the first inequality it follows that

$$g_M - f'_M \geq \tilde{C} > 0, \tag{258}$$

where $\tilde{C} := C - C_M > 0$ *for sufficiently large* M*.*

Lemma 2 *Let us assume that*

$$\alpha(B,\cdot) > 0, \quad \forall B \in \mathbb{R}, \tag{259}$$

then it holds

$$\alpha_M(B,\cdot) > 0, \quad \forall B \in \mathbb{R}. \tag{260}$$

Proof 2 *The bottom bound of* $\alpha(\cdot,\cdot)$ *are given as follows*

$$\overline{\alpha}(B) - \sum_{i=1}^{\infty} C_{Y_i} ||\lambda_i \phi_i^{\alpha}(B)||_{L^{\infty}(D)} < \alpha(B,\theta), \tag{261}$$

and for the truncated KLE $\alpha_M(\cdot,\cdot)$

$$\overline{\alpha}(B) - \sum_{i=1}^{M} C_{Y_i} ||\lambda_i \phi_i^{\alpha}(B)||_{L^{\infty}(D)} < \alpha_M(B,\theta). \tag{262}$$

In order to prove that the positivity of $\alpha_M(\cdot,\cdot)$ *one has to show that*

$$\overline{\alpha}(B) - \sum_{i=1}^{M} C_{Y_i} ||\lambda_i \phi_i^{\alpha}(B)||_{L^{\infty}(D)} > 0. \tag{263}$$

This is naturally expected to hold because if

$$\overline{\alpha}(B) - \sum_{i=1}^{\infty} C_{Y_i} ||\lambda_i \phi_i^{\alpha}(B)||_{L^{\infty}(D)} > 0, \tag{264}$$

the (263) *must hold since*

$$\sum_{i=1}^{\infty} C_{Y_i} ||\lambda_i \phi_i^{\alpha}(B)||_{L^{\infty}(D)} > \sum_{i=1}^{M} C_{Y_i} ||\lambda_i \phi_i^{\alpha}(B)||_{L^{\infty}(D)}. \tag{265}$$

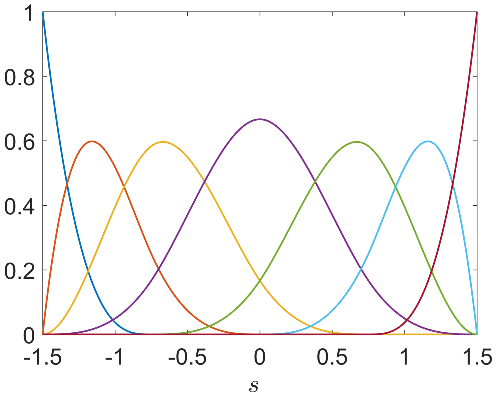

Figure 48: B-splines with $p = 3$ and $q = 0$

C B-spline basis functions

Let us introduce the sequence $\tau_N : s_1 \leq s_2, ..., \leq s_{N+p+1}$. The space of B-spline basis function is a linear span $\mathscr{L}_N^{p,q} = \text{span}\{N_k^{F,p}\}_{k=1}^N$ of degree p and minimal regularity of q. The k-th B-spline basis function is computed by using the Carl de Boor recursive relation

$$N_k^{F,p}(s) = \frac{s - s_k}{s_{k+p} - s_k} N_k^{p-1}(s) + \frac{s_{k+p+1} - s}{s_{k+p+1} - s_{k+1}} N_{k+1}^{p-1}(s), \tag{266}$$

where for $p = 0$

$$N_k^{F,0} = \begin{cases} 1 & s_k \leq s \leq s_{k+1}, \\ 0 & \text{otherwise,} \end{cases} \tag{267}$$

see [97, 98, 99]. The B-spline function has $q = p - r_k$ regularity if the knot s_k is duplicated r_k times. As an example of $N = 7$ third degree of splines, with the associated knot vector $(-1.5, -1.5, -1.5, -1, 5, -0.75, 0, 0.75, 1.5, 1.5, 1.5, 1.5)$, are shown in Fig. 48. The knots s_1 and s_{11} have been duplicated three times. Thus the regularity of N_1^F and N_7^F has dropped down to zero. The minimum regularity of this space of basis functions is $q = 0$ and it is denoted as $\mathscr{L}_N^{3,0}$.

List of Figures

List of Tables

References

[1] I. Babuška and J. Oden, “Verification and validation in computational engineering and science: Basic concepts,” *Computer Methods in Applied Mechanics and Engineering*, pp. 4057–4066, 09 2004.

[2] C. J. Roy and W. L. Oberkampf, “A comprehensive framework for verification, validation, and uncertainty quantification in scientific computing,” *Computer Methods in Applied Mechanics and Engineering*, vol. 200, no. 25, pp. 2131 – 2144, 2011.

[3] O. Maitre and O. Knio, *Spectral Methods for Uncertainty Quantification: With Applications to Computational Fluid Dynamics*. Scientific Computation, Springer Netherlands, 2010.

[4] D. Xiu, *Numerical Methods for Stochastic Computations: A Spectral Method Approach*. Princeton, NJ, USA: Princeton University Press, 2010.

[5] V. Barthelmann, E. Novak, and K. Ritter, “High dimensional polynomial interpolation on sparse grids,” *Advances in Computational Mathematics*, vol. 12, pp. 273–288, Mar 2000.

[6] H.-J. Bungartz and M. Griebel, “Sparse grids,” *Acta Numerica*, vol. 13, pp. 147–269, 2004.

[7] L. Grasedyck, D. Kressner, and C. Tobler, “A literature survey of low-rank tensor approximation techniques,” *GAMM-Mitteilungen*, pp. 53–78, 2013.

[8] W. Hackbusch, *Tensor Spaces and Numerical Tensor Calculus*, vol. 42. 01 2012.

[9] B. N. Khoromskij, “Tensors-structured numerical methods in scientific computing: Survey on recent advances,” *Chemometrics and Intelligent Laboratory Systems*, vol. 110, no. 1, pp. 1 – 19, 2012.

[10] D. Loukrezis, U. Römer, T. Casper, S. Schöps, and H. D. Gersem, “High dimensional uncertainty quantification for an electrothermal field problem using stochastic collocation on sparse grids and tensor train decomposition,” *International Journal of Numerical Modelling: Electronic Networks, Devices and Fields*, 10 2016.

[11] M. Loève, *Probability Theory I*. Comprehensive Manuals of Surgical Specialties, Springer, 1977.

[12] H. Hotelling, “Analysis of a complex of statistical variables into principal components,” *J. Educ. Psych.*, vol. 24, 1933.

[13] H. M. S. Harstick, M. Ritter, and W. Riehemann, “Influence of punching and tool wear on the magnetic properties of nonoriented electrical steel,” *IEEE Transactions on Magnetics*, vol. 50, pp. 1–4, April 2014.

[14] A. Saleem, N. Alatawneh, R. R. Chromik, and D. A. Lowther, “Effect of shear cutting on microstructure and magnetic properties of non-oriented electrical steel,” *IEEE Transactions on Magnetics*, vol. 52, pp. 1–4, May 2016.

[15] M. Bali and A. Muetze, “Influences of CO2 laser, FKL laser, and mechanical cutting on the magnetic properties of electrical steel sheets,” *IEEE Transactions on Industry Applications*, vol. 51, pp. 4446–4454, Nov 2015.

[16] S. K. Kuo, W. C. Lee, S. Y. Lin, and C. Y. Lu, “The influence of cutting edge deformations on magnetic performance degradation of electrical steel,” *IEEE Transactions on Industry Applications*, vol. 51, pp. 4357–4363, Nov 2015.

[17] N. Lewis, P. Anderson, J. Hall, and Y. Gao, “Power loss models in punched non-oriented electrical steel rings,” *IEEE Transactions on Magnetics*, vol. 52, pp. 1–4, May 2016.

[18] M. Bali, H. D. Gersem, and A. Muetze, “Epstein frame measurement based determination of original non-degraded and fully degraded magnetic properties of material submitted to mechanical cutting,” in *2015 IEEE International Electric Machines Drives Conference (IEMDC)*, pp. 1184–1189, May 2015.

[19] R. Ramarotafika, A. Benabou, and S. Clénet, “Stochastic modeling of soft magnetic properties of electrical steels: Application to stators of electrical machines,” *IEEE Transactions on Magnetics*, vol. 48, pp. 2573–2584, Oct 2012.

[20] R. Ramarotafika, A. Benabou, and S. Clénet, “Stochastic Jiles-Atherton model accounting for soft magnetic material variability,” *COMPEL - The international journal for computation and mathematics in electrical and electronic engineering*, vol. 32, no. 5, pp. 1679–1691, 2013.

[21] U. Römer, S. Schöps, and T. Weiland, “Stochastic modeling and regularity of the nonlinear elliptic curl–curl equation,” *SIAM/ASA Journal on Uncertainty Quantification*, vol. 4, no. 1, pp. 952–979, 2016.

[22] M. L. Hodgdon, “Applications of a theory of ferromagnetic hysteresis,” *IEEE Transactions on Magnetics*, vol. 24, pp. 218–221, Jan 1988.

[23] H. Cho, D. Venturi, and G. Karniadakis, “Karhunen-Loève expansion for multi-correlated stochastic processes,” *Probabilistic Engineering Mechanics*, vol. 34, no. Supplement C, pp. 157 – 167, 2013.

[24] R. Jankoski, U. Römer, and S. Schöps, “Modeling of spatial uncertainties in the magnetic reluctivity,” *COMPEL - The international journal for computation and mathematics in electrical and electronic engineering*, vol. 36, no. 4, pp. 1151–1167, 2017.

[25] J. D. Jackson, *Classical Electrodynamics*. 3rd ed. ed.

[26] B. Cornut, A. Kedous-Lebouc, and T. Waeckerlé, “From metallurgy to modelling of electrical steels: A multiple approach to their behaviour and use based on physics and experimental investigations,” *Journal of Magnetism and Magnetic Materials*, vol. 160, pp. 102 – 108, 1996. Proceedings of the twelfth International Conference on Soft Magnetic Materials.

[27] A. Buffa, H. Ammari, and J. Nédélec, “A justification of eddy currents model for the Maxwell equations,” *SIAM Journal on Applied Mathematics*, vol. 60, no. 5, pp. 1805–1823, 2000.

[28] K. Schmidt, O. Sterz, and R. Hiptmair, “Estimating the eddy-current modeling error,” *IEEE Transactions on Magnetics*, vol. 44, 2008.

[29] C. R. I. Emson and C. W. Trowbridge, “Transient 3D eddy currents using modified magnetic vector potentials and magnetic scalar potentials,” *IEEE Transactions on Magnetics*, vol. 24, pp. 86–89, Jan 1988.

[30] G. Bedrosian, “A new method for coupling finite element field solutions with external circuits and kinematics,” *IEEE Transactions on Magnetics*, vol. 29, pp. 1664–1668, Mar 1993.

[31] A. L. Chaillou and M. Suri, “Computable error estimators for the approximation of nonlinear problems by linearized models,” *Computer Methods in Applied Mechanics and Engineering*, vol. 196, no. 1, pp. 210 – 224, 2006.

[32] C. Pechstein and B. Jüttler, “Monotonicity-preserving interproximation of B-H-curves,” *J. Comput. Appl. Math.*, vol. 196, pp. 45–57, Nov. 2006.

[33] P. Grisvard, *Elliptic Problems in Nonsmooth Domains*. Society for Industrial and Applied Mathematics, 2011.

[34] W. Hackbusch, M. Schlick, R. Fadiman, and P. Ion, *Elliptic Differential Equations: Theory and Numerical Treatment*. Computational Mathematics Series, Springer, 1992.

[35] J. Lions and E. Magenes, *Non-homogeneous boundary value problems and applications*. No. v. 3 in Non-homogeneous Boundary Value Problems and Applications, Springer-Verlag, 1972.

[36] S. Mikhlin, *Variational methods in mathematical physics*. International series of monographs in pure and applied mathematics, Pergamon Press; [distributed by Macmillan, New York], 1964.

[37] S. Sobolev, *Some Applications of Functional Analysis in Mathematical Physics*. Translations of mathematical monographs, American Mathematical Society, 1991.

[38] L. C. K. John L. Volakis, Arindam Chatterjee, *Finite Element Method Electromagnetics: Antennas, Microwave Circuits, and Scattering Applications*. IEEE Press Series on Electromagnetic Wave Theory, Wiley, 1998.

[39] A. Nicolet and F. Delince, “Implicit Runge-Kutta methods for transient magnetic field computation,” *IEEE Transactions on Magnetics*, vol. 32, pp. 1405–1408, May 1996.

[40] C. Pechstein, *Multigrid-newton-methods for nonlinear magnetostatic problems, M.Sc. thesis*. Johannes Kepler Universität Linz, Austria.

[41] H. V. Sande, *Modeling and Finite Element Simulation of Non-linear Anisotropic Quasi-Static Electromagnetic Systems*. KU Leuven, 2003.

[42] J. Brauer, “Simple equations for the magnetization and reluctivity curves of steel,” *IEEE Transactions on Magnetics*, vol. 11, pp. 81–81, January 1975.

[43] D. Meeker, “FEM Magnetics.” `http://www.femm.info/wiki/Download`, 2016. (Online; accessed 15-May-2016).

[44] J. R. Shewchuk, “Triangle.” `https://www.cs.cmu.edu/%7equake/triangle.html`, 2005. (Online; accessed 15-May-2016).

[45] D. Meeker, “FEM Magnetics.” `http://www.femm.info/wiki/mytransformer`, 2006. (Online; accessed 15-May-2016).

[46] S. Schöps, D. Gersem, and T. Weiland, “Winding functions in transient magnetoquasistatic field-circuit coupled simulations,” *COMPEL - The international journal for computation and mathematics in electrical and electronic engineering*, vol. 32, no. 6, pp. 2063–2083, 2013.

[47] “Helmholtzzentrum für schwerionenforschung gsi.” `www.fair-center.de`, 2018.

[48] “Facility for antiproton and ion research in europe gmbh.” `www.gsi.de`, 2018.

[49] S. Russenschuck, *Field Computation for Accelerator Magnets: Analytical and Numerical Methods for Electromagnetic Design and Optimization*. Wiley, 2011.

[50] H. D. Gersem, V. Srinivasan, and C. Muehle, “Nonlinear three-port magnetic-circuit elements for simulating bending magnets,” *COMPEL - The international journal for computation and mathematics in electrical and electronic engineering*, vol. 37, no. 1, pp. 266–279, 2018.

[51] S. Koch, H. D. Gersem, and T. Weiland, “Transient 3D finite element simulations of the field quality in the aperture of the SIS-100 dipole magnet,” *IEEE Transactions on Applied Superconductivity*, vol. 19, pp. 1162–1166, June 2009.

[52] D. Xiu and J. S. Hesthaven, “High-order collocation methods for differential equations with random inputs,” *SIAM Journal on Scientific Computing*, vol. 27, no. 3, pp. 1118–1139, 2005.

[53] D. W. Scott, *Multivariate density estimation*. Wiley Series in Probability and Mathematical Statistics: Applied Probability and Statistics, John Wiley & Sons, Inc., New York, 1992. Theory, practice, and visualization, A Wiley-Interscience Publication.

[54] S. J. Sheather and M. C. Jones, “A reliable data-based bandwidth selection method for kernel density estimation,” *J. Roy. Statist. Soc. Ser. B*, vol. 53, no. 3, pp. 683–690, 1991.

[55] B. W. Silverman, *Density estimation for statistics and data analysis*. Monographs on Statistics and Applied Probability, Chapman & Hall, London, 1986.

[56] J. S. Simonoff, *Smoothing methods in statistics*. Springer Series in Statistics, Springer-Verlag, New York, 1996.

[57] M. C. Jones, J. S. Marron, and S. J. Sheather, “Progress in data-based bandwidth selection for kernel density estimation,” *Comput. Statist.*, vol. 11, no. 3, pp. 337–381, 1996.

[58] M. C. Jones, I. J. McKay, and T.-C. Hu, “Variable location and scale kernel density estimation,” *Ann. Inst. Statist. Math.*, vol. 46, no. 3, pp. 521–535, 1994.

[59] Z. I. Botev, J. F. Grotowski, and D. P. Kroese, “Kernel density estimation via diffusion,” *Ann. Statist.*, vol. 38, pp. 2916–2957, 10 2010.

[60] I. Babuška, F. Nobile, and R. Tempone, “A stochastic collocation method for elliptic partial differential equations with random input data,” *SIAM Journal on Numerical Analysis*, vol. 45, no. 3, pp. 1005–1034, 2007.

[61] M. Motamed, F. Nobile, and R. Tempone, "A stochastic collocation method for the second order wave equation with a discontinuous random speed," *Numerische Mathematik*, vol. 123, pp. 493–536, Mar 2013.

[62] F. Nobile, R. Tempone, and C. G. Webster, "A sparse grid stochastic collocation method for partial differential equations with random input data," *SIAM Journal on Numerical Analysis*, vol. 46, no. 5, pp. 2309–2345, 2008.

[63] F. Nobile, R. Tempone, and C. G. Webster, "An anisotropic sparse grid stochastic collocation method for partial differential equations with random input data," *SIAM Journal on Numerical Analysis*, vol. 46, no. 5, pp. 2411–2442, 2008.

[64] A. Iványi, *Hysteresis Models in Electromagnetic Computation*. Scientific review, International Specialized Book Service Incorporated, 1997.

[65] P. Weiss, "L' hypothèse du champ moléculaire et la propriété ferromagnétique," *J. Phys. Theor. Appl.*, vol. 6, no. 1, pp. 661–690, 1907.

[66] R. Bozorth, *Ferromagnetism*. Wiley, 1993.

[67] D. Jiles and D. Atherton, "Theory of ferromagnetic hysteresis," *Journal of Magnetism and Magnetic Materials*, vol. 61, no. 1, pp. 48 – 60, 1986.

[68] J. W. Macki, P. Nistri, and P. Zecca, "Mathematical models for hysteresis," *SIAM Review*, vol. 35, no. 1, pp. 94–123, 1993.

[69] P. Duhem., "Die dauernden Änderungen und die thermodynamik, I," *Zeitschrift für Physikalische Chemie*, vol. 22, no. 1, pp. 543–589, 1897.

[70] B. D. Coleman and M. L. Hodgdon, "On a class of constitutive relations for ferromagnetic hysteresis," *Archive for Rational Mechanics and Analysis*, vol. 99, pp. 375–396, Dec. 1987.

[71] M. L. Hodgdon, "Mathematical theory and calculations of magnetic hysteresis curves," *IEEE Transactions on Magnetics*, vol. 24, no. 6, pp. 3120–3122, 1988.

[72] F. E. Curtis and M. L. Overton, "A sequential quadratic programming algorithm for nonconvex, nonsmooth constrained optimization," *SIAM Journal on Optimization*, vol. 22, no. 2, pp. 474–500, 2012.

[73] J. O. Ramsay, "Estimating smooth monotone functions," *Journal of the Royal Statistical Society: Series B (Statistical Methodology)*, vol. 60, no. 2.

[74] C. Lanczos, "An iteration method for the solution of the eigenvalue problem of linear differential and integral operators," *J. Res. Natl. Bur. Stand. B*, vol. 45, pp. 255–282, 1950.

[75] B. N. Parlett and D. S. Scott, "The Lanczos algorithm with selective orthogonalization," *Mathematics of Computation*, vol. 33, pp. 217–238, 11 1978.

[76] B. Parlett, *The Symmetric Eigenvalue Problem*. Society for Industrial and Applied Mathematics, 1998.

[77] J. Cullum, W. Kerner, and R. Willoughby, "A generalized nonsymmetric Lanczos procedure," *Computer Physics Communications*, vol. 53, no. 1, pp. 19 – 48, 1989.

[78] C. Schwab and R. A. Todor, "Karhunen-Loève approximation of random fields by generalized fast multipole methods," *J. Comput. Phys.*, vol. 217, pp. 100–122, Sept. 2006.

[79] B. N. Khoromskij, A. Litvinenko, and H. G. Matthies, "Application of hierarchical matrices for computing the Karhunen–Loève expansion," *Computing*, vol. 84, pp. 49–67, Apr 2009.

[80] D. Brunner, M. Junge, P. Rapp, M. Bebendorf, and L. Gaul, "Comparison of the fast multipole method with hierarchical matrices for the helmholtz-BEM," *Computer Modeling in Engineering and Sciences*, vol. 58, no. 2, pp. 131–160, 2010.

[81] C. C. PAIGE, "Error analysis of the Lanczos algorithm for tridiagonalizing a symmetric matrix," *IMA Journal of Applied Mathematics*, vol. 18, no. 3, pp. 341–349, 1976.

[82] W. Hackbusch, "A sparse matrix arithmetic based on $\mathcal{H}$-matrices. Part I: Introduction to $\mathcal{H}$-matrices," *Computing*, vol. 62, pp. 89–108, 1999.

[83] W. Hackbusch, B. N. Khoromskij, and S. A. Sauter, "On $\mathcal{H}^2$-matrices," in *Lectures on Applied Mathematics* (H. Bungartz, R. Hoppe, and C. Zenger, eds.), pp. 9–29, Springer-Verlag, Berlin, 2000.

[84] S. Börm and W. Hackbusch, "Data-sparse approximation by adaptive $\mathcal{H}^2$-matrices," *Computing*, vol. 69, pp. 1–35, 2002.

[85] L. Grasedyck and W. Hackbusch, "Construction and arithmetics of $\mathcal{H}$-matrices," *Computing*, vol. 70, pp. 295–334, 2003.

[86] W. Hackbusch, *Hierarchische Matrizen — Algorithmen und Analysis*. Springer, 2009.

[87] S. Börm, *Efficient Numerical Methods for Non-local Operators: H2-matrix Compression, Algorithms and Analysis*. EMS tracts in mathematics, European Mathematical Society, 2010.

[88] J. Djokic, *Efficient Update of Hierarchical Matrices in the case of Adaptive Discretization Scheme*. PhD thesis, Universität Zürich, 2006.

[89] M. Bebendorf, "Approximation of boundary element matrices," *Numerische Mathematik*, vol. 86, no. 4, pp. 565–589, 2000.

[90] S. Börm and S. Christophersen, "H2Lib repository." `https://github.com/H2Lib/H2Lib/tree/community`, 2016. (Online; accessed 20-May-2016).

[91] E. G. Araujo, J. Schneider, K. Verbeken, G. Pasquarella, and Y. Houbaert, "Dimensional effects on magnetic properties of Fe 2013;Si steels due to laser and mechanical cutting," *IEEE Transactions on Magnetics*, vol. 46, pp. 213–216, Feb 2010.

[92] Y. Kurosaki, H. Mogi, H. Fujii, T. Kubota, and M. Shiozaki, "Importance of punching and workability in non-oriented electrical steel sheets," *Journal of Magnetism and Magnetic Materials*, vol. 320, no. 20, pp. 2474 – 2480, 2008. Proceedings of the 18th International Symposium on Soft Magnetic Materials.

[93] C. A. Baguley, U. K. Madawala, and B. Carsten, "The influence of remanence on magnetostrictive vibration and hysteresis in Mn-Zn Ferrite cores," *IEEE Transactions on Magnetics*, vol. 48, pp. 1844–1850, May 2012.

[94] K. C. Kim, K. S. Yoon, C. S. Yang, K. H. Shin, H. Y. Jeong, and Y. H. Kim, "Remnant magnetization prediction in the demagnetization process by orthogonal magnetic field," *IEEE Transactions on Magnetics*, vol. 47, pp. 4360–4363, Oct 2011.

[95] K. Seo, J. M. Han, and G. S. Park, "Effects of a remanent magnetization on the sensing signals in magnetic flux leakage type ndt," in *2007 International Conference on Electrical Machines and Systems (ICEMS)*, pp. 1932–1935, Oct 2007.

[96] F. Nobile, R. Tempone, and C. Webster, "An anisotropic sparse grid stochastic collocation method for partial differential equations with random input data," *SIAM Journal on Numerical Analysis*, vol. 46, no. 5, pp. 2411–2442, 2008.

[97] T. Hughes, J. Cottrell, and Y. Bazilevs, "Isogeometric analysis: CAD, finite elements, NURBS, exact geometry and mesh refinement," *Computer Methods in Applied Mechanics and Engineering*, vol. 194, no. 39, pp. 4135 – 4195, 2005.

[98] A. Buffa, G. Sangalli, and R. Vázquez, "Isogeometric analysis in electromagnetics: B-splines approximation," *Computer Methods in Applied Mechanics and Engineering*, vol. 199, no. 17, pp. 1143 – 1152, 2010.

[99] C. De Boor, *A practical guide to splines; rev. ed.* Applied mathematical sciences, Berlin: Springer, 2001.

Acknowledgment

The work of this thesis was financially supported by the Excellence Initiative of the German federal and state governments and the Graduate School of Computational Engineering at the Technical University Darmstadt.

There are several people that I would like to thank. First of all, I am thankful to professor Sebastian Schöps for giving me the opportunity to be a PhD student at the graduate school of computational engineering in Darmstadt and for his supervision. I owe my gratitude to Professor Ulrich Römer for his direct supervision, constant reading and correcting this thesis. Without his criticism and valuable advices the work in this thesis would not have been possible. Professor Ulrich Römer guided me in the early beginning when the UQ topic was new to me.

Also I would like to thank professor Herbert De Gersem for sharing his experience on magnetic hysteresis and design of accelerator magnets. Some of the fruitful discussions I had with him greatly inspired me to tackle certain problems in this thesis. I am thankful also to my colleague and friend Dimitrios Loukrezis for proof reading some parts of the thesis and of course for the great working atmosphere in the office we shared.

I would like to thank all of the TEMF colleagues for the great time during the past three years.

I will be forever indebted to my mother Vesna, father Slavko and my sister Verica for their dedication and encouragement during all my studies.

Curriculum Vitae

Personal data

- Name and surname : Radoslav Jankoski
- Birth place : Gostivar, R. Macedonia
- Date of birth : 30.08.1990
- Nationality : Macedonian

Education

[2015-2018] - PhD studies at the Technical university of Darmstadt, faculty for electrical engineering and information technology, Darmstadt, Germany

[2013-2014] - M.Sc at Ss. Cyril and Methodius university, the faculty for electrical engineering and information technology FEIT, Skopje, R. Macedonia

[01.09.2013 25.12.2013] - Guest scientist at the technical university of Ilmenau, Germany

[2009-2013] - B.Sc at Ss. Cyril and Methodius university, faculty for electrical engineering FEIT and information technology, Skopje, R. Macedonia

Awards

- Best poster paper award at COMPUMAG 2017, Daejon, South Korea for the paper entitled *The impact of spatial uncertainties of the magnetic reluctivity in the field quality of a combined function magnet: Radoslav Jankoski, Ulrich Römer, Sebastian Schöps*

Key publication

- Radoslav Jankoski, Ulrich Römer, Sebastian Schöps, (2017) "Modeling of spatial uncertainties in the magnetic reluctivity", COMPEL - The international journal for computation and mathematics in electrical and electronic engineering, Vol. 36 Issue: 4, pp.1151-1167, https://doi.org/10.1108/COMPEL-10-2016-0438